2023-12-19

Finite Element-based Methods for Dent Assessment on Pipelines

zhao, jian

UNIVERSITY OF CALGARY

Finite Element-based Methods for Dent Assessment on Pipelines

by

Jian Zhao

A THESIS

SUBMITTD TO THE FACULTY OF GRADUATE STUDIES

IN PARTIAL FULFILMENT OF THE REQUIREMENTS FOR THE

DEGREE OF DOCTOR OF PHILOSOPHY

GRADUATE PROGRAM IN MECHANICAL AND MANUFACTURING ENGINEERING

CALGARY, ALBERTA

DECEMBER, 2023

Abstract

As a well-developed form for energy transportation over wide ranges and long distances, pipelines always encounter various threats in service. In recent years, with the strong demand of clean energy, hydrogen transport in existing pipelines induces new challenges to the pipelines. Dent is a common mechanical defect present on pipelines, compromising structural integrity and causing pipeline failures. To date, there have been limited methods available to assess dent, and a dent combined with other types of defects such as corrosion.

In this work, novel methods and criteria were developed for assessment of pipeline dent, corrosion in dent and hydrogen distribution at the dent using finite element (FE) modeling. Denting and spring-back processes were modeled and plain dents were created on the pipeline. A new criterion based on ductile damage failure indicator analysis was proposed. Pressure-bearing capacity was assessed on corroded pipelines containing a dent, where the mutual interaction between corrosion and the dent were determined. In addition, a method was developed to assess the corrosion in dent by considering both mechanical and electrochemical forces. For dented pipelines repurposed for transporting hydrogen gas, a FE-based model was developed to determine the stress/strain and H atom concentrations at the dent, where denting, spring-back and cyclic loading processes were modeled. Furthermore, the hydrogen-induced crack initiation on the pipeline subject to denting process was investigated using the phase field method.

Research accomplishments made to date

1. Jian Zhao, Y. Frank Cheng, A new criterion based on strain determination for dent assessment of pipelines, Journal of Pipeline Science and Engineering, 2 (2022) 18-28, https://doi.org/10.1016/j.jpse.2021.11.004

2. Jian Zhao, Yun-Rong Lv, Y. Frank Cheng, Standards and methods for dent assessment and failure prediction of pipelines: A critical review, Petroleum Science, 19 (2022) 3029-3045, https://doi.org/10.1016/j.petsci.2022.10.003

3. Jian Zhao, Yun-Rong Lv, Y. Frank Cheng, A new method for assessment of burst pressure capacity of corroded X80 steel pipelines containing a dent, International Journal of Pressure Vessels and Piping, 199 (2022) 104742, https://doi.org/10.1016/j.ijpvp.2022.104742

4. Jian Zhao, Y. Frank Cheng, Assessment by finite element modeling of corrosion in dent on X52 steel pipelines, International Journal of Pressure Vessels and Piping, 200 (2022) 104835, https://doi.org/10.1016/j.ijpvp.2022.104835

5. Jian Zhao, Y. Frank Cheng, Finite element modeling of the distribution of hydrogen atoms at a dent on pipelines for hydrogen transport under cyclic loading, International Journal of Fracture, (2023), https://doi.org/10.1007/s10704-023-00741-8

6. Jian Zhao, Y. Frank Cheng, Investigation of hydrogen induced cracking on dented pipelines using phase field method, International Journal of Mechanical Science, in submission.

Acknowledgement

My sincere and grateful thanks go firstly to my supervisor, Professor Frank Cheng, whose high-level guidance, expertise, and unwavering support have been instrumental throughout my research journey. His noble ethics and rigorous research style keep shaping my academic foundation and have also been a source of inspiration for my personal and professional growth.

I extend my appreciation to the members in our research group, Yinghao Sun, Qing Hu, Jin Zhang, Xin Fan, Qin Min, Guojin Qin, Yi Shuai, Shiwen Guo and Boxin Wei, who provide essential helps and supports both in research and my life. Thanks also to my friends I met in Calgary, Haobin Chen (Peter), Zhuoran Dang, Yaser, Luma, Miriam, Navroop and those whose name cannot all be listed here, for the constant source of encouragement and friendship.

Deep gratitude to my family for their firm support and great love over my long journey pursuing knowledge and academic achievement. Covid pandemic and distance cannot stop me from going home. Special thanks to my girl friend Pengli Jin, who gives unwavering understand, patience and attention to me.

Lastly, I would like to express my gratitude to the members of my thesis committee, for their valuable insights, constructive feedback, and the time invested in reviewing and refining this work.

Dedication

To my beloved parents and family,

who try their best to raise me and shape my life.

Table of Contents

List of Tables

List of Figures and Illustrations

List of Symbols, Abbreviations and Nomenclature

Symbol	Definition
API	American Petroleum Institute
ASME	American Society of Mechanical Engineers
ASTM	American Society for Testing and Materials
BS	British Standard
CSA	Canadian Standards Association
CFR	Code of Federal Regulations
DFDI	Ductile failure damage indicator
DNV	Det Norske Veritas
FE	Finite element
FAD	Failure assessment diagram
H	Hydrogen
HE	Hydrogen embrittlement
HIC	Hydrogen induced cracking
HEDE	Hydrogen enhanced decohesion
HELP	Hydrogen enhanced localized plasticity
ILI	In-Line-Inspection
OD	Outer diameter
M-E	Mechano-electrochemical
PF	Phase field
R-O	Ramberg-Osgood relationship
SCC	Stress corrosion cracking
SLD	Strain limit damage
SMYS	Specific minimum yield strength
UKOPA	The United Kingdom Onshore Pipeline Operators' Association
a_0	Corrosion rate
C	Total H concentration
C_1	Constant
C_2	Elongation rate for the material
C_L	Lattice H atom concentration
C_T	H atom concentration in the traps
d_D	Dent depth
d_c	Corrosion depth
D_e	*DFDI* value under the simplified condition
D_{e0}	*DFDI* value under the simplified condition before spring-back
D_{em}	Maximum ductile damage factor at dent
D_i	Internal diameter of the pipeline
D_o	Outer diameter of the pipeline
D_{in}	Diameter of the indenter
D_L	Lattice H diffusion coefficient
E	Elastic modulus
f_1	Constant
f_2	Constant

F	Faraday's constant
h	Permanent dent depth
h_o	The initial dent depth
H	History variable
i_a	Anodic current density
i_c	Cathodic current density
I	Integral value
J	Hydrogen flux
K_r	Toughness ratio
l_0	Characteristic length scale l_0
l_c	Longitudinal length of the corroded area
L	Length of the dent in axial direction
L_1	Length of the pipeline
L_r^p	Load ratio
m	Membrane strain
M	Folias factor
M_m	Atomic weight of iron
N_A	Avogadro's number
N_L	Density of lattice sites to host H atoms
N_T	Number of trapping sites per unit volume
p	Internal pressure
R	Ideal gas constant
R_s	Surface radius of curvature
R_0	Initial pipe surface radius
R_1	External surface radius of curvature in the transverse plane
R_2	External surface radius of curvature in longitudinal plane
S_{flow}	Flow stress
S_F	Burst pressure of the corroded pipeline
t	Wall thickness of the pipeline
T_c	Time for corrosion growth
T	Absolute temperature
u	Dent profile function in longitudinal direction
v	Dent profile function in circumferential direction
w	Pipe wall deflection in the radial direction
W_B^d	Binding energy of dislocations
x	Axial distance of the pipeline
X	Circumferential direction
y	Function of the contour of the dented area with the variable x
Y	Radial direction
z	Calculation constant
Z	Axial direction
α	Constant that used in the R-O relationship
β	Constant that used in the R-O relationship
β_L	Capacity number of lattice sites hosting H atoms
ε	Strain

ε_1	Circumferential bending strain
ε_1	Circumferential bending strain
ε_2	Longitudinal bending strain
ε_3	Longitudinal extensional strain
ε_{as}	Strain at dent apex after spring-back
ε_{apex}	Equivalent strain at the dent apex
ε_{iA}	Equivalent strains of the inner surface at the dent apex
ε_{ini}	Strain at dent apex before spring-back
ε_{oA}	Equivalent strains of the outer surface at the dent apex
ε_{eq}	Equivalent strain
ε_d	Constant
ε_i	Equivalent strain on the inside pipe surface
ε_{max}	Maximum equivalent strain of inner and outer surfaces
ε_o	Equivalent strain on the outside pipe surface
ε_x	Strain in axial direction
ε_x^b	Bending strain in axial direction
ε_y^b	Bending strain in circumferential direction
ε_x^m	Membrane strain in axial direction
ε_y^m	Membrane strain in circumferential direction
ε_x^o	Initial strain due to the pressure in the pipe in axial direction
ε_y^o	Initial strain due to the pressure in the pipe in hoop direction
ε_y	Strain in circumferential direction
ε_z	Strain in radial direction
ϕ	Phase field parameter
φ^0	Standard equilibrium potential
ψ	Strain energy density
$\varphi_{a,eq}$	Anodic reaction equilibrium potential
$\varphi_{c,eq}$	Cathodic reaction equilibrium potential
γ_{xy}	Shear strain
θ_L	Lattice sites occupancy
θ_T	Trap occupancy
ρ_M	Density of iron
σ	Stress
σ_{eq}	Equivalent stress
σ_f	Flow stress
σ_H	Hydrostatic stress
σ_m	Average stress
σ_y	Yield strength
σ_u	Ultimate tensile strength
υ	Poisson's ratio

Chapter One: Introduction

1.1 Research background

Pipelines provide an efficient and effective means for transportation of natural gas and crude oil over a long distance around the world [1-5]. Large transportation capacity, low cost, long service life and high stability drive a large-scale construction of the pipelines. Pipelines are thin-walled structures that are made of various grades of steels such as X46, X52 and X80 steels. During service, the pipelines encounter multiple threats, e.g., dent, gouge, corrosion and cracks, to integrity of the system [1, 6-10]. In recent years, hydrogen transport by existing pipelines has attracted wide attention, while new challenges are associated with the pipelines in high-pressure hydrogen gas environments [6, 7].

Mechanical defects caused by rock impact, resting on rock or third-machinery strike are constantly detected on pipelines [8]. Dent is a common form of mechanical defect where there is no metal loss [9, 10]. Failure of dented pipelines can result in a decreased pressure-bearing capacity and the leakage of carried fluids. Stress and strain concentrations, micro cracks and corrosion can be caused at the dents, significantly degrading the performance of the pipelines. Thus, development of accurate methods for failure assessment of dented pipelines has always been a top priority to pipeline operators. Many types of dents can be found on the pipelines, such as constrained and unconstrained dents, and plain and kinked dent. Unconstrained plain dents have been wildly investigated and many assessment methods have been developed. However, the failure mechanism of dented pipelines is still unclear. It is validated in experiments and finite element (FE) simulations [11, 12] that the pressure capacity of the pipelines is not affected by plain dents. Instead, a ductile fracture is found in dent area [13, 14], however, relative investigations do not provide information on threshold conditions for the fracture occurrence. Moreover, methods for

strain estimation and failure assessment in existing standards usually give inaccurate failure criteria. Improvement on failure criterion for dented pipelines is an urgent demand for pipeline engineering development.

Buried pipelines can experience corrosion due to degradation of external coatings and cathodic protection, adversely affecting the pipeline performance safety [15, 16]. To date, investigations have been conducted to assess the burst failure capacity of dented pipelines and corroded pipelines independently. Whereas multiple defects such as dents and corrosion are usually present on pipelines, resulting in an accelerating structural degradation and failure of the pipelines [17, 18]. Corrosion is considered as a metal-loss defect due to the electrochemical reaction, where the anodic reaction is normally iron oxidation, and the cathodic reaction depends on the environmental conditions. For example, buried pipelines can suffer from corrosion in a so-called near-neutral pH electrolyte under disbonded coatings, where the cathodic reaction is mainly the hydrogen evolution [19-22]. Different from dent, corrosion can continuously grow to cause increased metal loss with time and this process is affected by mechanical loads. A mechano-electrochemical (M-E) interaction concept is developed to define the effect of mechanical and electrochemical forces on pipeline corrosion growth [23]. Cheng group initiated the M-E concept in pipeline corrosion study and contributes to a wide application of the concept for pipeline corrosion defect assessment [1, 22, 24, 25]. To date, there has been rare work investigating corrosion in dent and assessing the impact on pipeline integrity. This is a major gap to be filled in terms of an accurate and reliable assessment method applied for pipelines containing both a dent and corrosion defect.

Furthermore, it has been accepted that hydrogen will play a central role in energy transition. Pipelines provides an economical and effective mechanism to transport hydrogen over long

distances. However, pipeline steels are prone to hydrogen embrittlement (HE), a problem potentially causing pipeline fracture [26-28]. Hydrogen (H) atoms, once generating in the service environment and entering the steels, can degrade the mechanical properties of the steels, such as reduced fracture toughness [29, 30], and cause crack initiation and propagation through various mechanisms [31-35]. Therefore, determination of H atom distribution in the steels and estimation of the critical H atom concentration to initiate cracks are critical to safety of the pipelines, especially those containing dent defects. To date, there has been no method or model available to assess the HE risk of dented pipelines.

1.2 Research objectives

The main objectives of this research are to develop new models and methods for accurate assessment of dented pipeline, including corrosion in dent, H atom distribution in steels, and the hydrogen-induced crack initiation under pressure fluctuations. Specific progresses will be made in the following aspects.

1) Establish an FE based model to simulate the denting process on a steel pipe, with the modeling results validated with existing experimental measurements and relevant data in literature.

2) Determine the stress and strain distributions at the dent area, and develop a new, strain-based assessment method for failure of dented pipelines.

3) Model the denting process on a corroded pipeline and develop a new burst failure assessment criterion considering the mutual interaction of the dent and the corrosion defect.

4) Develop an FE model assessing X52 steel pipe containing corrosion in dent in a deoxygenated, near-neutral pH electrolyte while considering the M-E interaction.

5) Investigate the H atom diffusion and distribution at an unconstrained dent on an X52 steel pipe under cyclic loading of various magnitudes.

6) Develop an assessment method for determination of hydrogen-induced crack initiation and the critical dent depth to initiate cracks.

1.3 Content of thesis

The thesis is composed of eight chapters and the contents are listed as follows.

Chapter One is an introduction of the research background, objectives and outlines of the thesis.

Chapter Two presents the literature review over the fundamental basis for dented pipeline, corrosion, fracture analysis, H diffusion theory and HIC of pipeline steels. Research progress in literature and remarks on assessment methods are also summarised.

Chapter Three proposes a new criterion for the dent assessment of pipelines based on the ductile damage failure indictor (DFDI) criterion combined with improved strain determination by a finite element (FE) model. Parameters such as dent depth, indenter size and spring-back upon removal of indenter are considered into the assessment of dented pipeline. The limitations of ASME B31.8 in dent assessment are explained and a more accurate criterion is established.

Chapter Four develops a novel method to determine the pressure-bearing capacity of corroded pipelines containing a dent. An FE model is developed to simulate the mutual interaction between the dent and corrosion, and the stress/strain concentrations are analyzed. A burst pressure analysis method for the pipeline containing corrosion and dent is proposed, considering the corrosion growth affected by the dent.

Chapter Five simulates the growth of corrosion in the dent on a pipeline by coupling the mechanical and electrochemical forces. A deoxygenated, near-neutral pH electrolyte is present in the dent area and the anodic current density is calculated as the indicator of corrosion rate.

Chapter Six investigates the H atoms diffusion in the dented pipeline under cyclic internal pressure. Effects of stress-strain concentrations at the dent on H atom diffusion are studied. Implications on occurrence of hydrogen embrittlement are analyzed.

Chapter Seven develops a phase field model for assessment of hydrogen-induced crack initiation on dented pipelines. A 3-D FE model is proposed and the hydrogen induced degradation of fracture toughness of the steel is investigated.

Chapter Eight includes main conclusions and limitations of the research work in this thesis. Remarks for assessments of dented pipelines in a variety of complex environmental conditions are provided.

Chapter Two: Literature review*

2.1 Overview of dent on pipelines and the interaction with other defects

Multiple threats exist to adversely affect the integrity and safety of pipelines in the field. These include corrosion, cracks, mechanical damage, material and manufacturing anomalies, geohazards and external interference [36]. Dent, a common type of mechanical damage introduced during pipeline construction and excavation activities, is defined as a permanent inward plastic deformation on pipe wall. Dents have caused frequent pipeline failures [37-39]. It was reported that 50% of pipelines in service contained over 10 dents after excavation and inspection [40]. Moreover, 60% of pipeline failure cases were related to dents or dents combined with other types of defects [41]. Development of accurate and reliable techniques for dent assessment has been paid extensive attention to pipeline industry.

Decades of investigations into failure assessment of dented pipelines have developed a system of standards to provide guidance in practice. Commonly used standard provisions for dented pipelines include [13, 42-44] ASME B31.8, ASME B31.4, ASME B31G, API 579, API 1160, CSA Z662, etc. Depth-based criterion and strain-based criterion are typical methods to assess the damage of a dent to pipelines [45, 46]. The critical depth and the maximum strain at the center of the dent are respectively specified as indicators to determine the resulting damage of the dent. Many researchers [12, 47, 48] investigated the critical dent depth criterion and proposed improved critical values. The strain-based criterion uses the profile data from In-Line-Inspection (ILI) tools and formulas in the standard to calculate the critical strain at the dent center. It was noted [13, 49]

* This chapter has been published as:

Jian Zhao, Yunrong Lv, Y. Frank Cheng, Standards and methods for dent assessment and failure prediction of pipelines: A critical review, *Petroleum Science*, 19 (2022) 3029-3045. https://doi.org/10.1016/j.petsci.2022.10.003

that the strain-determination formulas are deficient, and many modified methods were thus proposed.

Methods available in standards are easy to operate and estimate the severity of the dent combined with other defects. However, the inaccuracy and conservatism of estimation results limit application of the standards. It is widely accepted [50-52] that experimental testing is the most reliable method to provide true results. However, as compared with the complexity and facility requirement of the experimental tests, the FE method provides an accurate assessment tool that can significantly decrease the financial and time consuming.

Dents interacting with corrosion is common in engineering. After a long time of service in the field, pipelines usually contain both corrosion and dent defects. Corrosion defects such as pits and general corrosion are metal-loss damages, causing thinning of pipe wall [53, 54]. The primary consequence of corrosion damage is to decrease pressure capacity of the pipelines [55, 56] and thus, the criteria provided in standards are based on the burst pressure prediction [1]. Dents are usually adjacent to or overlapped with corrosion defects, and the synergistic effect of dent and corrosion cannot be simply assessed by existing standards. The corrosion is unique in terms of its continuous growth with time and a mutual interaction exists between the dent and corrosion, while the problem is barely considered in the previous assessments. According to the M-E interaction theory [22, 24, 25], a plastic strain can remarkably enhance the anodic current density, i.e., corrosion rate, of pipe steels in a local area such as a dent. In addition to the hoop stress resulting from the internal pressure and potential soil stress due to ground movement, a significant deformation occurs at the dent to generate a large residue stress. When the external coating is disbonded and a corrosive environment is generated, the electrochemical condition is usually associated with CO_2 dissolved in ground water, which permeates into the dent area. If the coating,

such as a polyethylene-based coating, shields the cathodic protection current from reaching the trapped water, a near-neutral pH, diluted bicarbonate solution is generated to cause corrosion of the steel at the dent. In literature, various defect assessment methods available today usually consider the dent and the corrosion separately [13]. Although some failure forms such as fatigue and inner pressure-induced burst were investigated in a dented pipeline [57, 58], the denting process was applied on the pipeline where a corrosion defect was already present.

For pipelines carrying high-pressure hydrogen gas in either pure or blended form, hydrogen embrittlement is a potential threat to integrity of the pipelines [31, 35, 59]. In recent years, substantial attention has been paid to pipeline HE problem. Compared with newly constructed pipelines, the existing natural gas pipelines are associated with additional challenges when they are converted for hydrogen service [60-62]. The diffusion of H atoms in the steels can be influenced by stress condition, especially under plastic deformation [63]. In addition, gas pipelines usually experience frequent pressure fluctuations [64, 65]. A combined effect of the stress and strain concentration at the dent and the cyclic loading resulting from pressure fluctuations is expected to remarkably affect the HE susceptibility of the pipelines.

The HE of pipeline is caused by diffusion and local concentration of H atoms in lattice sites and traps in the steels [66, 67]. Various HE mechanisms have been proposed to illustrate crack initiation and propagation under service conditions [68-70], including pipeline HE or hydrogen-induced cracking behavior [30, 71]. However, the presence of dent on existing pipelines makes it difficult to predict and assess the HE occurrence. Relevant methods do not exist to assess pipeline HE in the presence of dent on pipe body.

2.2 Assessment standards of the dented pipelines

Plain dent is a smooth dent without metal loss or other forms of damage [10, 72]. By applying the failure criteria in standards, the failure assessment of dented pipelines can be conducted. To date, failure criteria for plain dent in existing standards can be mainly classified as the depth-based criteria, such as ASME B31.4, CSA Z662 and API 1160, and the strain-based criteria, such as ASME B31.8. For most depth-based criteria, the critical depth of the plain dent is set as 6% of the outer diameter of the pipeline. Although the depth-based criteria are considered inaccurate, it is easy to obtain the depth parameter for pipeline failure evaluation [73]. For the strain-based criterion like ASME B31.8, the algorithm of the maximum equivalent strain is presented in Table 2.1. Parameters like dent depth, and the external surface radii of curvature in the transverse and longitudinal planes through the dent are required.

Compared with plain dent, a dent combined with other defects like gouges, corrosion and cracks is much more complicated and dangerous to pipeline safety. It is confirmed that the presence of other defects on a dent area significantly influences the pressure bearing capacity of the pipelines [74-76]. The main standards for assessment of combined defects include ASME B31.8, ASME B31G, and API 579. Geometric parameters such as three-dimensional sizes of the gouges, corrosion defects and cracks are needed to conduct the failure assessment procedure [1].

2.2.1 Plain dent

For assessment of a plain dent, the dent depth is the most direct geometric parameter. However, it is reported that depth of a dent rarely affects the bearing capacity of internal pressure even when the dent depth exceeds 20% of the pipe diameter [11, 12, 73]. Moreover, even the dent depth is less than 6% of the pipe outer diameter, the pipelines still tend to fail due to initiation of cracks [48].

Table 2.1 Standards and methods used for assessment of plain dents and a dent combined with other types of defects on pipelines [13, 24, 43, 44].

Standard	Plain dents	Dent with corrosion	Dent with crack
ASME B31.4	Dent depth < 6% OD	Corrosion defect is accessed by ASME B31.G	Repair
ASME B31.8	Circumferential bending strain $\varepsilon_1 = (1/2)t(1/R_0 - 1/R_1)$ (2.1) Longitudinal bending strain $\varepsilon_2 = -(1/2)t/R_2$ (2.2) Longitudinal extensional strain $\varepsilon_3 = (1/2)(d_D/L)^2$ (2.3) Equivalent strain on the inside pipe surface $\varepsilon_i = \left[\varepsilon_1^2 - \varepsilon_1(\varepsilon_2 + \varepsilon_3) + (\varepsilon_2 + \varepsilon_3)^2\right]^{1/2}$ (2.4) Equivalent strain on the outside pipe surface $\varepsilon_o = \left[\varepsilon_1^2 + \varepsilon_1(-\varepsilon_2 + \varepsilon_3) + (-\varepsilon_2 + \varepsilon_3)^2\right]^{1/2}$ (2.5) Maximum equivalent strain < 6% Or dent depth < 6% OD	Repair	Repair
CSA Z662	Dent depth < 6% OD and length/depth < 20 or the maximum equivalent strain < 6%	Accessed by ASME B31.G for corrosion between 10 to 40% of wall thickness	Repair
49CFR 192	Dent depth < 6% OD	6% OD and metal loss per corrosion criterion	Repair
49CFR 195	Dent depth < 6% OD	Repair	Repair
API 1160	Dent depth < 6% OD	Immediate repair, unless engineering evaluation shows not an immediate risk	Repair
UKOPA	Dent depth < 7% OD or strain < 6%	Corrosion depth < 20% wall thickness	Repair

where OD is outer pipe diameter, R_o, R_1 and R_2 are initial outer radius of the pipe, outer radius of curvature of the pipe in transverse plane across the dent, and outer radius of curvature of the pipe

in longitudinal plane through the dent, respectively, t is pipe wall thickness, L is dent length in longitudinal direction, d_D is dent depth, ε_1 and ε_2 are bending strains in the circumferential and longitudinal directions, respectively, ε_3 is extensional strain in the longitudinal direction, and ε_i and ε_o are inside and outside equivalent strains, respectively.

The strain-based criterion for plain dent assessment in ASME B31.8 is considered to be more accurate [45]. The parameters required in the strain calculation, as included in Fig. 2.1, include the dent depth d_D, length L of the dent in axial direction, initial pipe surface radius R_o, external surface radius of curvature R_1 in the transverse plane through the dent, and external surface radius of curvature R_2 in the longitudinal plane through the dent. The surface radius of curvature, R_s, can be calculated by:

$$\frac{1}{R_s} = \frac{d^2y/dx^2}{\left[1+\left(dy/dx\right)^2\right]^{3/2}} \tag{2.6}$$

where R_s is the radius of curvature R_1 or R_2, and y is the function of the contour of the dented area with the variable x. Measuring the profile of the dented area is necessary to determine the function of the geometric shape for determining the radius of curvature by Eq. (2.6).

The theoretical basis of Eqs. (2.1) ~ (2.5) is the thin plate model [78], in which the total strain is divided into axial and circumferential bending strains and membrane strains. The further assumption is that the circumferential membrane strain is ignored due to a negligible change of the transverse girth for dented pipelines. However, this assumption is questionable. Through FE analysis and full-scale tests on dented pipelines [49], it is found that, when the dent is deep, the

circumferential membrane strain cannot be ignored. Investigations indicates that the membrane strain formula in ASME B31.8 is not accurate because of an inadequate analogy to radial strains in a circular plate [49]. Studies on strain calculations are carried out by Lukasiewicz et al. [49], who improves the accuracy of the formulas of equivalent strain according to a large deformation thin shell theory:

$$\varepsilon_{\mathrm{eq}} = \frac{2}{\sqrt{3}}\left[\varepsilon_x^{\,2} + \varepsilon_x \varepsilon_y + \varepsilon_y^{\,2}\right]^{1/2} \tag{2.7}$$

where $\varepsilon_{\mathrm{eq}}$ is the equivalent strain, ε_x and ε_y are strains in axial and circumferential directions which can be calculated by:

$$\varepsilon_x = \varepsilon_x^{\mathrm{m}} \pm \varepsilon_x^{\mathrm{b}} \ , \ \varepsilon_y = \varepsilon_y^{\mathrm{m}} \pm \varepsilon_y^{\mathrm{b}} \tag{2.8}$$

The superscript “m” denotes the membrane strain and “b” denotes the bending strain. The sign would be positive when considering the strain of inner surface, and negative for outer side. There is no theoretical foundation for the equivalent strain calculation in ASME B31.8, whereas Eq. (2.7) is derived based on the plastic strain theory with the presupposition that the volume of the material remains constant during the deformation ($\varepsilon_x+\varepsilon_y+\varepsilon_z=0$).

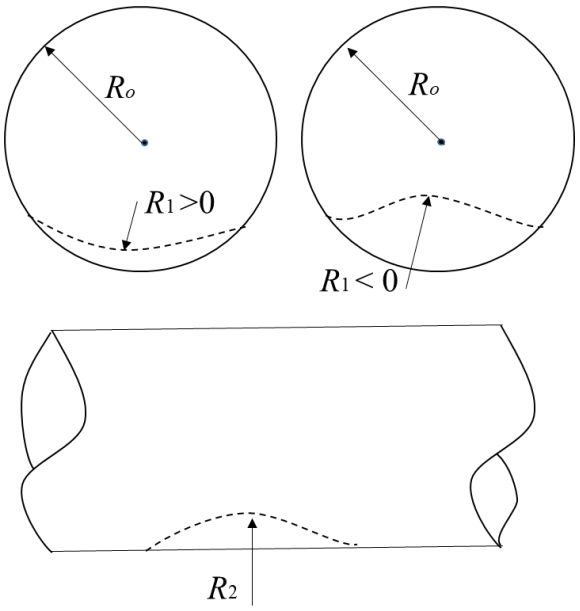

Figure 2.1 Sketches of a dented pipeline [77].

2.2.2 Corrosion in dent

Corrosion is one of the primary mechanisms causing pipeline failures [1, 79, 80]. As the main form of metal loss defect, both uniform corrosion and localized corrosion are commonly present on pipelines. Moreover, pipeline corrosion can happen internally and externally. A big decrease of pipe wall thickness due to corrosion will greatly influence the mechanical performance of pipelines, such as burst pressure, fatigue life and plastic fracture resistance [81]. Qin and Cheng [1] reviewed defect assessment techniques for corroded pipelines. For dented pipelines, corrosion tends to preferentially occur in the dent area due to a high local stress and, sometimes, an aggressive environment generated at the dents [82, 83].

The ASME B31.8 suggests that, for a combined dent with corrosion, the safety assessment should be performed separately. The dent, which is regarded as a plain dent, is assessed by the strain-based criterion, and the corrosion defect is assessed by ASME B31G [84]. In standards like

CSA Z662 and UKOPA, the depth-base criterion is used for dent assessment. Among various standards, the ASME B31G is most used, where the burst pressure, S_F, is determined by:

$$S_F = S_{flow}\left[\frac{1-\frac{2}{3}(d_c/t)}{1-\frac{2}{3}(d_c/t)/M}\right] \quad M=\sqrt{1+0.8z} \tag{2.9}$$

where $z=L_c^2/D_o t$, L_c is longitudinal length of the corroded area, and d_c is corrosion depth. Eq. (2.9) is applicable for $z\leq 20$. When $z>20$, the burst pressure is determined by:

$$S_F = S_{flow}\left(1-d_c/t\right) \tag{2.10}$$

The flow stress S_{flow} is set as 1.1×SMYS (specific minimum yield strength). A modified version of ASME B31G defines that, for $z\leq 50$,

$$S_F = S_{flow}\left[\frac{1-0.85\,d_c/t}{1-0.85d_c/(Mt)}\right] \quad M=\sqrt{1+0.6275z-0.003375z^2} \tag{2.11}$$

For $z>50$, $M=0.032z+3.3$. It is noted that the assessment methods listed above is categorized as Level 1, and the profile of the corroded area is treated as parabolic ($z\leq 20$) or rectangular ($z>20$). In the modified method, the corrosion profile is regarded as a mixed type of geometric shape [1]. Circumferential geometry of the corrosion area is ignored. In addition to ASME B31G, the

standards such as DNV-RP-F101 and API 579 assess corrosion defects in similar formulas with different *M* factors and flow stresses.

2.2.3 Dent with cracks

Cracks represent the most dangerous feature to pipeline integrity [85]. Cracks usually initiate at irregularities such as dents on pipe surface and serve as stress risers, especially at crack tips. Crack growth due to steel yielding and plastic deformation can be induced by a high stress concentration. For pipelines containing cracks, prediction of the burst pressure depends on geometry of the cracks, such as crack depth, width and length, as well as the direction of crack propagation. Compared with cracks with other orientations, the longitudinal cracks which are perpendicular to the primary stress (i.e., hoop stress) resulted from internal pressure are generally more dangerous [86]. Commonly used standards for crack assessment include API 579 and BS 7910 [87], where the failure assessment diagram (FAD) is used. There are three levels of assessment. In API 579, Level 1 and Level 2 assessments are applicable for cracks that become arrested and stop growth under given loading conditions and service environments. Critical length and depth of the cracks are considered in Level 1 to estimate severity of the damage. In Level 2, the stress intensity factor is determined for assessment. The crack dimension obtained from ILI data is used in calculations of local stress and then the corresponding stress intensity factor. The FAD is used to determine if the cracks are acceptable. Sometimes, the critical crack length can also be predicted by FAD in Level 2. Fig. 2.2 shows a typical FAD recommended by API 579, where K_r is toughness ratio and L_r^p is load ratio (API /ASME 579-1/FFS-1, 2016) [88]. If a point is on or inside the FAD, the crack size under the given conditions is acceptable.

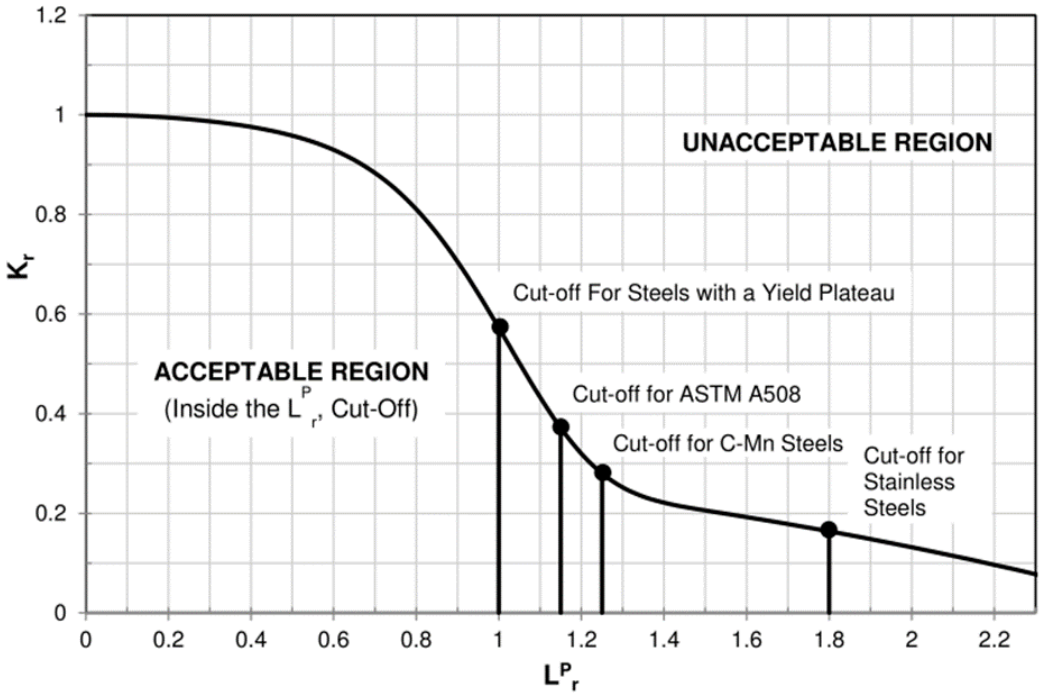

Figure 2.2. A typical FAD recommended by API 579 for crack assessment [88].

Dents on a pipeline are usually accompanied with cracks, where a high strain occurs during formation of dent or due to preferential corrosion, mechanical damage or cyclic loading [89]. Field experiences on dented pipeline show that cracks can initiate even when the dent was shallow [48]. Although a plain dent contributes little to failure of pipelines, but the cracks initiating in the dent area remarkably degrade the pipeline integrity [90]. In addition, the external coating can be damaged during denting. As a result, a corrosive environment will form, which, combined with the stress concentration at the dent, causes stress corrosion cracking (SCC). A widely cited concept of the M-E Interaction explains pipeline SCC initiating at dents due to a synergism of local stress or strain and electrochemical corrosion reaction [24].

A combination of dent and cracks is not allowed in most standards. Once one or more cracks are detected at a dent, remediations or replacements will be required. Due to the limited resolution and accuracy of ILI tools, most cracks cannot be easily found until pipeline leaking, or other failure

modes happen. Standards such as 49 CFR 192 (gas pipelines) and CFR195 (liquid pipelines) do not include sufficient methods for assessment of the dent-crack combination. For gas pipelines, an immediate repair is recommended. For liquid pipelines, cracks combined with a dent on the upper 2/3 of the pipeline needs to be repaired immediately and otherwise, a service for 60 days is acceptable [13]. ASME B31.8 states that a dented pipeline with cracks less than 12.5% of pipe wall thickness can be removed by grinding. It is also found [43] that the burst pressure of pipelines is rarely affected when the crack depth is small; while when the crack exceeds 40% of the pipe wall thickness, the burst pressure decreases by 55%.

2.2.4 HE of dented pipelines

An assessment system of hydrogen pipelines included in standards by determinations of material properties in hydrogen environments. The HE susceptibility of steels is evaluated using the method in ASTM G142 [91, 92], in which the indicators including yield strength, ultimate tensile strength, notch tensile strength, the reduction in area and elongation. These indicators can be measured by tensile testing of smooth or notched specimens. Crack propagation behavior demonstrations using slow strain rate test, four-point bending test or crack tip opening displacement test can be found in standards such as ASTM F1624, ASTM F1459 and NACE TM0284 [93, 94], where the HE measurements in both aqueous and gaseous environments are considered.

For the design, manufacture and assessment of hydrogen pipelines, the ASME B31.12 provides criteria and methods as the guidance [93]. When the dent forms on the pipelines, it is required that the dent depth should not exceed 6% of the nominal pipe diameter or the strain should be less than 2% [95].

2.3 Commentary remarks on existing standards and the improvements

As shown in Table 2.1, the present standards for pipeline dent assessment mostly focus on the plain dents. For dents combined with other types of defects, there has been no reliable method available for accurate assessment. Moreover, the existing standards and methods are usually conservative and suffer from certain limitations in dent assessment. A further improvement on dent assessment techniques, especially for dent-defect combinations, is critical to pipeline integrity and safety.

Nowadays, modifications on plain dent assessment have mainly focused on implementation of the strain-based criterion to replace the commonly used depth-based criterion. The depth-based methods are mostly empirical and do not have sufficient theoretical support. Thus, they can only be used as the Level 1 assessment. Instead, more information can be obtained from strain analysis at a dent, such as cracking prediction [43]. Three improvements have been achieved, i.e., methods for strain calculation, estimations of dent profile, and pipeline failure criteria.

The ASME B31.8 introduces the strain-based criterion for dent assessment. However, many problems still exist. First, it assumes that the maximum bending and membrane strains are located at the center of a dent [45]. However, both experimental testing and FE analysis indicate that the maximum strain is not always at the dent center [96]. As the dent depth increases, the location of the maximum strain moves from the center of the dent to the edge [11, 97]. It means that the failure assessment based on strain calculation at the dent apex will give misleading information, especially for deep dents. Second, the formulas in ASME B31.8 are confusing. For example, the formulas for bending and membrane strains are from empirical methods. The FE analyses have shown that the formulas can have predictable erroneous strains [98]. Moreover, there is no clear explanation about

the origin of the empirical equivalent strain equations [78]. Third, an important assumption in the standard is that the membrane strains in circumferential and radial directions and the shear strain are negligible [45]. Nevertheless, denting is a plastic deformation on pipelines, where the plane strain assumption is not proper. Finally, for unconstrained dents, there will be a re-rounding process after denting, during which the dent depth and strain will decrease. The maximum deformation during the denting cannot be accurately estimated by ASME B31.8 [45]. In summary, the strain-based method in ASME B31.8 cannot provide accurate and reliable results for dent assessment and pipeline failure prediction.

Lukasiewicz et al. [49] proposed more accurate formulas based on the theory of large deformation of cylindrical shell. The bending strains in longitudinal and circumferential directions can be calculated by following equations.

$$\varepsilon_x^{\mathrm{b}} = \frac{t}{2}\frac{\partial^2 w}{\partial x^2} \ , \ \varepsilon_y^{\mathrm{b}} = \frac{t}{2}\frac{\partial^2 w}{\partial y^2} \tag{2.12}$$

where w is the pipe wall deflection in the radial direction. The profile functions in longitudinal and circumferential directions are defined as u and v. Then the membrane strain $\varepsilon_x^{\mathrm{m}}$, $\varepsilon_y^{\mathrm{m}}$ and shear strain γ_{xy} can be derived by following equations.

$$\begin{aligned} &\varepsilon_x^{\mathrm{m}} = \frac{\partial u}{\partial x} + \frac{1}{2}\left(\frac{\partial w}{\partial x}\right)^2 + \varepsilon_x^{\mathrm{o}} \ , \ \varepsilon_y^{\mathrm{m}} = \frac{\partial u}{\partial y} + \frac{w}{R} + \frac{1}{2}\left(\frac{\partial w}{\partial y}\right)^2 + \varepsilon_y^{\mathrm{o}} \\ &\gamma_{yx} = \frac{\partial u}{\partial y} + \frac{\partial v}{\partial x} + \left(\frac{\partial w}{\partial x}\right)\left(\frac{\partial w}{\partial y}\right) \end{aligned} \tag{2.13}$$

where ε_x^o and ε_y^o are the initial strain due to the pressure in the pipe in axial and circumferential direction. The equivalent strains can be estimated by Eq. (2.7). Compared with the method in ASME B31.8, Lukasiewicz method has better accuracy and ASME B31.8 method underestimates the equivalent strain [78]. The failure critical strain for strain-based assessment is 6% in ASME B31.8 which is also an empirical assumption. Different failure criteria are proposed based on various failure mechanisms, such as Oyane plastic failure criterion, ductile failure damage indictor (DFDI) criterion, strain limit damage (SLD), plastic collapse strain criterion, and remaining fatigue life criterion.

2.3.1 Ductile damage criteria: Oyane plastic failure criterion and DFDI

Ductile damage results from the accumulation of plastic deformation is one of the damage forms for pipelines which will induce cracking of the steel until fracture [99]. Oyane et al. [100] took the cumulative damage into account during the deformation and proposed the failure criterion.

$$I = \frac{1}{C_2}\int_0^{\varepsilon_{eq}} \left| \frac{\sigma_m}{\sigma_{eq}} + C_1 \right| d\varepsilon_{eq} \tag{2.14}$$

where C_2 is the elongation rate for the material measured in the uniaxial tensile test and constant C_1 is obtained through a burst test on a non-indented pipe; I is the integral value that can be used as the damage indicator; σ_m is the average stress; σ_{eq} and ε_{eq} are equivalent stress and strain respectively. When the indicator I=1, ductile fracture will occur [14, 101]. For X52 steel, C_1=0.227 and C_2=0.3 [102].

The DFDI criterion is built on the understanding that the growth of micro-cracks in the ductile solids is a common reason for the material fracture [103]. The DFDI criterion can be expressed as:

$$DFDI = \int_0^{\varepsilon_{eq}} \frac{d\varepsilon_{eq}}{1.65\varepsilon_d \exp\left(-\frac{3}{2}\frac{\sigma_m}{\sigma_{eq}}\right)} \tag{2.15}$$

where the value of ε_d should be measured by the uniaxial tensile tests as which were conducted by Gao et al. [13] and Arumugam et al. [104]. For X52 pipeline steel, ε_d is 51.2%. Similarly, the plastic fracture is believed to take place when *DFDI* value equals to 1. Both Oyane criterion and DFDI criterion are validated in experimental and FE methods to effectively predict the cracking of the material [101, 104]. Furthermore, the formation of dented pipeline is a plastic deformation process for which the plastic fracture failure criteria are suitable for the assessment [103].

2.3.2 Other criteria for plain dent assessment

The SLD, as recommended by ASME [13], uses elastic-plastic FE analysis to estimate the accumulated plastic damage on pressure vessels, including pipelines:

$$D_{et} = D_{eform} + \sum_{i=1}^{NL} D_{e,i} \leq 1 \tag{2.16}$$

where D_{et} is an indicator of the limit state for a structure such as pipeline to carry no further loads, D_{eform} is the damage resulted from deforming, *NL* is the number of load increments and $D_{e,i}$ is the damage during the i^{th} load increment, which is associated with the total plastic strain and stress.

When D_{et} exceeds 1, the load capacity of the structure reaches its limit. The SLD criterion is based on the minimum reduction area and elongation to failure, while the properties of the material are not required. The stress and strain data used in the criterion is obtained from FE analysis.

The net section failure criterion is a stress-based criterion, which specifies that the minimum von Mises stress in the dent area should not exceed the flow stress, $\sigma_f=(\sigma_y+\sigma_U)/2$ [105]. The plastic collapse strain criterion is commonly used in pressurized structures like pipelines. The plastic collapse state is defined as the point of intersection on the load-displacement curve between the peak and a line drawn from the origin with a slope twice of the elastic slope (TES) [18]. It is effective to use the plastic collapse criterion to assess dented pipelines where a large plastic deformation occurs [106].

Methodologies for fatigue life assessment of dented pipelines are summarized and compared in Ref. [107], where EPRG 1995 and EPRG 2000 are thought as the best empirical methods in terms of the quality-of-fit to published full-scale test data [13]. Fatigue life of a pipeline containing an unconstrained dent is determined by the cycles of circumferential stress, N, and the stress concentration factor, K_{sc}:

$$K_{sc} = 2.871 \cdot \sqrt{d_D \cdot t / D_o} \tag{2.17}$$

$$N = 1000 \cdot \left(\sigma_u - 50\right) / \left(2 \cdot \sigma_{FS} \cdot K_{sc}\right) \tag{2.18}$$

where d_D is dent depth, t is pipe wall thickness, D_o is pipe outer diameter, and σ_{FS} is fatigue strength. Stress-life fatigue design equations were used by Petrobras [107] to estimate the fatigue life of dented pipelines, where the stress concentration factor was limited to the linear elastic stage. The fatigue limit of pipeline steels is assumed to be attained at 10^6 cycles.

$$K_{sc} = A_P + B_P \left(\frac{d_D}{D_o} \right) \left(\frac{D_o}{t} \right)^{1.14} \tag{2.19}$$

$$N = \sigma_a^{1/b} \cdot \left[C_P \left(1 - \left(\sigma_m / \sigma_U \right)^2 \right) \right]^{-1/b} \tag{2.20}$$

where A_P, B_P and C_P are coefficients, which depend on dent geometry, pipe dimension and steel properties, respectively, and σ_a and σ_m are alternating stress and mean stress, respectively. Both EPRG methods and the Petrobras model are stress-based.

A strain-based model was proposed for fatigue life assessment of dented pipelines [13]:

$$\Delta\varepsilon = 3.5 \frac{\sigma_U}{E} N^{-0.12} + e_0 N^{-0.6} \tag{2.21}$$

where $\Delta\varepsilon$ is the cyclic strain range, E is elastic modulus, and e_0 is true strain to failure. The cyclic strain range at the dent can be obtained by FE analysis.

2.3.3 Corrosion in dent

The main harm of the corrosion to the pipeline is the thinning effect on the wall thickness. Thus, the most direct failure is the decreasing of the pressure capacity of the pipeline with high pressure [56]. Most of the existed assessment criteria have similar formations that are developed based on experimental tests [108, 109]. However, the development and validation of the criteria in codes are accomplished by tests on low grade steels such as X42 to X52 steel [1, 110]. Assessment methods on high grades such as X80, X100 are less studied. Another important characteristic for

corrosion is the continuing development during the operation in corrosive environment. The growth rate is a critical factor for the service life of corroded pipelines. Generally, corrosion rate is considered to be related to the corrosive solution, pipeline material and electrochemical environment etc. According to the mechano-electrochemical interaction theory, the stress and strain conditions of corrosion area can affect the corrosion rate. From experiments and FE simulations in literature [24, 111, 112], it is concluded that in the near-neutral pH solution, the plastic stress can remarkably enhance the growth rate of corrosion defect, while the elastic stress has limited effects.

2.4 Existing experimental testing for dent assessment of pipelines

2.4.1 Plain dent

Plain dent, as the simplest defect on pipelines, has been extensively investigated experimentally. Burst tests are conducted to determine the internal pressure capacity of a dented pipeline. The general procedure includes selection of a pipe segment, denting, and the burst pressure loading. To perform burst testing, caps are required to install at both ends of the pipe, while the influence of the caps should be eliminated by adjusting the ratio of the pipe length to the outer diameter. Generally, the burst pressure of the dented pipeline is not affected by the plain dent. To obtain the relationship between the indenter displacement (i.e., the dent depth) and the load applied on the pipe, a typical dent depth vs. load curve is obtained. The strain at the dent area varies during denting. Upon removal of the indenter for unconstrained dents, the re-rounding process also changes the strain distribution. The strain at the dent during denting and re-rounding cannot be directly measured. Strain gauges placed in the dent area will fail when the indenter loads on them [113]. Thus, there were work installing strain gauges on the pipe body outside the dent in

both circumferential and longitudinal directions to measure strain variations during the denting process [114].

The mechanical properties of pipe steel at the dent area are affected by shape, depth and length of the dent. For rectangular and spherical dents, a local strain as high as 29.6% could cause pipeline leak or rupture [113]. Generally, under identical conditions, a high strain was detected at a rectangular dent than a canoe shape dent [115].

2.4.2 Plain dent combined with corrosion

Corrosion tends to preferentially occur at a dent on pipelines. This is attributed to an enhanced local electrochemical activity. While corroded pipelines have been widely tested and assessed, the corrosion defects are usually made artificially with a regular profile, which is not consistent with real corrosion defects [115-117]. ILI tools have a limited capacity to distinguish corrosion and gouge [13]. The two different types of metal loss affect the pipeline integrity at different mechanisms and severities. Compared to the gouge defect, corrosion is a time dependent process [80]. Even when the metal loss is not obvious for a corrosion pit at a given instant, the further growth of the pit in corrosive environments can penetrate the pipe wall and cause leaking rapidly. The enhanced corrosion at dents can be explained by the M-E Interaction concept developed by Cheng group [22, 25, 111]. Basically, the full-scale tests conducted on a pipe with corrosion in dents have been limited.

2.4.3 HE occurring on dented pipelines

Nowadays, a reliable method for assessing the HE susceptibility of hydrogen pipelines has not been established [93]. Questions such as the exact mechanisms of H diffusion and trapping in

steels, hydrogen-induced crack initiation and propagation, critical service conditions such as pressure and pressure fluctuations, and the effect of defects such as dents on pipeline HE are to be understood and answered. Two HE mechanisms have been widely accepted to explain the hydrogen-induced cracking behavior, i.e., hydrogen enhanced decohesion (HEDE) and hydrogen enhanced localized plasticity (HELP) [93, 118]. It is assumed in the HEDE mechanism that the lattice cohesive strength of the steel is weaken by the interstitial H atoms, inducing the decohesion of Fe lattice structure. For HELP theory, the plastic flow of the steel is enhanced by H atoms because that the mobility of dislocations is increased by the H-reduced elastic energy for dislocation movement. Four stages are defined in the process of H atoms generating from H_2 gas and diffusing into the steel, as shown in Fig. 2.3.

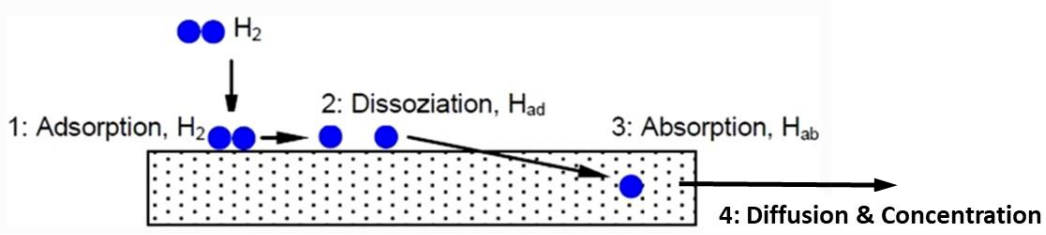

Figure 2.3. Sketch of the process of H atoms diffusion and concentration in steel.

Atomic H can diffuse and reside in normal interstitial lattice sites and metallurgical traps. The trapping sites can be dislocations, grain boundaries, phase interfaces, secondary phase particles, etc. Generally, the traps are categorized as reversible and irreversible types based on their binding energies (W_B). When $|W_B|$ is more than 60 kJ/mol, the traps are irreversible and H atoms cannot leave the traps at room temperature. When $|W_B|$ is less than 30 kJ/mol, the traps are regarded reversible, and H atoms can be released even at room temperature [68]. The effect of H atoms on mechanical properties of steels and the interaction between H and fatigue have been investigated

in both aqueous and gaseous environments [119-122]. Tensile testing results obtained on H-charged pipeline steel specimens showed that H atoms do not influence the elastic modulus, yield stress and ultimate tensile strength of the steels [61, 91, 123]. However, the ductility is reduced more than 20% in terms of the reduction in area at fracture surface compared with the H-free specimens [70]. The fracture toughness measured in hydrogen gas environments reduces to 48–60% of the fracture toughness obtained in air. The fatigue resistance of pipeline steels in gaseous hydrogen environments can be noticeably reduced, and the fatigue crack growth rate is remarkably accelerated by hydrogen exposure than in air [29, 122, 124]. Quantitative relationships were proposed to predict the hydrogen induced fatigue crack growth rate [6, 34, 63, 125, 126].

In pipelines transporting hydrogen in blended form, the partial pressure of hydrogen gas is another important factor affecting fatigue cracking. Tensile and fatigue tests were conducted to investigate the fatigue resistance and crack growth rate of an X80 pipeline steel under a total 12 MPa pressure mixed with hydrogen with a partial pressure of 0.6 MPa [122, 124]. Hydrogen exhibited an obvious effect on both crack initiation and growth. It is further found [61, 127] that a low concentration of hydrogen blended in natural gas cannot affect mechanical properties of pipeline steels at an obvious level.

2.5 Finite element methods used in dent assessment on pipelines

2.5.1 General simulation of the denting process

Denting is an elastoplastic deformation process, and contains the following three steps which are identical to the experimental procedure [11, 14, 103, 106, 128-131]:

a) Denting: The indenter is placed on the pipeline model. Then downward displacement load is applied on the indenter by small increments until the set value of depth reached.

b) Spring-back: For unconstrained dent, the indenter should be removed upward and the dent area will have a spring-back process.

c) Loading: Static pressure is performed on the internal surface of the pipeline to test the burst pressure. Other kinds of loads can also be applied such as bending moment and external loads.

2.5.2 Denting model validation

Comparison between the numerical simulation and test results is the mostly used validation method. Strain gauges cannot be attached during denting, but other parameters can be used to validate the FE modeling, such as the relationship between reaction force and displacement of the indenter during denting and removing of the indenter [131, 132].

2.5.3 Burst modeling of dented pipelines

For dented pipeline in burst test, in step (c), the pipeline is applied with increasing internal pressure until the pipeline fails. Literature shows that the plain dent has limited influence on the burst pressure of the pipeline which has been validated by both experimental and numerical methods [11, 12]. Corrosion defect can be numerically simulated as the single pit, long groove and the large area corrosion in FE analysis [81]. Basic parameters to determine the corrosion defect profile are the depth, width and length of the corrosion [44]. Besides, the "element death" technology also can be used to build the model of corrosion [10]. Burst pressure is the main criterion for the assessment of the residual strength of the corroded pipeline. Numerical analysis errors of the burst of the corroded pipeline are acceptable [133]. Numerous research of the pipeline subjected to the corrosion defect existed in the literature, nevertheless, the investigations of the dented pipeline combined with corrosion defect still need further development.

Modeling of cracks in pipelines by FE is challenging, while some progresses have been made in the recent years. Bedairi et al. [87] investigated cracks in corrosion area by modeling the crack tip as a blunt notch with a specific radius of the size of the plastic zone. V-shape notch was used by Ghaednia et al. [134] to model cracks in pipelines, where the grids in crack area were properly adjusted. Another method to model pipeline cracks is the so-called extended FE method [135]. A pipe with a crack can be modeled by shell and solid elements. The shell element was used to model the pipe body, and the solid element modeled the crack. The shell-solid coupling constraint was utilized to attach the shell elements with the solid elements. A dent can be produced by applying load of the indenter.

2.5.4 FE modeling of H diffusion and HE behavior

Finite element method is an efficient tool modeling the H diffusion and the HE behavior of steels. Extensive studies have been performed to determine the hydrogen diffusion at metallurgical defects and crack-tip [29, 119, 125, 136]. Pipeline is under pressure fluctuations during normal operation. Numerical analysis shows that the pressure fluctuations of the pipelines accelerated the hydrogen-induced fatigue crack growth [68]. However, limited investigations have been reported for the H atom distribution at a dent on pipelines, especially under pressure fluctuations.

For HE of steels, the sharp crack topology induces discontinuity and singularity, which are main barrier for cracking assessment. Two numerical algorithms for cracking of materials are developed and can be classified as the discontinuous and continuous methods, respectively [137]. Representatives of the discontinuous method include the extended finite element method (XFEM) [138, 139] and the boundary element method [140]. The basics of the discontinuous methods is to directly simulate the crack topology through specific criteria, leading to a strong discontinuity in

the displacement field [137]. Additional rules are required for the crack initiation and propagation which causes further difficulties in FE simulations [141]. One of the popular continuous models for fracture mechanism is the phase field (PF) method, which predicts cracking by smearing the discontinuity of crack geometry over a band through the characteristic length scale l_0 [142]. As a result, the pre-existing crack is not necessary for fracture analysis, while the initiation of cracks can be forecasted [143]. Extended from the Griffith fracture theory, the PF method indicates that the crack grows if the energy release rate reaches a critical value. The path of crack growth is involved with the maximum energy dissipation path in the displacement field during the loading process [144]. Particularly, the crack initiation and propagation with an arbitrary path can be effectively predicted via the PF method [145]. Elastic strain energy is considered during deformation of the material and thus, the early PF method is only available for brittle fracture such as the fracture of concrete, ceramics and brittle metals [146, 147]. However, for pipeline steel, the elastic plastic fracture occurs inevitably during the crack initiation and growth, which greatly restrict the application of PF method in engineering. Extensions of the PF method from the brittle fracture to elastic-plastic fracture were promoted by Miehe et al. [146, 148, 149] and Ambati et al. [141, 150], by introducing the plastic strain energy into the total deformation energy dissipation. Advancement in both theoretical and computational techniques provides the basis for elastic-plastic fracture analysis using the PF method [71, 149, 151, 152].

Chapter Three: A new criterion based on strain determination for dent assessment of pipelines[†]

3.1 Introduction

To date, as reviewed in Chapter Two, relevant studies on failure assessment of dented pipelines have been limited, and the existing standard, mainly ASME B31.8, contains problems, making assessment results not sufficiently accurate and reliable. In this work, a ductile damage failure assessment was combined with a FE model for dent assessment on an X52 steel pipeline.

The indentation and spring-back process, as well as strain distribution at the dent were modeled based on the geometric parameters included in Ref. [11]. The modeling results were validated with previous experimental measurements and modeling data. The dent assessment results were compared with the calculations by ASME B31.8 standard, where the essential problems in strain calculation were analyzed. The DFDI criterion was modified, which was combined with FE modeling of local strain, to be used for accurate dent assessment and failure prediction on pipelines.

3.2 Numerical modeling

3.2.1 Material properties of X52 steel

The API X52 steel, one of the most widely used materials in pipeline industry, was used in this work. The mechanical properties of the steel are listed in Table 3.1 [11], where E is elastic

[†] The work in this chapter has been published as:

Jian Zhao, Y. Frank Cheng, A new criterion based on strain determination for dent assessment of pipelines, *Journal of Pipeline Science and Engineering*, 2 (2022) 18-28. https://doi.org/10.1016/j.jpse.2021.11.004

modulus, υ is Poisson's ratio, σ_y is yield strength, σ_U is ultimate tensile strength, and δ is maximum elongation under uniaxial tensile testing.

Denting on a pipe is a permanent deformation process including both elastic and plastic stages. True stress-strain behavior of X52 steel should be used in FE modeling. The Ramberg-Osgood (R-O) material model can fit the stress-strain curve and was used in this work:

$$\frac{\varepsilon}{\varepsilon_0}=\frac{\sigma}{\sigma_y}+\alpha\left(\frac{\sigma}{\sigma_y}\right)^{\beta} \tag{3.1}$$

where σ and ε are stress and strain, respectively, ε_0 is initial strain ($\varepsilon_0=\sigma_y/E$), and α and β are strain-hardening coefficients. In this work, α=1.19 and β=15.6 [153]. Using relevant parameters in Eq. (3.1) and combining with the R-O model, the true stress-strain behavior of X52 steel is derived in Fig. 3.1. It is noted that, while this work is conducted based on the X52 pipe steel, the developed method is applicable to other grades of pipe steel using their specific mechanical properties as input parameters.

Table 3.1 Mechanical properties of X52 pipeline steel used in this work.

Steel	E (GPa)	υ	σ_y (MPa)	σ_U (MPa)	δ (%)
API 5L X52	208	0.3	375	468	22.3

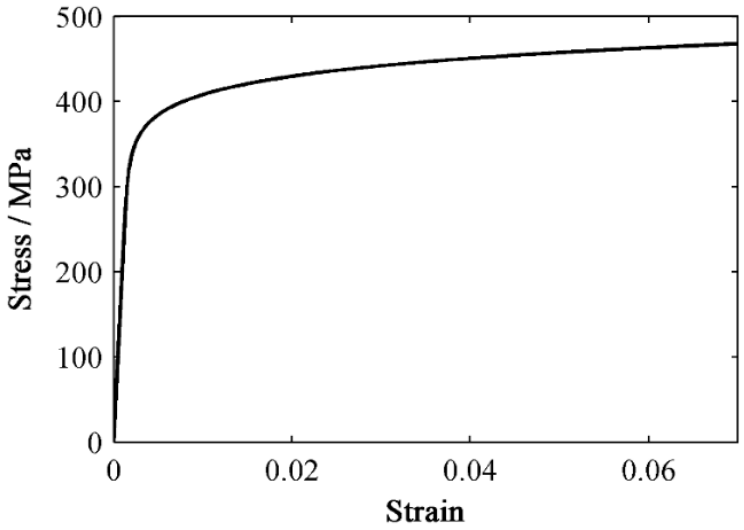

Figure 3.1 True stress-strain curve of X52 pipeline steel.

3.2.2 Finite element modeling

A FE-based model was developed using ANSYS software. The geometric parameters of the modeled pipe segment are consistent with a previous work [11] for convenience to validate the modeling results. The outer diameter of the pipe was 720 mm, and the pipe wall thickness was 8.1 mm. Due to symmetry of the pipe, a quarter model was established as shown in Fig. 3.2 (a). To eliminate boundary effect and simulate the experimental installation reported in [11], the pipe segment to be modeled was 7,466 mm in length, which was about ten times of the pipe outer diameter. An indenter was used with a rigidly spherical shape and a diameter of 100 mm. The X, Y and Z directions referred to the circumferential, radial and axial directions, respectively. It is noted that an actual dent is not always present on the top of the pipe. Moreover, the dent is not necessarily circular. To simplify modeling and generate generally applied results, the indenter used in the work was assumed as spherical, and the dent was created on the top of the pipe segment, as shown in Fig. 3.2 (a). It is noted that an indenter with a geometry other than sphere will affect the shape of the generated dent and thus the induced strain distribution. The FE model can determine

the local strain based on an exact dent profile. However, the modeling process can become more complicated with increased computational time.

The modeling targets includes an elastoplastic deformation and a contact between the indenter and the pipe. It is realized that the modeling was highly nonlinear and complex, and adjustments such as grid density and the contact area are required to promote convergence. To ensure both accuracy and efficiency of the modeling, an eight-node element (i.e., SOLID185) was selected for both the pipe and the indenter. As shown in Fig. 3.2 (b), high-density grids were applied at the dent area to improve the modeling accuracy and convergence stability. The grid size was determined by analysis of the grid density sensitivity. For other area, the grids were relatively coarse to save computational time. The mesh size of the indenter was consistent with the dent area for contact convergence. The pipe wall was divided into three layers of elements. The outer surface of the indenter and the dented area on the pipe were defined as the contact surface and the target surface, respectively. The contact friction factor was set as 0.3.

The boundary condition of the FE model was symmetrical. A displacement constraint was applied on the bottom of the pipe. The ends of the pipe segment were not constrained.

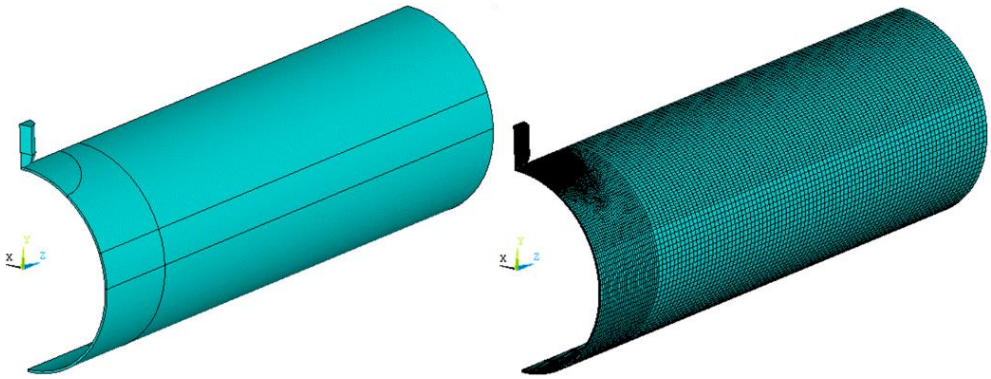

Figure 3.2 (a) A quarter model of the pipe segment and an indenter, (b) grids and refined mesh of the modeled targets in this work.

The dent studied in this work is an unconstrained dent, where the indenter would be removed after indentation. There is potentially a spring-back when the indenter is removed from the dent area. This can decrease the dent depth, depending on the spring-back behavior and internal pressure of the pipe. To approximate the indentation process, the FE modeling contains three steps, i.e., indentation, removal of the indenter, and application of internal pressure.

(1) Set a vertical, downward direction and apply a displacement load on the indenter to reach a pre-set depth, which is called initial dent depth, h_o, on the pipe.

(2) Move up the indenter and eliminate contact with the pipe. Observe the spring-back phenomenon. The dent depth after spring-back is referred as the permanent depth, h.

(3) Apply an internal pressure from low to high value until the steel fails and the pipe burst occurs. It is noted that a pipeline is sufficiently long. To approximate conditions as defined in Ref. [11], equivalent tensile stresses should be employed on both ends of the pipe to simulate the effect of hydrostatic pressure applied on the end-cap in testing. The equivalent axial tensile stress is calculated as $pD_i^2/(D_o^2-D_i^2)$, where p is internal pressure, and D_i and D_o are inner and outer diameters, respectively, of the pipe.

3.3 Model validation and strain determination at the dent

3.3.1 Analysis of grid density sensitivity

The density of grids is a major factor influencing modeling accuracy and time consumption in FE analysis. As stated, the grid density for FE modeling in this work included three levels, i.e., dent area, outside the dent, and the pipe far from the dent. In particular, the number of elements in the dent area is the most important parameter affecting the modeling accuracy, convergence of

nonlinear analysis and computational time. To determine a proper grid size at the dent area, the element size was set from 4 mm to 10 mm, and the von Mises total mechanical strain (i.e., equivalent strain in the following discussions) in ANSYS was calculated at the dent center. Fig. 3.3 shows the equivalent strain at the dent center as a function of the element size. Smaller elements can guarantee the accuracy of FE analysis. However, high element density can result from the small element size and therefore significantly increase the time and resource costs of the calculation. Besides, the equivalent strains in Fig. 3.3 tended to be steady when the element size was approaching 5 mm. Calculation time in this work increased a lot when the element size was smaller than 5 mm. Thus, to balance the modeling accuracy and a reasonable computational time, an element size of 5 mm was selected at the dent area. The element sizes chosen for other segments on the pipe changed from 10 mm to 20 mm with an increased distance to the dent area. The indenter was meshed as 5 mm to ensure a convergence of the contact algorithm.

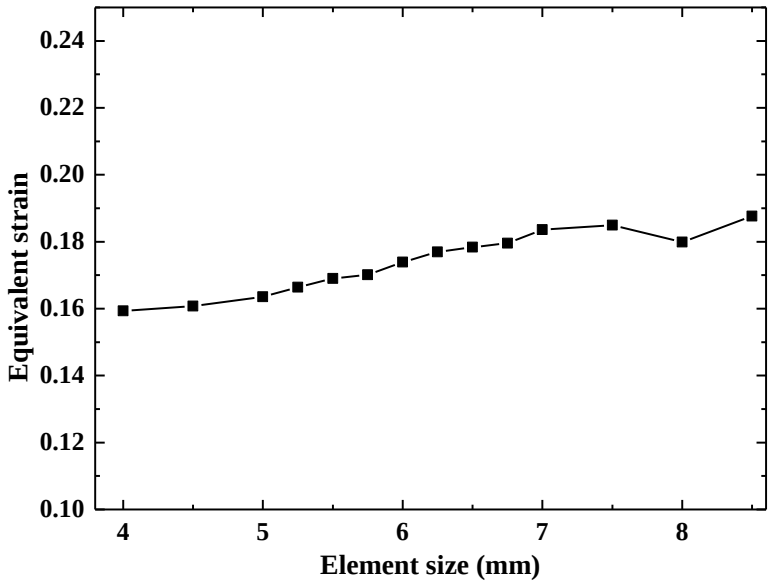

Figure 3.3 Equivalent strain at the dent as a function of the element size for analysis of grid density sensitivity.

3.3.2 Validation of the modeling results

Since the input parameters of the FE model are similar to those used in previous work, the modeling results obtained in this work were validated with both experimental measurements using a strain gauge and modeling data in Ref. [11]. As the strain gauge cannot be placed in the dent area during indentation, the distribution of strain at the dent cannot be measured directly. In experimental testing, the strain gauge was installed on a specimen to record data after the denting process is completed [11]. The recorded strain data did not include residual strain, which should be subtracted from the modeling result.

Fig. 3.4 shows the circumferential and axial strains at the dent apex obtained from FE modeling in this work with previous tests and modeling results [11] under various internal pressures, and Fig. 3.5 shows the axial strain at the pipe segment that is 2,500 mm away from the dent apex. It is seen that the dependences of both circumferential and axial strains on internal pressure obtained by FE modeling in this work have similar tendencies to the reported experimental measurements and modeling results in Ref. [11]. Particularly, the difference between the modeling in this work and the experimental measurements in Ref. [11] is smaller than the deviation of previous modeling results in Ref. [11] from the experimental measurements. The potential sources of error include measurement errors, dimensional errors, and differences in material properties and boundary conditions. In addition, a strain hardening occurring at the dent [12] cannot be simulated by FE modeling, which can cause a small strain under the identical load used in the experiment. The burst pressure determined by FE modeling in this work is 10.32 MPa, while the experimentally measured value in Ref. [11] is 10.72 MPa. The relative difference is

3.73% only. It is thus believed that the FE model developed in the work is reasonable and reliable for strain determination at the dent on pipelines.

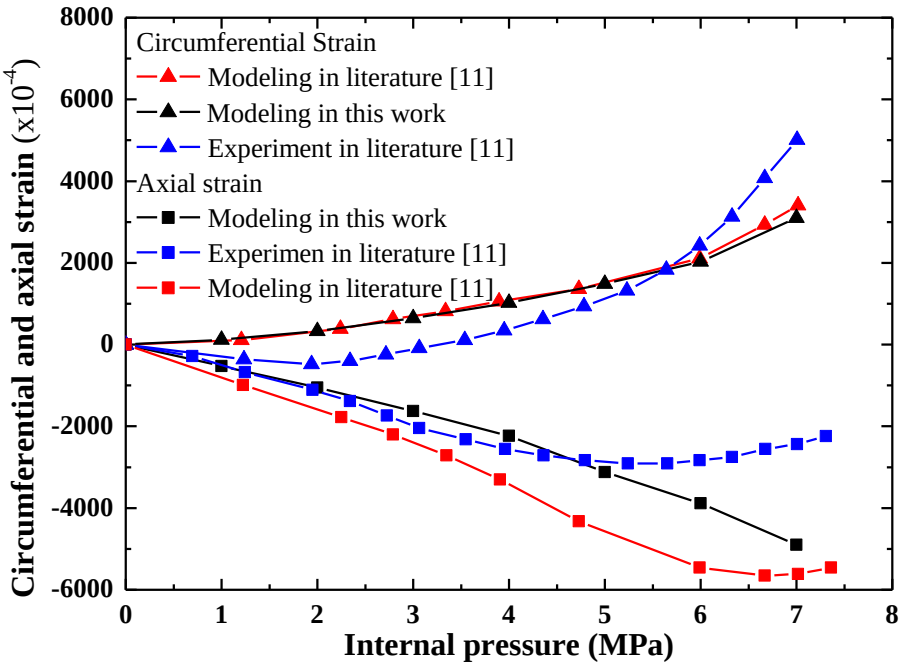

Figure 3.4 Comparison of circumferential and axial strains at the dent apex obtained from FE modeling in this work with previous experimental tests and modeling results [11] under various internal pressures.

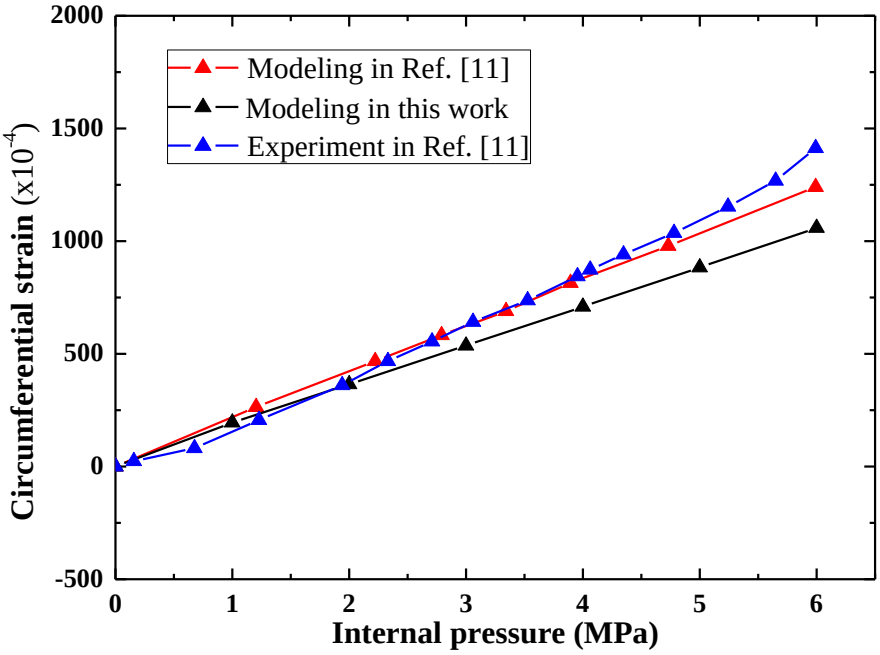

Figure 3.5 Comparison of circumferential strains at the pipe segment that is 2,500 mm away from the dent apex obtained from FE modeling in this work with previous experimental measurements and modeling results [11].

3.3.3 Modeling of indentation and spring-back process

Fig. 3.6 shows the relationship between the indentation load and the indenter displacement (initial dent depth h_o=30 mm) in the absence and presence of an internal pressure of 3 MPa on X52 steel pipe. As indentation is applied on the pipe to increase the indenter displacement, the indentation load keeps increasing. When the indenter was moved upward, the indentation load started to decrease and a spring-back of the dent area occurred. The spring-back process shows a linear relationship, like the stress-strain behavior upon stress-relieving. Residual displacement of the dent area can be observed, which indicates that the denting process is an elastoplastic deformation. Moreover, an apparent difference before and after the application of internal pressure was observed during the indentation and spring-back process. At specific indentation

displacements, a bigger indentation load was recorded in the presence of internal pressure. It is thus believed that the presence of an internal pressure prevents the denting effect on pipelines during indentation. When the indenter was moved, the internal pressure made the dented area spring-back more rapidly. The residual depth of the dent after spring-back is usually shallower in the presence of internal pressure, which is consistent with the report by European Pipeline Research Group (EPRG) [154].

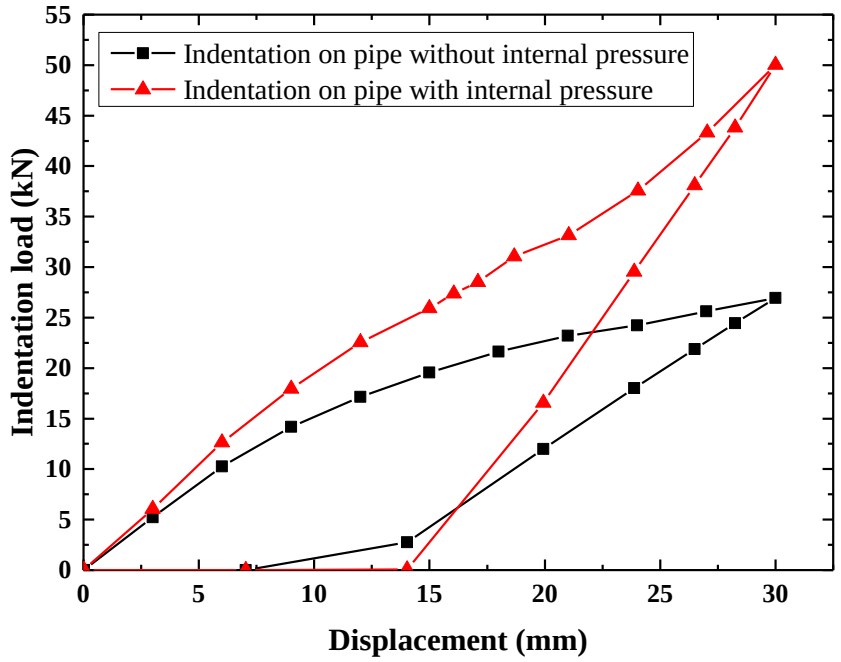

Figure 3.6 Relationship between the indentation load and the indenter displacement (h_o=30 mm) in the absence and presence of an internal pressure of 3 MPa on X52 steel pipe.

3.4 Determination of strain at the dent

To develop a strain-based criterion for dent assessment on pipelines, the strain distribution at the dent and nearby areas should be modeled and determined. Fig. 3.7 shows the distribution of circumferential and axial strains at the dent area during indentation and spring-back process. As

expected, both circumferential and axial strains decrease in response to spring-back. Generally, the circumferential strain of outer surface of the dent is tensile (positive) and the inner surface is under compressive strain. However, for axial strain, the inner surface is in tension and the outer surface is in compression.

To define the detail of strain distribution on the inner surface of the dent, further processing was conducted on the FE model of the dented pipe. Fig. 3.8 presents a partial display of the existing model to show the path selection on the dent area, where point A refers to the dent apex and paths A-B and A-C represent the circumferential and axial directions, respectively, of the inner surface. The circumferential and axial strains as a function of the circumferential angle and axial distance, respectively, after spring-back are shown in Fig. 3.9, where the origin point (i.e., 0° in circumferential angle and 0 mm in axial distance) refers to the dent apex. The circumferential angle cannot be directly determined from the FE model and is to be calculated using a relationship between the arc length (obtained from software) and the radius of curvature. As displayed in Fig. 3.9, the largest circumferential and axial strains are recorded at the dent apex. However, for the equivalent strain, the maximum value is not at the dent apex, but deviates a bit from it. As discussed in the next section, when the dent depth exceeds a certain value, the maximum equivalent strain is not located at the dent apex anymore. The strain tends to decrease and gradually become zero when it is away from the dent center.

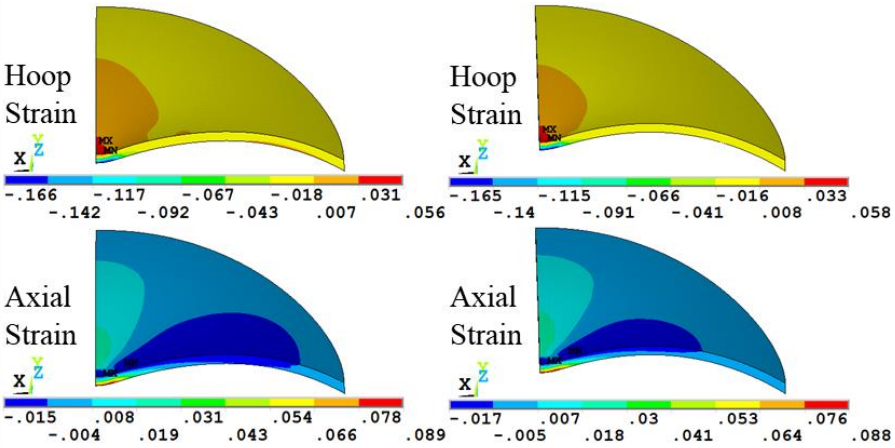

Figure 3.7 Distribution of circumferential and axial strains at the dent area during indentation (left) and spring-back (right) process.

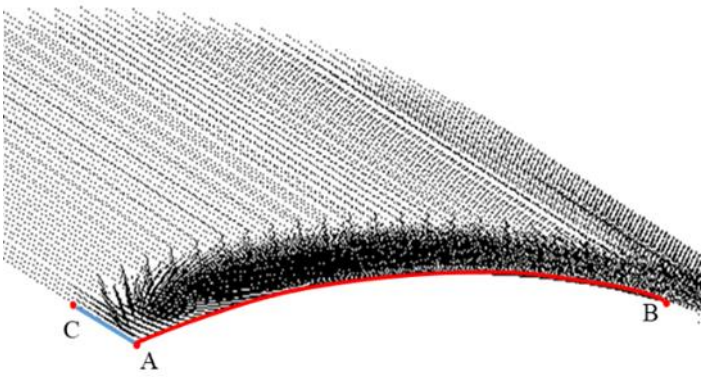

Figure 3.8 A physical model of the dented pipe showing the inner surface of the pipe, where point A is the dent apex, and paths A-B and A-C represent the circumferential and axial directions, respectively.

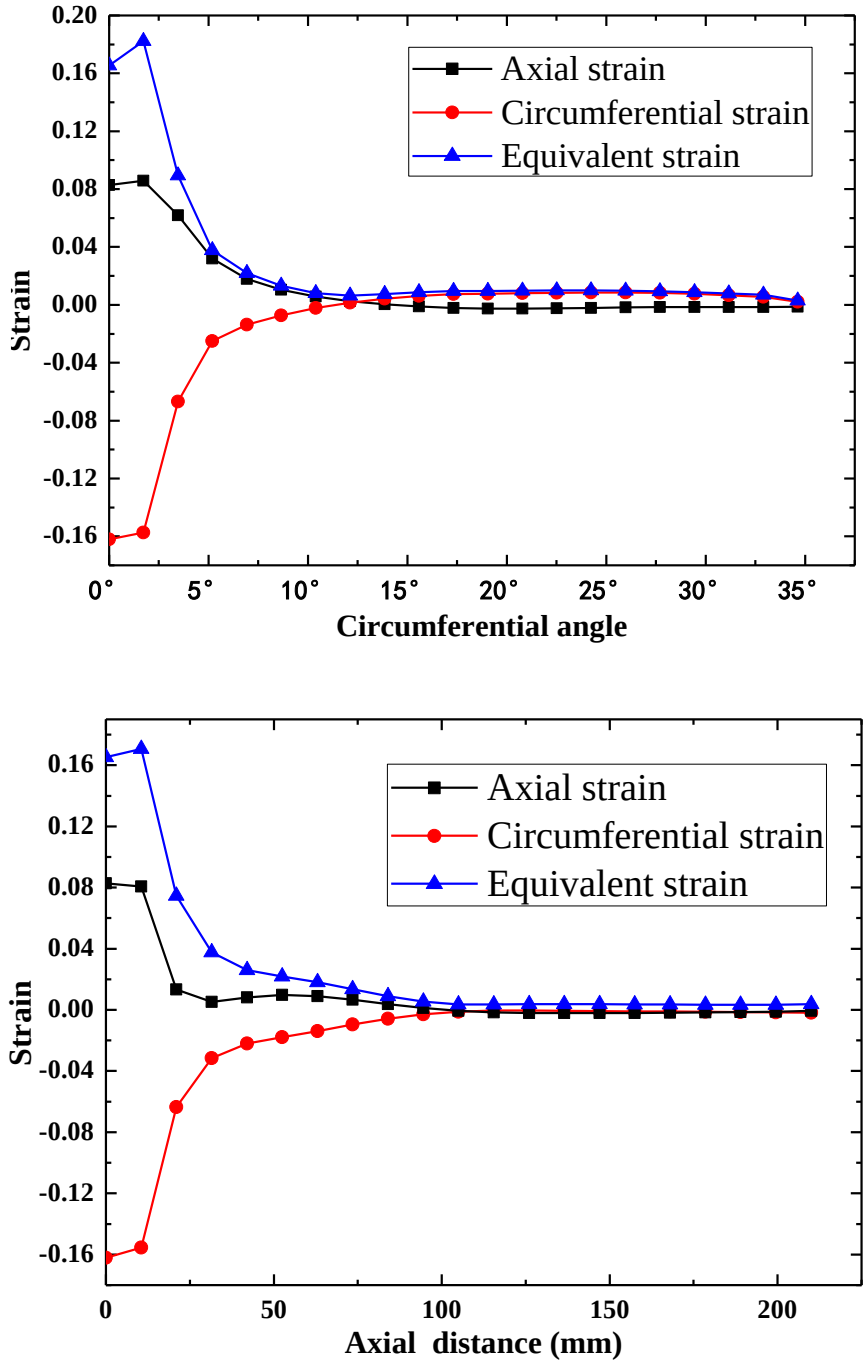

Figure 3.9 Circumferential and axial strains as a function of circumferential angles and axial distance, respectively, after spring-back. The origin point of both figures refers to the dent apex.

3.5 Discussion of the failure criteria of dented pipeline

3.5.1 Strain at dent – A comparison of FE modeling in this work with ASME B31.8

Strain data in different directions of the dent area can be extracted from the analysis results of FE simulation. Also, the strains can be calculated using the method in ASME B31.8 with Eq. (2.1) ~ Eq. (2.5). In this work, the developed FE model can derive the dent profile more accurately. The local strain including the maximum equivalent strain at the dent area can be determined. At the same time, the derived geometrical parameters were also introduced into the strain calculation equations in ASME B31.8 to calculate the maximum equivalent strain as a comparison with the modeling results obtained in this work. It is noted that ANSYS can calculate the displacement and rotation, but not the curvature radius such as R_1 and R_2. Hence, other methods like geometric deformation curve fitting should be performed. The node displacement was extracted from FE modeling and introduced into the fitting curve using MATLAB. The radius of curvature was solved by first-order and second-order differential operations as in Eq. (2.6).

Fig. 3.10 shows the transverse and axial views of the profile of a dented pipe by FE modeling. Details of the circumferential and axial deformations at the dent area with various dent depths are shown in Fig. 3.11, where the horizontal axis refers to the distance to dent center and the vertical axis is the Cartesian coordinate of internal surface of the dented pipe relative to an intact pipe. To obtain the curvature radius, curve fitting was conducted. Previously, the longitudinal length, L, of the dent was not clearly defined. An axial length of 1/2 of dent depth was taken as L [45], as marked in Fig. 3.11 (b). The derived parameters of the dent created with different indenter displacements on the steel pipe after spring-back upon removal of the indenter are listed in Table 3.2. The strains ε_1, ε_2, ε_3, ε_i and ε_o were then calculated using Eqs. (2.1) ~ (2.5), and the calculation results were compared with the modeling results obtained in this work in Table 3.3, where the

subscripts ‘A’ and ‘F’ refer to ASME B31.8 calculation and FE modeling, respectively. It is seen that, based on ASME B31.8, the difference between equivalent strains of the inner and outer surfaces, i.e., ε_{iA} and ε_{oA}, at the dent apex is about 0.05, which is much smaller than the modeling results of about 0.12 - 0.19. Thus, the ASME B31.8 standard cannot distinguish the difference of strains between the internal and external surfaces of the dent. The FE modeling shows that the inner surface of the dent is under a tensile strain, and the outer surface is of a compressive strain. With increased indentation displacement, the location with the maximum equivalent strain becomes deviated from the dent center. Therefore, ASME B31.8 does not give accurate strains, especially for deep dents on pipelines.

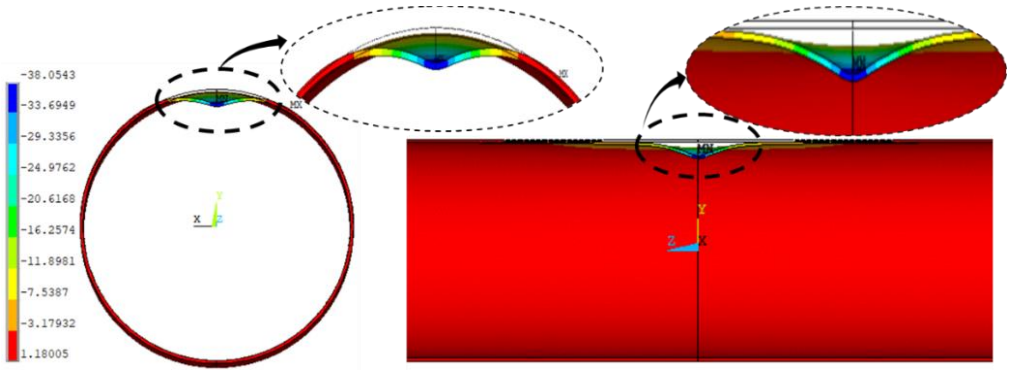

Figure 3.10 Transverse and axial views of the profile of a dented pipe by FE modeling.

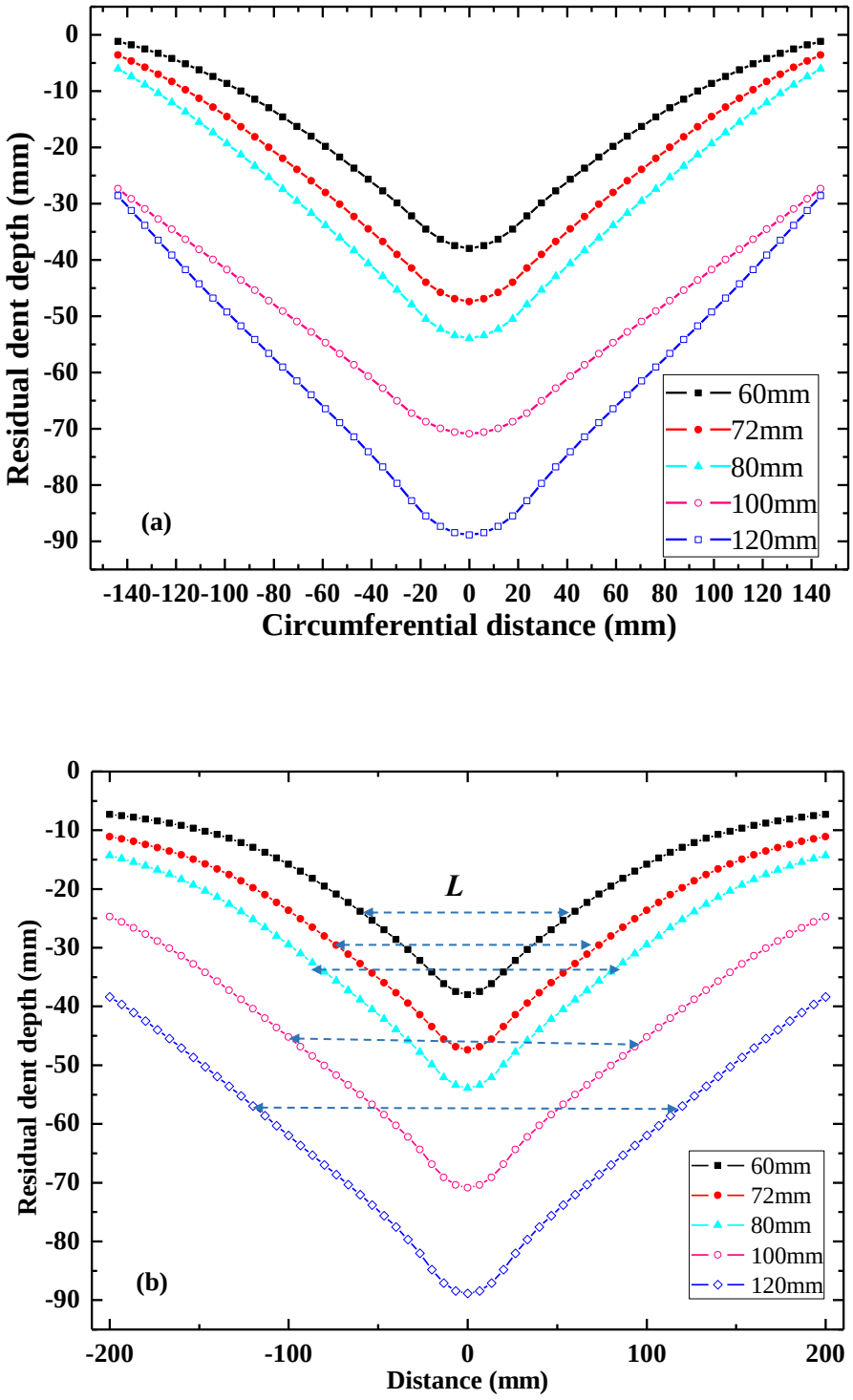

Figure 3.11 Details of the (a) circumferential and (b) axial deformations at the dent area with various dent depths, where the distance of 0 refers to the dent center.

Table 3.2 Derived geometrical parameters of the dent created with different indenter displacements on the steel pipe after spring-back upon removal of the indenter.

Dent depth (mm)	Residual depth (mm)	R_1 (mm)	R_2 (mm)	L (mm)	R_o (mm)	t (mm)
60	37.5	29.0	34.3	165.2	360	8.1
72	46.9	28.2	33.3	198.0	360	8.1
80	53.4	28.8	32.9	224.2	360	8.1
100	70.3	30.0	42.1	274.5	360	8.1
120	88.2	42.5	49.3	343.8	360	8.1

Table 3.3 Comparison of various strains at the dent calculated by ASME B31.8 and obtained by FE modeling in this work.

Dent depth (mm)	ASME B31.8					FE modeling	
	ε_{1A}	ε_{2A}	ε_{3A}	ε_{iA}	ε_{oA}	ε_{iF}	ε_{oF}
60	-0.1285	-0.1179	0.0661	0.1120	0.1634	0.1653	0.0496
72	-0.1323	-0.1312	0.1215	0.1151	0.1670	0.1669	0.0423
80	-0.1300	-0.1304	0.1229	0.1124	0.1656	0.1678	0.0403
100	-0.1237	-0.1236	0.0963	0.1118	0.1471	0.1775	0.0342
120	-0.0842	-0.1168	0.0822	0.0758	0.1246	0.1915	0.0330

3.5.2 Ductile damage assessment criteria for pipeline dent assessment

Another concern of ASME B31.8 in dent assessment is the selection of 6% as the critical strain. Using the stress and strain results from FE modeling, the dent can be assessed by Oyane

criterion and DFDI criterion. Fig. 3.12 shows the damage value (*DFDI* for DFDI criterion and *I* for Oyane criterion) as a function of the indentation displacement at a dent on X52 steel pipe. It is seen that, as the indentation displacement increases, both *DFDI* and *I* values increase, indicating an increased susceptibility to ductile damage. Generally, the ductile damage value calculated by DFDI criterion, i.e., *DFDI* value, is about 10% larger than the value of the Oyane criterion, i.e., *I* value, at specific indenter displacements, indicating that the DFDI criterion is more conservative than Oyane criterion in safety assessment of dented pipelines. Thus, the DFDI criterion gives an extra safety allowance and is more suitable for dent assessment on pipelines.

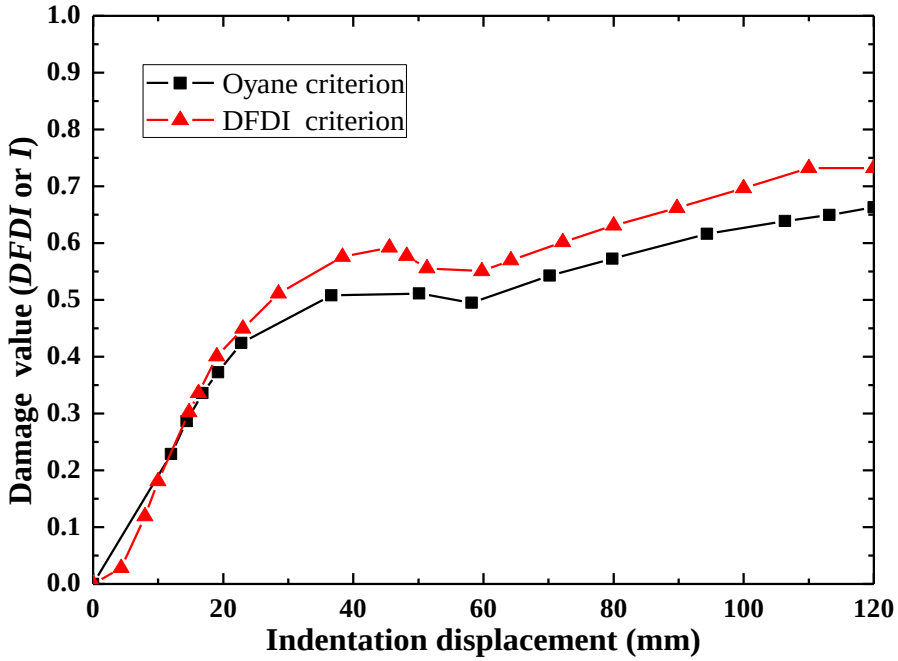

Figure 3.12 Damage value (*DFDI* for DFDI criterion and *I* for Oyane criterion) as a function of the indenter displacement at a dent on X52 steel pipe.

With the modeling results (mainly ε_{eq}, σ_m and σ_{eq}) obtained in this work as input, the *DFDI* values of both internal and external surfaces at a dent were determined based on Eq. (2.15) along

the axial and circumferential paths as marked in Fig. 3.8, where the internal pressure was 8.4 MPa. The results are shown in Fig. 3.13. It is seen that there are larger *DFDI* values on the external surface of the pipe than its internal surface for both axial and circumferential directions. This indicates that the external surface of the dent is weaker than the internal surface and tends to fail first. Moreover, the maximum *DFDI* value is not located at the dent apex. The result is consistent with distribution of the maximum equivalent strain. Generally, a location with the maximum DFDI is the most prone to plastic fracture.

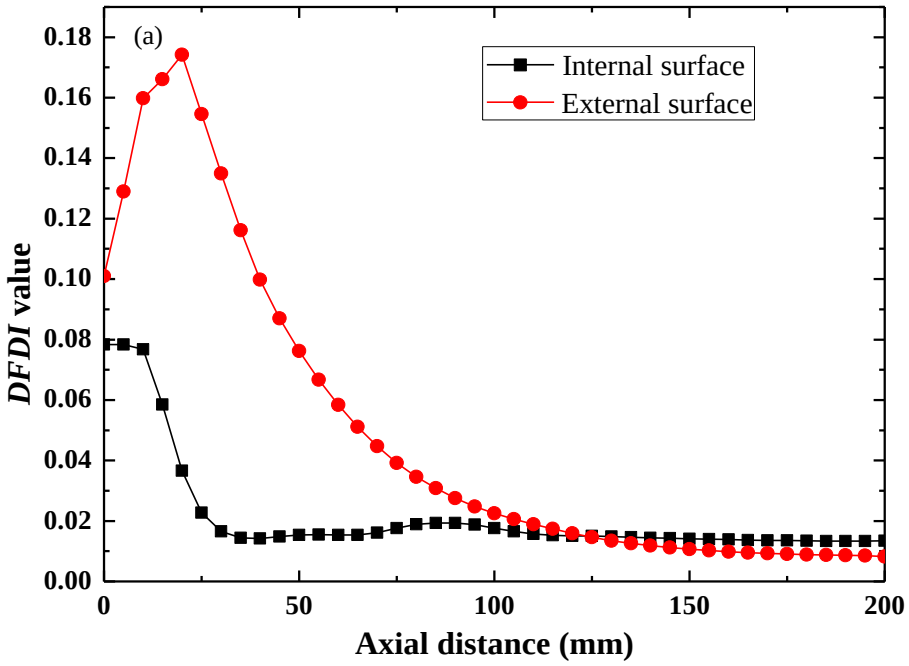

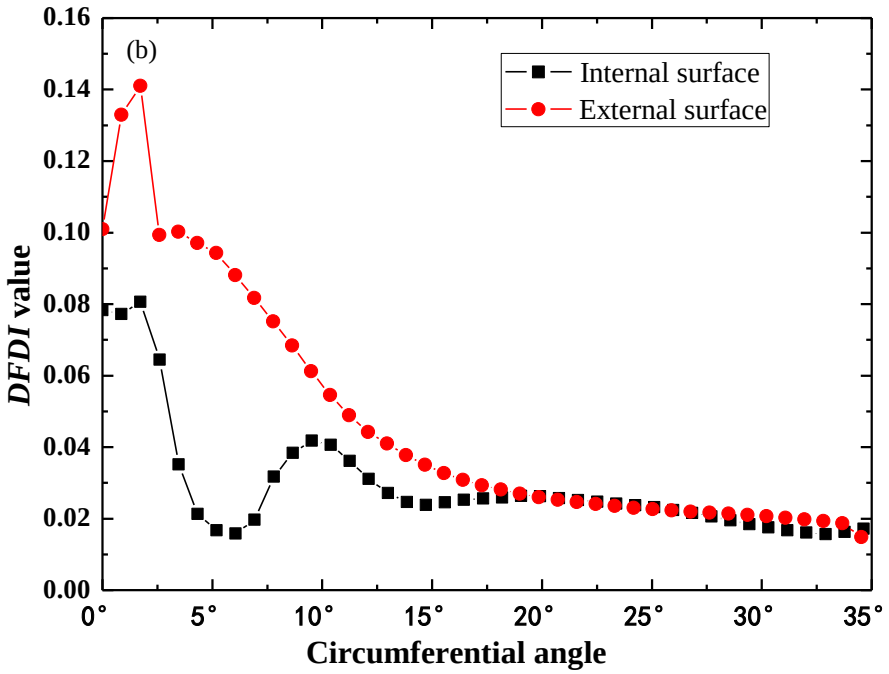

Figure 3.13 *DFDI* values of both internal and external surfaces at a dent along the (a) axial and (b) circumferential paths as marked in Fig. 3.8, where the internal pressure is 8.4 MPa.

Fig. 3.14 shows the maximum DFDI during indentation and spring-back process for dents with various initial indentation displacements on X52 steel pipe. The first stage is indentation, where the horizontal axis is the indenter displacement. The second stage is the spring-back process, where the variable is time step for numerical analysis. The third stage is application of an internal pressure until burst of the pipe, and the horizontal axis is internal pressure. It is seen that the *DFDI* value changes significantly at different stages. With increased indenter displacement, the *DFDI* value increases during indentation, indicating an increased failure risk at deep dents. After spring-back, the DFDI keeps unchanged, and then decreases as the internal pressure increases. At the second and third stages, an increased initial indenter displacement does not always cause a larger *DFDI* value.

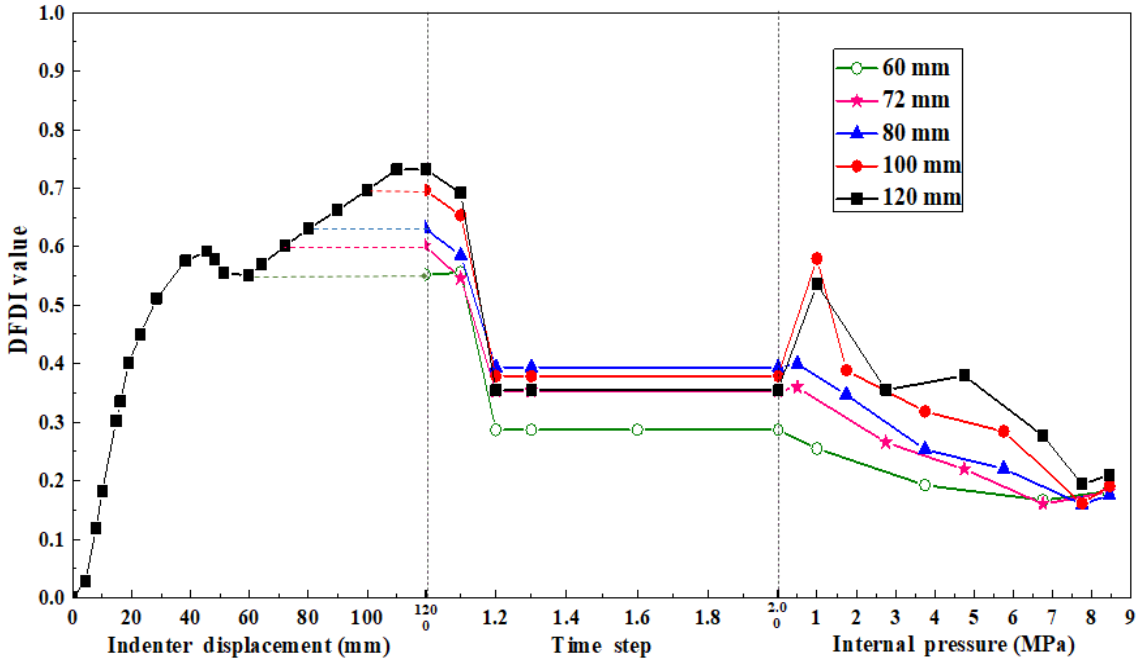

Figure 3.14 Maximum *DFDI* value during indentation and spring-back process at the dents with various initial indentation displacements on X52 steel pipe.

3.6 Development of a new strain-based criterion for dent assessment

The existing strain calculation methods in ASME B31.8 are not sufficiently accurate for dent assessment on pipelines. Ductile damage criteria were validated experimentally that a plastic damage starts when the indicator, e.g., *DFDI* in Eq. (2.15), closes to or exceeds 1. Thus, the ductile damage criterion DFDI combined with improved strain determination by FE modeling developed in this work provides a promising method for pipeline dent assessment.

3.6.1 Present industry practice in dent assessment

Critical input parameters in DFDI criterion include σ_{eq}, σ_m and ε_{eq}. In practice, the ILI tools measure the dent profile to calculate local strain. However, σ_{eq} and σ_m cannot be obtained directly.

To solve the problem, a simplified formula was proposed with assumption of a bi-axial loading, which implied $\sigma_1=\sigma_2\neq0$ and $\sigma_3=0$ [155]. Eq. (2.15) is simplified as:

$$D_e = \frac{\varepsilon_{eq}}{\left(\frac{\varepsilon_d}{1.65}\right)} \tag{3.2}$$

where D_e is the DFDI value under the simplified condition. The effectiveness of the formula was approved by excavation measurements [156]. The internal and external equivalent strains calculated by ASME B31.8 were then used in Eq. (3.2) to calculate D_e and evaluate whether the pipeline fails. Since the DFDI values on the inner and outer surfaces were different, a higher value was chosen for assessment. As discussed, the simplified processing and derivation of the equivalent strain by ASME B31.8 make this method not accurate for dent assessment. Strain calculation method proposed by Lukasiewicz et al. [49] can be used to modify the method in the standard. Compared with strain calculations in ASME B31.8, ε_x and ε_y in Eq. (2.8) can be expressed by ε_1, ε_2 and ε_3:

$$\varepsilon_x = \varepsilon_3 \pm \varepsilon_2 \ , \ \varepsilon_y = \pm\varepsilon_1 \tag{3.3}$$

Then the equivalent strain can be calculated using Eq. (2.7). With the geometric results of dents listed in Table 3.2, the maximum equivalent strain of inner and outer surfaces, ε_{max}, was used to calculate D_e by ASME B31.8 and Lukasiewicz algorithms, and the results are shown in Table 3.4. It is seen that the strain calculated by Eq. (2.7) is larger than the strain calculated by ASME

B31.8, so does the D_e value. Moreover, with an increased indentation depth, both the strain and D_e value decrease. This is attributed to the fact that the location with the maximum equivalent strain is not at the dent apex for deep dents.

Table 3.4 Equivalent strain and D_e value calculated by ASME B31.8 and Lukasiewicz algorithms at the dent apex with various depths.

Dent depth (mm)	ASME B31.8 standard			Lukasiewicz method		
	ε_{iA}	ε_{oA}	D_{eA}	ε_{iL}	ε_{oL}	D_{eL}
60	0.1120	0.1634	0.5265	0.1858	0.3140	1.0120
72	0.1151	0.1670	0.5381	0.1929	0.3215	1.0361
80	0.1124	0.1656	0.5337	0.1932	0.3179	1.0244
100	0.1118	0.1471	0.4741	0.1630	0.2873	0.9258
120	0.0758	0.1246	0.4016	0.1115	0.2298	0.7407

3.6.2 Effect of spring-back behavior on DFDI value

A spring-back process can reduce the equivalent strain at dent apex and the D_e value. Ductile damage is cumulative in nature. For example, the microcracks generating before spring-back do not disappear as the strain decreases. Thus, it is required to determine strain and D_e before spring-back and find a method to correct the difference. Fig. 3.15 (a) shows the relationship between the dent depth after spring-back and the initial displacement, h_o, of the indenter applied on the steel pipe obtained in this work. A linear relationship was observed, which was consistent with the published results [73]. In addition, it was found that the spring-back of the pipe was not affected by the radius of curvature of the indenter. The equivalent strain at the dent apex after spring-back

was also approximately linear with the strain before spring-back, as seen in Fig. 3.15 (b). With the FE modeling, linear equations can be fitted for the results in Fig. 3.15 (a) and 3.15 (b):

$$h_o = 0.7897h - 8.2128 \tag{3.4}$$

$$\varepsilon_{as} = 0.9246\varepsilon_{ini} + 0.0114 \tag{3.5}$$

where h is the dent depth measured after removal of the indenter, ε_{as} is the strain at dent apex after spring-back, and ε_{ini} is the strain before spring-back. Thus, the ductile damage factor before spring-back, D_{e0}, can be modified as:

$$D_{e0} = \frac{\varepsilon_{eq} - A}{\left(\frac{\varepsilon_o}{1.65}\right) \cdot f_1} \tag{3.6}$$

where f_1 is a factor representing the difference of strains after and before spring-back (f_1=0.9246 in this work), and A is a constant, which is 0.0114 as fitted. The strain at the dent apex after removal of the indenter, i.e., ε_{eq} in Eq. (3.6), can be obtained by ILI tools, but f_1, which is important to obtain an accurate ductile damage factor, should be obtained by modeling for specific cases.

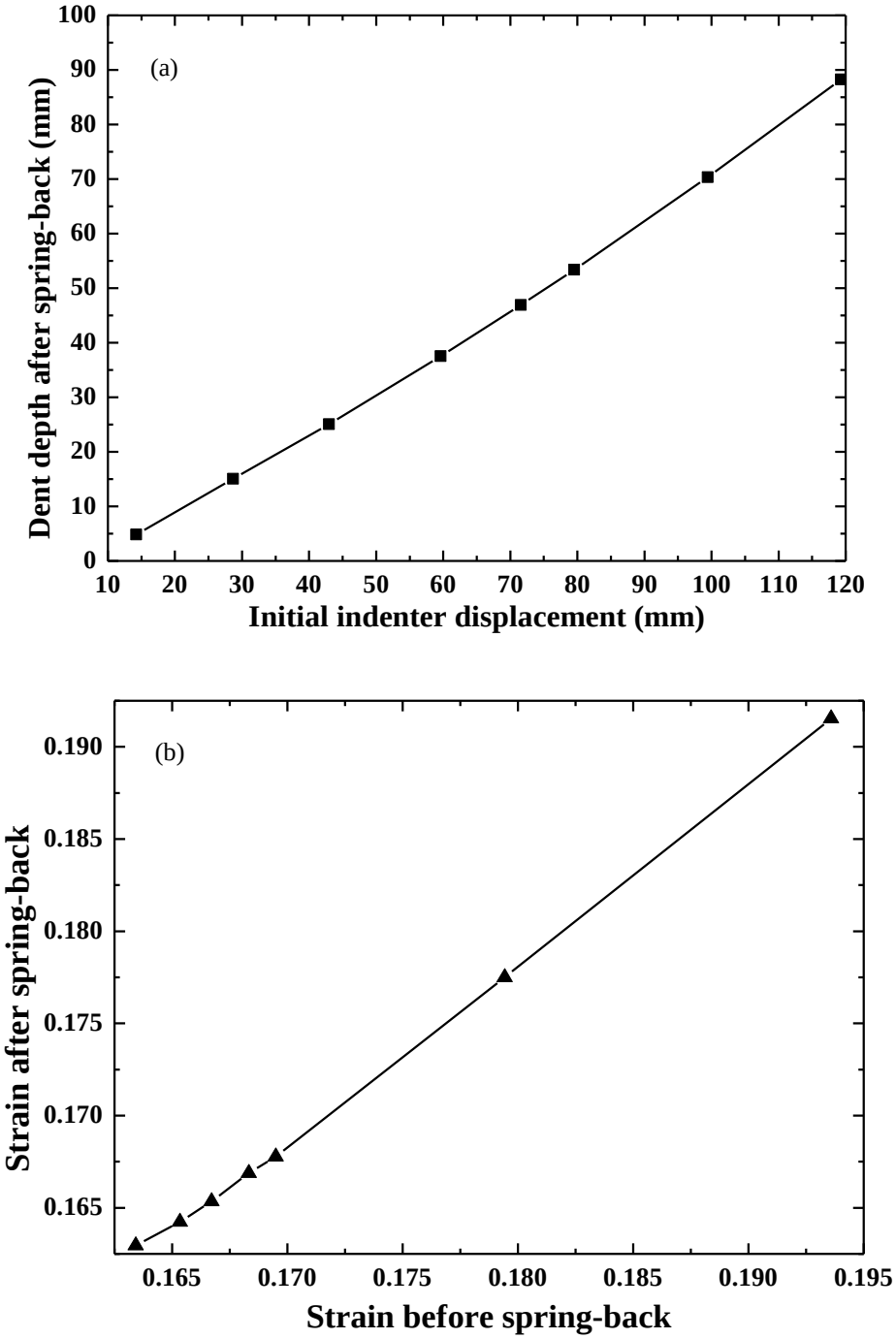

Figure 3.15 (a) Relationship between the dent depth after spring-back and the initial displacement of the indenter obtained in this work, (b) Equivalent strain at the dent apex before and after spring-back.

3.6.3 Determination of the maximum DFDI at dent

This work confirms that, when the indenter displacement is smaller than the 8% of the pipe outer diameter, the maximum *DFDI* is located at the center of the dent. Otherwise, the location with the maximum *DFDI* deviates from the dent center. Moreover, when the spring-back process is considered, the strain distribution becomes more complicated at the dent. To evaluate the ductile damage more accurately, a determination of the *DFDI* value at the dent apex only is not sufficient. The FE modeling can provide the equivalent strain at the dent apex and the maximum equivalent strain at the dent area, and the relationship between them is shown in Fig. 3.16. To simplify the analysis, a linear fitting function is derived to describe the relationship between the equivalent strain at the dent apex and the maximum equivalent strain at the dent area by:

$$\varepsilon_{\max} = 2.4544\varepsilon_{\text{apex}} - 0.2226 \tag{3.7}$$

where $\varepsilon_{\max}$ is the maximum equivalent strain at the dent area, and $\varepsilon_{\text{apex}}$ is equivalent strain at the dent apex. Eq. (3.6) is then modified as:

$$D_{\text{em}} = \begin{cases} \dfrac{\varepsilon_{\text{eq}} - A}{\left(\dfrac{\varepsilon_{\text{o}}}{1.65}\right)\cdot f_1}, & \text{when } h_{\text{o}} \le 0.08\, D_{\text{o}} \\ \dfrac{\varepsilon_{\text{eq}} - A - B\cdot f_1}{\left(\dfrac{\varepsilon_{\text{o}}}{1.65}\right)\cdot f_1 \cdot f_2}, & \text{when } h_{\text{o}} > 0.08\, D_{\text{o}} \end{cases} \tag{3.8}$$

where D_{em} is the maximum ductile damage factor at dent, B is a constant, which is fitted as 0.2226 in this work, f_2 is a factor determined in Eq. (3.7), which is 2.4544 in this work, and D_o is pipe outer diameter. Eq. (3.8) presents the final form of dent assessment method with an improved accuracy for pipeline failure prediction. When h_o is smaller than 8%D_o, D_{em} can be determined from the equivalent strain at the dent apex. However, when h_o exceeds 8%D_o, the maximum equivalent strain at the dent area should be determined by the developed FE model. This work developed a more accurate, quantitative relationship between the equivalent strain at dent apex and the maximum equivalent strain at the dent area. Eq. (3.8) provides a new method for dent assessment, as compared with the industry practice used today, based on the exact geometrical profile of the dent present on pipelines.

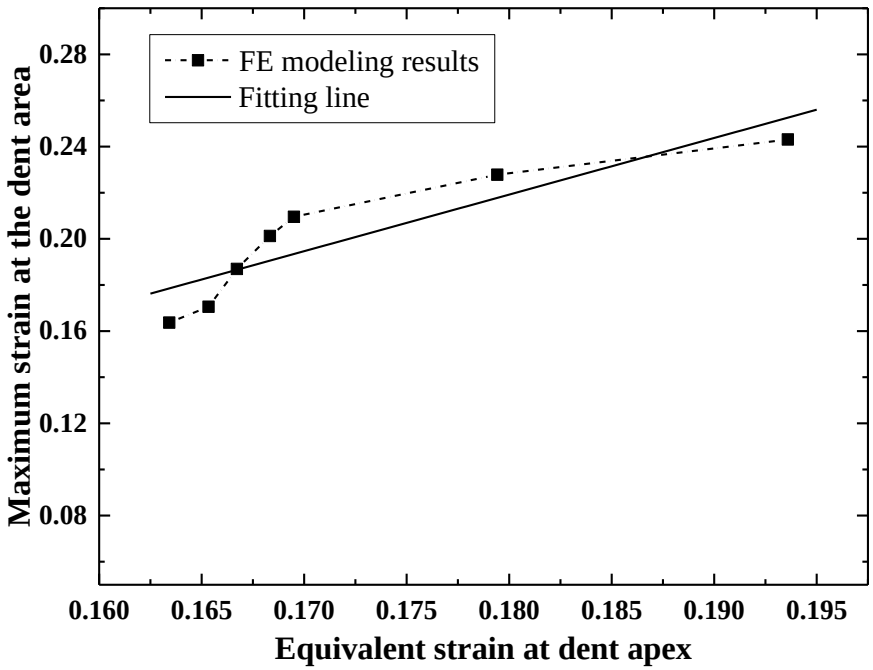

Figure 3.16 Relationship between the equivalent strain at dent apex and the maximum strain at the dent area obtained by FE modeling.

3.7 Conclusions

The FE model developed in this work can simulate the indentation and spring-back process while dents are created on a steel pipe. The strain distribution at the dent can be accurately determined. An internal pressure influences pipe deformation during indentation by reducing the local strain and preventing denting effect. The results in this work are based on modeling of the pipe segment with geometrical parameters included in literature [11], and general conclusions can be obtained from the developed method with different pipe geometrical parameters.

The commonly used ASME B31.8 standard for dent assessment in industry does not give accurate strains, especially for deep dents on pipelines, even using the geometric parameters of the dent derived by the FE model. Moreover, ASME B31.8 cannot distinguish the difference of strains between the internal and external surfaces of the pipe at a dent. Another major limitation of ASME B31.8 is that a strain of 6% is randomly selected as the critical strain for pipeline failure at the dent.

For the two ductile damage-based failure criteria, i.e., DFDI and Oyane criteria, the DFDI criterion is more conservative and gives an extra safety allowance in assessment of dented pipelines. Thus, the DFDI criterion is more suitable for dent assessment on pipelines. With the modeling results such as equivalent strain at a dent obtained by the developed model, the *DFDI* values of internal and external surfaces of the dent are determined. The external surface of the dent is weaker than the internal surface and tends to fail first. The maximum *DFDI* is not located at the dent apex, especially for deep dents, and the result is consistent with the distribution of the maximum equivalent strain.

A new method based on the ductile damage DFDI criterion combined with the improved strain determination by FE model is developed for pipeline dent assessment. The DFDI formula is

modified by considering the influence of spring-back and the difference between the equivalent strain at dent apex and the maximum equivalent strain at the dent area. A new failure assessment criterion is proposed. When the indenter displacement is smaller than 8% of pipe outer diameter, the maximum *DFDI* can be determined from the equivalent strain at the dent apex. However, when the initial displacement exceeds 8% of pipe outer diameter, the maximum equivalent strain at the dent area, which deviates from the dent apex, should be determined by the FE models.

Chapter Four: A new method for assessment of burst pressure capacity of corroded X80 steel pipelines containing a dent[‡]

4.1 Introduction

Increasing energy demands today require the pipelines to operate under high internal pressures [15, 157]. High-strength steels such as X80 steel are increasingly used in gas pipeline transportation [24, 54, 158]. Lots of experimental and numerical research has been carried out assessing the burst pressure of corroded pipelines. For example, Mondal and Dhar [53] developed burst pressure formulas based on FE modeling and experimental testing for determination of burst pressure of corroded pipelines. The formulas are acceptable to industry for pipeline failure prediction. The geometrical parameters of corrosion defects are considered in assessment of the pressure capacity of corroded pipelines [79, 117, 133, 159, 160]. However, these methods and criteria suffer from some limitations. First, validation experiments were mostly performed on low-grade steels such as X52 steel, while high-grade steels such as X80 steel were rarely tested for modeling purposes. Second, according to the M-E interaction theory [24, 161], the plastic strain produced by denting can enhance the corrosion rate. However, the available assessment models do not consider the stress-corrosion interactions. Finally, most investigations to determine the burst pressure were limited to pipelines containing corrosion defects only [162]. For example, a recent work investigated the effect of internal corrosion defect on burst failure of pipelines [163], while other types of defects such as dent and its interaction with corrosion were not considered.

[‡] The work in this chapter has been published as:

Jian Zhao, Yunrong Lv, Y. Frank Cheng, A new method for assessment of burst pressure capacity of corroded X80 steel pipelines containing a dent, *International Journal of Pressure Vessels and Piping*, 199 (2022) 104742. https://doi.org/10.1016/j.ijpvp.2022.104742

The combinations of a dent and metal-loss defects such as scratch and gouge were investigated [44, 73]. It is found that the dent does not affect pressure-bearing capacity of the pipeline containing a gouge or a scratch [12]. Sun et al. [164] investigated the interaction between a corrosion defect and an adjacent dent on an X46 steel pipeline, where the overlapped dent with corrosion defect, which was more commonly observed in practice, was not considered. Moreover, the effect of the dent on further corrosion growth was not included in the existing assessment methods because the models do not consider the M-E interaction on pipelines. Generally, both external and internal corrosion of pipeline at a dented area are both affected due to a local stress concentration and the resulting M-E interaction. While this work focuses on the interaction of a dent with external corrosion, for the inner surface, the steel is mainly under a tensile stress [163], which strongly enhances the corrosion rate.

The novelty of this work is to develop a new FE-based method to perform pressure capacity assessment on corroded pipelines containing a dent, where the mutual interaction between the corrosion defect and the dent, as well as its effect on corrosion growth with time, were defined. A three-dimensional (3-D) FE model was developed to simulate the processes of denting and burst failure of a corroded high-strength X80 steel gas pipeline. Parametric effects, including corrosion depth, dent depth and corrosion length, on local stress distribution and burst pressure of the pipe were determined. The stress-enhanced corrosion growth due to the dent-corrosion defect interaction was quantitatively evaluated. A burst assessment program for corroded steel pipelines containing a dent was proposed for integrity management of the pipelines.

4.2 Algorithms for finite element analysis

4.2.1 Modeling for pipeline steels and their mechanical properties

The material used in this work is an X80 pipeline steel. To validate modeling results obtained from this work, experimental measurements in the literature were used. Moreover, an X65 steel was also selected for modeling to provide additional confirmation in terms of the modeling reliability. As suggested by API 579-1/ASME FFS-1 2016, the R–O model was used for both X65 and X80 steels in this work.

For X65 steel, the R–O model is described as [165]:

$$\varepsilon = \frac{\sigma}{E} + \alpha \left(\frac{\sigma}{\sigma_{\mathrm{y}}} \right)^{\beta} \left(\frac{\sigma}{E} \right) \tag{4.1}$$

and for X80 steel,

$$\varepsilon = \frac{\sigma}{E} + 0.079 \left(\frac{\sigma}{\sigma_{\mathrm{U}}} \right)^{12.64} \tag{4.2}$$

Mechanical properties of X65 and X80 steels are listed in Table 4.1. The R–O relationship curves of X65 and X80 steels are shown in Fig. 4.1. For modeling of the denting process, a rigid material model was used for the indenter. The Poisson ratio was 0.3 for all materials used in the work.

Table 4.1 Mechanical properties of X65 and X80 steels [73, 166, 167].

Grades	E / GPa	σ_{y} / MPa	σ_{U} / MPa	α	β
X65	206.7	449	531	3.686	10.64
X80	200	601	684	-	-

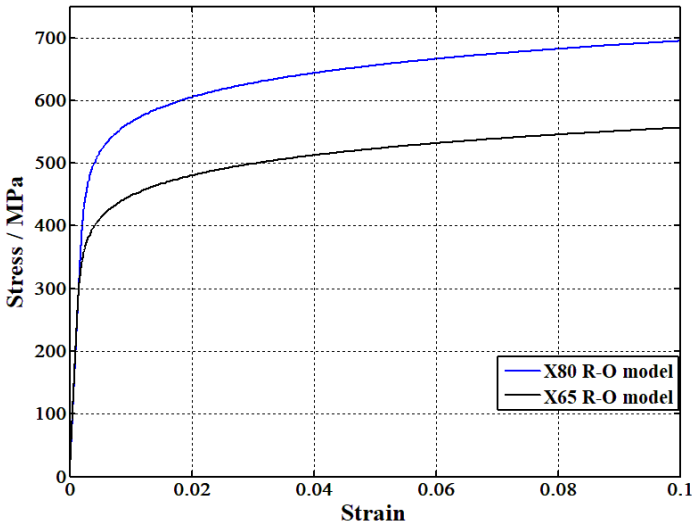

Figure 4.1 Stress-strain curves of the R–O model used for X65 and X80 pipeline steels.

4.2.2 Modeling for defects on steel pipes

Both corrosion and dent defects were considered in FE modeling to investigate the combined effect on burst failure of the X80 steel pipe. An FE model for the steel pipe containing corrosion defect only was also developed to validate the model with existing testing results included in literature. Both pressurizing the steel pipe to burst and denting processes are elastic-plastic deformations and nonlinear processes. An 8-nodes 3-D element Solid185 was used for FE modeling in the software ANSYS for both the pipe segment and the indenter. A dent was generated on a corrosion defect present on the pipe segment. Due to the symmetrical nature, a quarterly model was used to save calculational time. The schematic diagram of the quarterly portion of a steel pipe containing a corrosion defect combined with a dent are shown in Fig. 4.2, where D_o, L_1 and t are pipe outer diameter, length of the pipe segment and pipe wall thickness, respectively, d_c, l_c and w are depth, longitudinal length and circumferential width of the corrosion defect,

respectively, *h* is depth of the dent center, which is also the center of the corrosion defect, and *x*, *y* and *z* are circumferential, radial and axial directions, respectively.

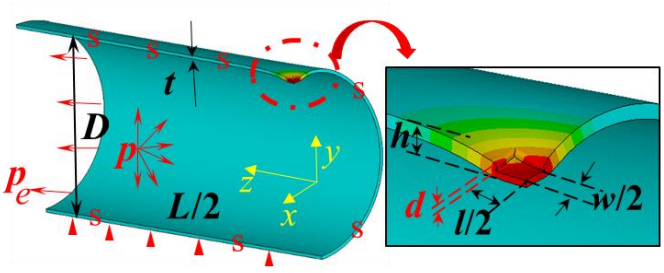

Figure 4.2 Schematic diagram of a quarterly portion of a steel pipe containing a corrosion defect combined with a dent.

The FE model included two parts where different element sizes were applied. The stress-strain condition of the defect area was the target, where fine elements were assigned with a size of 2 mm. Relatively coarse elements with a size of 10 mm were assigned on the remaining part of the pipe segment. The element size of the indenter was same as the size of the defect area. The rigid properties were applied for the indenter, and the element type for the indenter was also Solid185. It is realized that the rigid surface element is also effective for modeling. However, application of surface elements in a solid model is much complicated and is not used in the work. Meshing of the FE model is shown in Fig. 4.3, and similar grid size settings are also used in Ref. [168]. The grid sensitivity test confirmed that the selected element sizes are proper for FE analysis. When considering the indentation process on the corroded pipe, the contact/target elements were established in the contact area between the indenter and the pipe.

Geometrical parameters of the model were consistent with experimental settings in literature [166, 169]. The outer diameter (D_o) of X65 steel pipe was 762 mm and the pipe wall thickness (t)

was 17.5 mm. The depth (d_c) of the corrosion defect was 8.75 mm, and its lengths (l_c) were 100 mm and 200 mm, respectively. For X80 steel pipe, the outer diameters included 459 mm and 457 mm, with pipe wall thicknesses of 8 mm and 8.1 mm. The corrosion defect was 40 mm and 39.6 mm in length, and 3.75 mm and 5.4 mm in depth, respectively. The edges of the corrosion defect were rounded into a radius of 1.5 mm to simulate actual corrosion morphology.

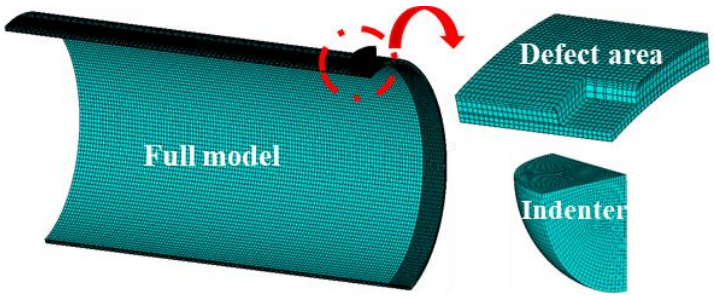

Figure 4.3 Element meshing of the FE model used for different parts of the pipe segment.

It is noted that the modeling results can be affected by the length (L_1) of the pipe segment. For FE modeling, if L_1 is too small, the boundary conditions applied on both ends of the pipe will influence the stress and strain distributions at the defect area. To eliminate this effect, the minimum length of the modeled pipe segment, L_{min}, should meet the requirement [170]:

$$L_{min} = \frac{l_c}{2} + \frac{d_c}{t}\sqrt{D_o \cdot t \cdot l_c} \tag{4.3}$$

It is seen that L_{min} is determined by geometrical parameters of the pipe and of the corrosion defect. With inputs of relevant parameters used in this work, the pipe segment lengths of 2000 mm and

4000 mm were selected for X65 and X80 steel pipes, respectively. Based on calculations in this work, the X65 steel pipe requires a minimum length of 627.39 mm (for a corrosion length of 100 mm) and 916.55 mm (for a corrosion length of 200 mm). The selected pipe segment length of 2000 mm meets the requirement of Eq. (4.3). In addition, as analyzed by FE, this pipe segment is sufficiently long that the pipe segment length effect can be eliminated. It is suggested [108] that the circumferential width (w) of corrosion defect does not affect the burst pressure of corroded pipelines. As a result, w was kept constant with the same value as the value in literature. The dent was created on the corrosion defect by an indenter shaped of a sphere with a diameter 80 mm. The distance of downward movement of the indenter influences the dent depth (h).

To approximate with the experimental settings of burst tests in literature, the boundary conditions of the FE model were consistent with the tests. As shown in Fig. 4.2, the symmetric surface of the model was set as symmetric boundary conditions, which are marked as "s" in the figure. The displacement in y direction of the bottom line was restrained to avoid rigid body motion. The internal pressure, p, was applied on the inner surface of the pipe, and sufficient load steps were set to analyze the pipe performance under different internal pressures. Downward and upward displacement loads were applied on the indenter to create a dent on the pipe. During the burst test, the pipe was filled with water and a hydrostatic pressure continually increased until the pipe failed. End caps were installed at both ends of the pipe segment. The effect of end caps should be approximated in the model, and thus, an equivalent pressure, p_e, was applied on the end surface of the model. An axial tension, p_e, can be calculated by Refs. [2, 5]:

$$p_e = p \cdot \frac{\left(D_o - 2t\right)^2}{D_o^{\,2} - \left(D_o - 2t\right)^2} \tag{4.4}$$

A widely accepted failure criterion in FE modeling is selected in this work [1]:

$$\sigma_{\text{Mises}} = \frac{1}{\sqrt{2}}\sqrt{(\sigma_1-\sigma_2)^2+(\sigma_2-\sigma_3)^2+(\sigma_3-\sigma_1)^2} > \sigma_{\text{U}} \tag{4.5}$$

The von-Mises equivalent stress, σ_{Mises}, is compared with the ultimate tensile strength, σ_{U}, to determine pipe failure.

4.2.3 FE modeling procedure

The Newton-Raphson method is used for nonlinear analysis. The processes for modeling a corroded pipe in the absence and presence of a dent are different. For burst of the corroded pipe without a dent, the FE analysis was conducted by: (1) The FE model was established with specific geometric parameters of the pipe and of the corrosion defect. The R–O material models for X65 and X80 steels were applied on the pipe. (2) Symmetric boundary conditions and internal pressure were applied on the model. (3) Nonlinear large deformation and load steps were set, and the pressure applied on the pipe was increased until failure occurred. The burst pressure was calculated.

For corroded X80 steel pipe containing a dent, the indentation process was simulated to obtain a good approximation to the reality. Three steps were followed: (1) The FE models of the corroded pipe and the indenter were developed with proper input parameters. The contact/target elements were used in the contacting surface between the indenter and the corrosion defect. (2) Symmetric boundary conditions and motion constraint in *y* direction were applied on the pipe. Pre-determined downward displacement loads were applied on the indenter and compression happened. At this stage, the internal pressure *p* was set as 0. (3) The indenter was removed upward and a spring-back

at the dent area was observed. An internal pressure p was then applied on the inner surface of the pipe until a non-convergence occurred. The burst pressure of the pipe was determined.

4.3 Results

4.3.1 Validation of FE modeling results

To validate the FE modeling results, burst testing results obtained on corroded pipelines in open publications were used as references [166, 169]. Burst pressures of X65 and X80 steel pipes measured in literature and the burst pressures modeled by FE analysis in this work are shown in Table 4.2, where both X65 and X80 steel pipes are used to show the applicability of the FE model on both low- and high-grades of pipe steels. Moreover, the geometric parameters of the FE model were set as identical to those used in tests in literature. It is seen that the errors between the test measurements and the modeling results are small, with a maximum value of 3% only. It is thus thought that the FE model is acceptable for pipeline burst analysis.

Table 4.2 Comparison and validation of burst pressures of X65 and X80 steel pipes measured in experiments in Ref. [166, 169] and modeled by FE analysis in this work.

Steels	Pipeline geometry, mm			Corrosion size, mm			Burst pressure, MPa		
	Diameter (D_o)	Thickness (t)	Length (L_1)	Length (l_c)	Depth (d_c)	Width (w)	Test p_{test}	FE p_{FE}	Difference %
X65	762	17.5	2000	100	8.75	260	24.68	24.94	1.0
X65	762	17.5	2000	200	8.75	260	22.48	22.105	1.7
X80	459	8	4000	40	3.75	32	24.2	25.378	4.6
X80	457	8.1	4000	39.6	5.4	32	22.7	23.453	3.2

4.3.2 Burst pressures of X80 steel pipe containing corrosion defect and dent

The burst pressure of X80 steel pipe was analyzed with various corrosion depths (d_c) and dent depths (h), while other parameters were kept constant, i.e., D_o=457 mm, t=8.1 mm, L_1=4000 mm, and w=32 mm. Fig. 4.4 shows the burst pressure results obtained by FE modeling. The dent depths were selected to reflect a continuous change from a shallow dent to a deep dent. The corrosion depth of 2–6 mm was selected to be representative of general corrosion defect present on pipelines. When a corrosion defect is too shallow such as less than 2 mm, it does not generate sufficient adverse effect on pipelines. If the corrosion defect is too deep, the operators should repair the defect for safety reason. A gradual increment in corrosion defect depth was to investigate the effect of corrosion defect on pipeline burst failure. It is seen that, at specific dent depths, the burst pressure of the pipe decreases as the corrosion depth increases. However, the dent depth does not affect burst pressure of the corroded steel pipe at individual corrosion depths. Particularly, when the dent does not exist (i.e., a dent depth of zero), the burst pressure is greater than the dent is present on the pipe. The results are same as those obtained on corroded low-grade steel pipes containing metal-loss defects [171, 172], and the conclusions are thus convincing. Generally, denting is a large elastic-plastic deformation process. The dent area is strengthened by a strain hardening mechanism [12]. Dent is not a metal-loss, and there is a limited effect on pressure-bearing capacity of the pipelines. As a comparison, corrosion causes a local thinning of pipe wall. As a result, the pressure capacity of the pipe decreases at the local area.

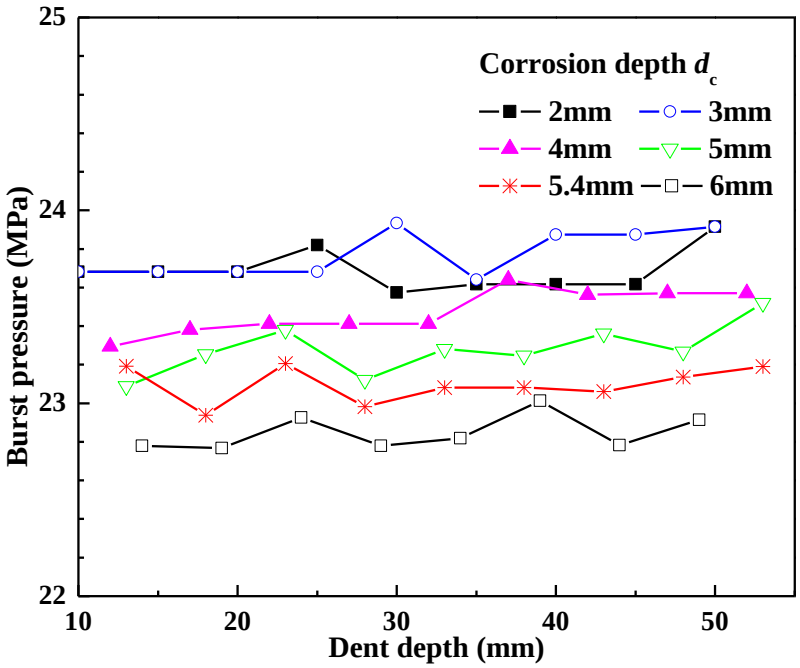

Figure 4.4 Burst pressures of X80 steel pipe containing corrosion defect with various depths and a dent with varied depths obtained by FE modeling.

4.3.3 Effects of corrosion defect and dent on stress distribution on the pipe

Fig. 4.5 shows an example of the von Mises equivalent stress distribution at a corrosion defect with a depth of 5.4 mm (i.e., 0.67t) on an X80 steel pipe, where there is no dent present, operating at a pressure p=10 MPa [158]. The stress level at the corrosion area is relatively low, except the corner edge where a stress concentration is developed. At the bottom of the corrosion defect, the greatest equivalent stress is 460 MPa, indicating that the defect is in elastic deformation. Even at the corner edge, the local stress is up to 550 MPa, which is close to yielding but still at an elastic deformation, while the yielding strength of X80 steel is 601 MPa.

When a dent is generated on the corrosion area, the local stress distribution is changed. A spring-back process occurs after the indenter is removed. To distinguish different stages during denting, various initial corrosion depths (d_c) and the maximum initial dent depths (h_0), i.e., the dent

depth prior to the spring-back, were selected. The instant dent depth (h) refers to the dent depth after the spring-back occurs, which is resulted from removal of the indenter and application of an internal pressure on the pipe. Figs. 4.6 and 4.7 show distributions of von Mises equivalent stress of a corroded X80 steel pipe (operating pressure: 10 MPa) after spring-back of indentation with different values of h_0 at the initial corrosion depths of 5.4 mm and 2.0 mm, respectively. The two corrosion defect depths were selected because they were located at both ends of the investigated depth range. Generally, at least 3 cycles of internal pressure, i.e., equivalent to 72% of specified minimum yield strength (SMYS) of the pipe steel, were applied to produce rebounding of a dented pipe to consider a residual dent depth at the end of the process, which was assumed not affected by further internal pressure to be applied [173]. Internal pressure acts to reduce the dent depth, and this reduction is a nonlinear deformation process. A better comparison between different initial dent depths (h_0) could be attained considering the rebounding process. It is seen that, at the corrosion depth of 5.4 mm, the stress at the corrosion defect increases with increased h_0. For example, the equivalent stress at the center of the corrosion defect increases from 437 MPa to 684 MPa when the initial dent depth h_0 increases from 15 mm to 40 mm. When the initial dent depth h_0 is more than 30 mm (i.e., $0.066D_o$), the bottom of the corrosion defect is in plastic deformation, although both the longitudinal and circumferential edges of the corrosion defect are still in the elastic stage. However, at a small corrosion depth such as 2.0 mm, the stress at the bottom of the corrosion defect decreases with the increasing h_0. As seen in Fig. 4.7, the equivalent stress at the center of the corrosion defect decreases from 680.6 MPa to 463.8 MPa as the dent depth increases from 15 mm to 40 mm. It is thus seen that the mutual interaction of corrosion defect and dent depends on the depth of the corrosion defect. At a deep corrosion defect (e.g., 5.4 mm in depth), the stress level at the corrosion defect increases with increased initial dent depth. However, if a

dent is generated at a shallow corrosion defect (e.g., 2.0 mm in depth), the local stress decreases as the initial dent depth increases. When the corrosion defect is relatively deep, a tensile stress exists at the defect bottom and increases with increased dent depth. The local stress further increased under the effect of internal pressure. For shallow corrosion defects, with the effect of spring-back, a compressive stress at the corrosion defect bottom gradually replaces the tensile stress along with the increase in dent depth. As a result, the tensile stress at the corrosion defect bottom decreases as the dent depth increases. Furthermore, shallower corrosion defects tend to present a higher local stiffness. The dent depths after spring-back (h) are expected to be lower when compared with deeper corrosion defects with the same value of h_0. Similarly, deeper corrosion defects have a lower local stiffness and, for the same initial indentation, have higher dent depths after spring-back. Higher stresses are thus expected to be found in deeper corrosion defects.

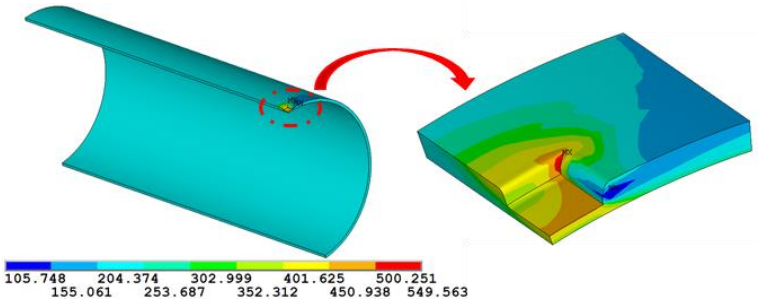

Figure 4.5 An example of the von-Mises equivalent stress distribution at a corrosion defect with a depth of 5.4 mm (i.e., 0.67*t*) on an X80 steel pipe, where there is no dent present, operating at a pressure *p*=10 MPa [158].

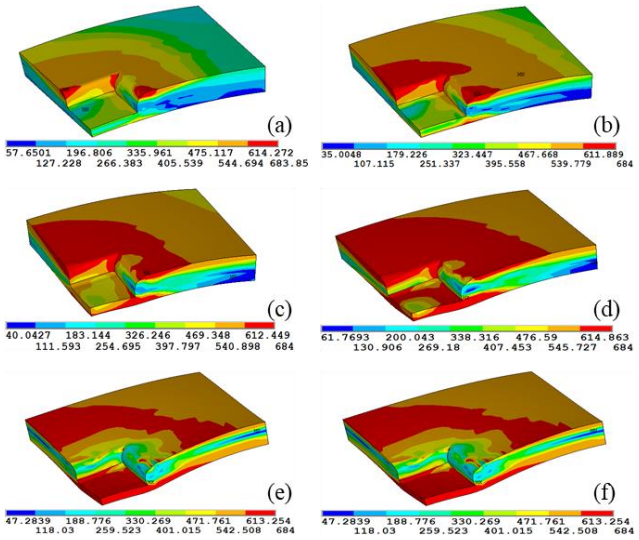

Figure 4.6 von Mises stress of a corroded X80 steel pipe (operating pressure: 10 MPa) after spring-back with different values of h_0 at an initial corrosion depth of 5.4 mm (a) h_0=15 mm, (b) h_0=20 mm, (c) h_0=25 mm, (d) h_0=30 mm, (e) h_0=35 mm, (f) h_0=40 mm.

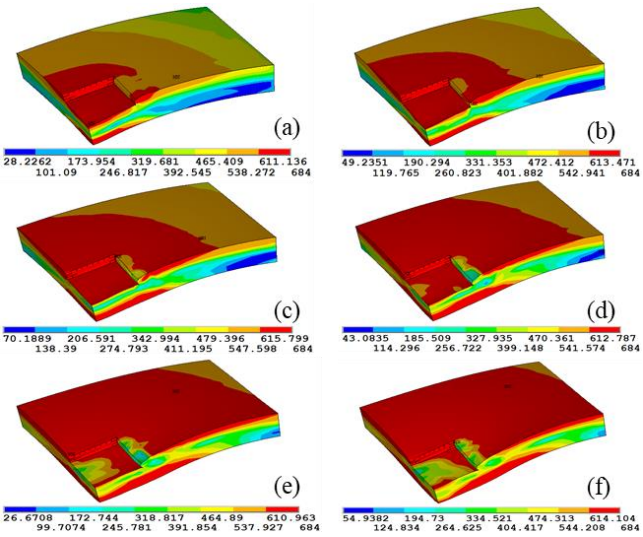

Figure 4.7 von Mises stress of a corroded X80 steel pipe (operating pressure: 10 MPa) after spring-back with different values of h_0 at an initial corrosion depth of 2.0 mm (a) h_0=15 mm, (b) h_0=20 mm, (c) h_0=25 mm, (d) h_0=30 mm, (e) h_0=35 mm, (f) h_0=40 mm.

4.3.4 Effect of dent on corrosion defect growth on pipeline

Corrosion is electrochemical in nature. The corrosion rate can be expressed as anodic dissolution rate of steels. The presence of stress can enhance corrosion reaction, and the enhancement factor, k_σ, is defined as [111]:

$$k_\sigma = \frac{R_{ct}^{\sigma=0}}{R_{ct}^{\sigma}} \tag{4.6}$$

where $R_{ct}^{\sigma=0}$ and R_{ct}^{σ} are charge-transfer resistance, which is inversely proportional to corrosion rate, in the absence and presence of stress (σ), respectively. By measuring the values of $R_{ct}^{\sigma=0}$ and R_{ct}^{σ} of pipe steel in a corrosive environment, the stress-enhanced corrosion can be quantitatively determined. Xue and Cheng [112] made electrochemical measurements on X80 steel under various applied stresses in a bicarbonate solution. It was found that k_σ is approximately 1.8 when the stress is elastic, representing the stress-enhanced corrosion factor. When the stress is in plastic stage, the corrosion enhancement becomes more apparent. The specific value of the factor depends on the stress level. Considering conservatism in engineering assessment, a factor 2.25 is used in this work.

There are some models to simulate corrosion growth, such as the single value corrosion growth rate model, linear growth model, power-law model, etc. [174]. The power-law corrosion rate model, as showed below, is widely accepted, and used in pipeline corrosion growth [175]:

$$a_0 = \lambda\zeta\left(T_c - Y_0\right)^{\zeta-1} \tag{4.7}$$

where a_0 is corrosion rate in the absence of the stress enhancement effect that varies over time T_c, Y_0 is the time that corrosion initiates, λ and ζ are proportionality and exponent constants, respectively. As verified previously [175, 176], constants λ and ζ are determined by Y_0, pH, soil chemistry, pipeline coatings, etc. To make the modeling corrosion growth rate results comparable with published work, the values of the parameters are selected: λ=0.164, ζ=0.780 and Y_0=2.88, which are identical to those in the work [176]. It is believed that variations in the parameters will change the corrosion growth model, and thus, provide different prediction results. In this work, the commonly used power model is used. In the further work, the authors will explore and validate the reliability of other corrosion growth models. The depth of the corrosion defect $d_c(T_c)$, (in the absence of stress enhancement effect) can be determined by integrating the corrosion rate a_0 over time T_c:

$$d_c(T_c) = d_0 + \lambda\left(T_c - Y_0\right)^{\zeta} \tag{4.8}$$

where d_0 is initial corrosion depth. When a stress is applied, the corrosion growth rate a and corrosion depth $d_c(T_c)$ are calculated as

$$a = k_\sigma a_0 = k_\sigma \lambda\zeta\left(T_c - Y_0\right)^{\zeta-1} \tag{4.9}$$

$$d_c(T_c) = d_0 + k_\sigma \lambda\left(T_c - Y_0\right)^{\zeta} \tag{4.10}$$

According to Fig. 4.6, for a corroded pipe containing a 5.4 mm deep corrosion defect and a dent with an initial depth more than 30 mm (i.e., h_0>0.066D_o), the stress concentration is usually

located on the bottom of the corrosion defect, which is also the site bearing with the plastic stress with the assigned k_σ=2.25. The corrosion growth rates of the defect bottom and the sides are determined as $k_\sigma a_0$ and a_0, respectively. For the circumferential edge of a corrosion defect, the stress is relatively small compared with the longitudinal edge and the bottom of the defect. In addition, as analyzed, the effect of the defect width on the burst pressure is negligible. Thus, the corrosion rate is fixed as a_0 for simplification purpose. As a result, the ratio between the length and depth (i.e., l_c/d_c) of the corrosion defect experiences changes during corrosion process. Similar analyses are also conducted on corrosion defects with different initial depths, and the results of corrosion growth rate are listed in Table 4.3, where the mutual interaction between corrosion defect and dent on further corrosion growth at the defect associated with specific stress levels is quantitatively determined.

Table 4.3 Calculated corrosion growth rates of X80 steel pipe containing a corrosion defect with various initial depths and a dent with various initial depths.

Initial corrosion depth (d_0)	Initial dent depth (h_0, mm)	Corrosion growth rate a (mm·y^{-1})		
		Defect bottom	Longitudinal site	Circumferential site
$d_0 \leq 0.67t$	$h_0 \leq 30$ ($0.066D_o$)	$2.25a_0$	$2.25a_0$	a_0
	$h_0 > 30$	a_0	$2.25a_0$	a_0
$d_0 > 0.67t$	$h_0 \leq 30$ ($0.066D_o$)	a_0	a_0	a_0
	$h_0 > 30$	$2.25a_0$	a_0	a_0

Note: a_0 is corrosion growth rate of X80 steel in near-neutral pH solutions without considering the stress enhancement effect.

The pressure capacity of corroded pipelines assessed in ASME B31G is determined by corrosion length l_c and depth d_c. According to the power-law corrosion rate model in Eq. (4.7), the time dependence of the longitudinal length $l_c(T_c)$ of the corrosion defect can be expressed as:

$$l_c(T_c) = l_{c0} + k_\sigma \lambda \left(T_c - Y_0\right)^\zeta \tag{4.11}$$

where l_{c0} is initial longitudinal length of corrosion defect. In this work, l_{c0}=39.6 mm. The results of l_c/d_c vs. time obtained by FE modeling with different initial corrosion defect depths are shown in Fig. 4.8. The initial corrosion depths of 2.0 mm and 5.4 mm were selected to reflect two typical corrosion scenarios. When the corrosion defect is deeper (such as 5.4 mm in initial depth), the deceasing rate of l_c/d_c with time is small, meaning that the depth growth is a bit faster than the length growth. As the dent depth increases, the ratio reduces. However, for a shallow corrosion defect such as 2.0 mm in initial depth, the deceasing rate of l_c/d_c with time is much greater, meaning that the depth growth is accelerated with time. However, as the dent depth increases, the ratio increases. The dependence of the corrosion growth rate on depths of corrosion defect and dent are well consistent with the stress modeling results in Figs. 4.6 and 4.7.

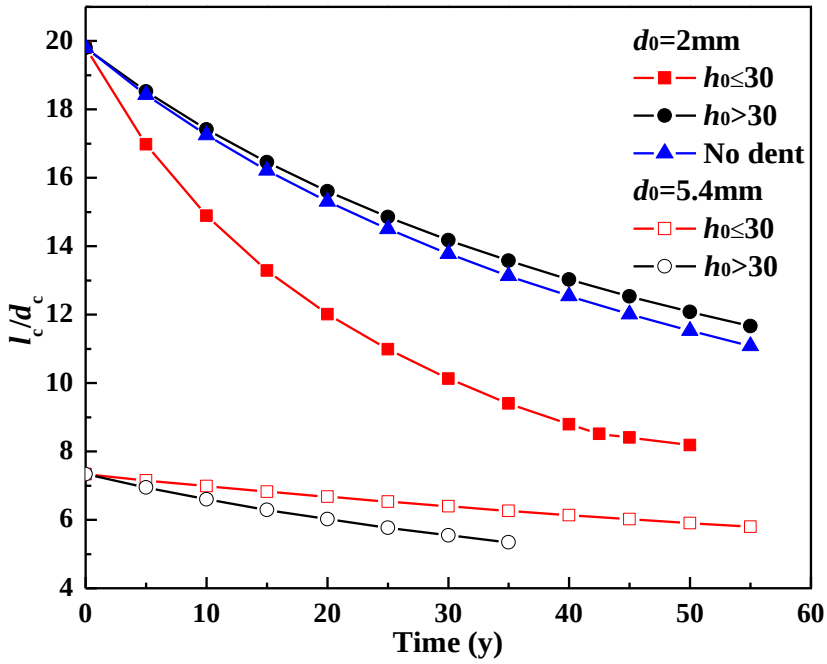

Figure 4.8 The ratio of longitudinal length of the corrosion defect to its depth, i.e., l_c/d_c, vs. time obtained by FE modeling with different initial corrosion defect depths.

4.4 Failure assessment of pipelines containing both corrosion defect and dent

4.4.1 Comparison of the developed FE model with existing assessment methods for corroded pipelines

Presently, the pressure capacity of natural gas pipelines containing corrosion defects is assessed by standards such as ASME B31G and DNV RP F101. The common characteristic of these methods is that the effect of corrosion defect is treated as a damage factor. According to the modified ASME B31G, the failure pressure, P_{ASME} (MPa), of a corroded pipelines is calculated by:

$$P_{\text{ASME}} = \frac{2 \cdot t}{D_o} \cdot S_F = \frac{2 \cdot t}{D_o} \cdot S_{\text{flow}} \cdot \left[\frac{1 - 0.85(d_c/t)}{1 - 0.85(d_c/t)/M} \right] \tag{4.12}$$

where M is Folias factor, and S_{flow} (MPa) is flow stress which is equal to σ_y+69 [1]. For short corrosion defects (i.e., z<50, where $z=l_c^2/D_o t$):

$$M = \left(1 + 0.6275z - 0.003375z^2\right)^{1/2} \tag{4.13}$$

For z>50 (i.e., long corrosion defects),

$$M = 0.032z + 3.3 \tag{4.14}$$

In DNV RP F101 standard, the failure pressure, P_{DNV}, is calculated as [1]:

$$P_{DNV} = \frac{2 \cdot t}{D_o - t} \cdot S_F = \frac{2 \cdot t}{D_o - t} \cdot S_{flow} \cdot \left[\frac{1 - \left(d_c / t\right)}{1 - \left(d_c / t\right)/M} \right] \tag{4.15}$$

where the flow stress S_{flow}=1.05σ_U [53], and

$$M = \sqrt{1 + 0.31 \cdot \frac{l^2}{D_o t}} \tag{4.16}$$

If the failure pressure calculated by Eq. (4.12) or (4.15) is smaller than operating pressure (p) multiplied by a safety factor S_F, the pipelines are required for repair or replacement. Apparently,

the calculated failure pressure of corroded pipelines depends on length and depth of the corrosion defect, while the corrosion defect growth vs. time is ignored.

It is generally believed [53, 177] that the modified ASME B31G method is more conservative for estimation of the burst pressure, as shown in Table 4.4. However, the error of the modified ASME B31G is much greater than the error of DNV RP F101. Thus, further investigations were conducted using DNV RP F101 as a base for comparison to improve the assessment accuracy.

Table 4.4 Comparison of the burst pressures obtained by FE model developed in this work as compared with the results from the modified ASME B31G and DNV RP F101 methods.

d_c (mm)	l_{c0} (mm)	Burst pressure P (MPa)				
		FE	Modified ASME B31G	Difference (%)	DNV RP F101	Difference (%)
2	39.6	24.438	23.071	5.6	25.420	3.9
3	39.6	24.310	22.598	7.0	25.037	2.9
4	39.6	23.917	21.986	8.1	24.489	2.3
5	39.6	23.471	21.159	9.9	23.638	0.7
6	39.6	22.993	19.981	13.1	22.135	3.9

Note: The input parameters of the corroded pipeline used for FE modeling include D_o=457 mm, t=8.1 mm. The pipe steel is X80 steel.

4.4.2 A new assessment method for burst pressure of corroded pipelines considering the effect of dent and service time

As stated, the mutual interaction between corrosion defect and dent must be included in failure assessment for an improved pipeline burst prediction accuracy. A dent, when it is located at a corrosion defect, can obviously influence the stress condition at the defect area and then the corrosion growth. Thus, when the dent occurs at corrosion area on pipelines, the failure assessment should include both the pressure-bearing capability of the pipelines and the remaining service life due to dent-enhanced corrosion growth on the pipelines. A new criterion was proposed for assessment of burst pressure capability and remaining service life of corroded pipelines containing dent. For a corroded X80 steel pipe containing a dent, the pressure capacity can be determined by the criterion considering length of corrosion, dent depth and service time. The failure pressure, $P(T_c)$, of the corroded pipe at a certain time, T_c, is calculated by:

$$P\left(T_c\right)=\frac{2\cdot t}{D_o-t}\cdot S_{flow}\cdot\left[\frac{1-\frac{d_c(T_c)}{t}}{1-\frac{d_c(T_c)}{t\cdot M\left(T_c\right)}}\right] \tag{4.17}$$

$$M\left(T_c\right)=\sqrt{1+0.31\cdot\frac{l_c^{\,2}\left(T_c\right)}{D_o t}} \tag{4.18}$$

Fig. 4.9 shows the relationship between failure pressure and service time for a corroded X80 steel pipe with various initial corrosion depths and dent depths. It is seen that the failure pressure decreases with time, as expected. The dent depth affects remarkably the failure pressure. For deep corrosion defects such as 5.4 mm in depth, the failure pressure is lower at specific times, compared

with the pipe containing a corrosion defect of 2 mm in depth. Particularly, for pipelines containing deep corrosion defects, the co-presence of a deeper dent (i.e., over 30 mm in depth) makes the failure pressure decreases much more rapidly with time, as compared with the pipe containing a dent with the depth smaller than 30 mm. However, as shown in Fig. 4.9, an opposite tendency is observed for the pipelines containing shallow corrosion defects due to different stress-enhanced corrosion rates as presented in Table 4.3.

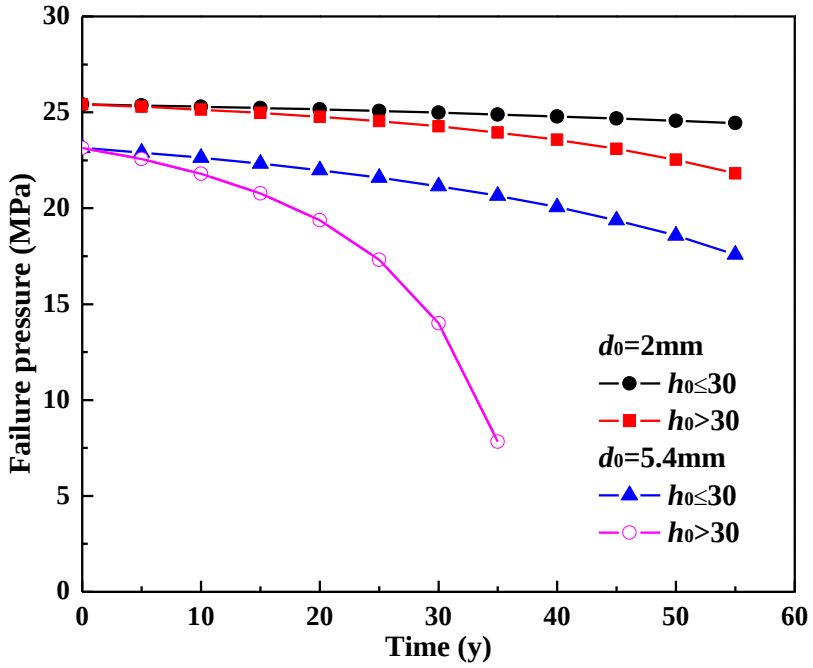

Figure 4.9 Relationship between failure pressure $P(T_c)$ and service time T_c for a corroded X80 steel pipe with various initial corrosion depths and dent depths. The initial corrosion defect length is l_{c0}=39.6 mm.

After the steel pipe is dented in the absence of an internal pressure and the indenter is removed, a spring-back process happens due to elasticity of the material. When an internal pressure is applied on the pre-dented pipe, a further reduction of the dent depth will occur. Thus, the measured dent

depth is deviated from the initial depth. Although the spring-back behavior of dented pipelines has been investigated [12, 73, 168], there has been rare work conducted on corroded pipelines. According to the FE model in this work, the initial depth h_0 and instant depth h of the dent can be obtained. Fig. 4.10 shows the relationship between the dent depth (h) under internal pressure (p) and the initial dent depth (h_0) of a corroded X80 steel pipe with various initial corrosion depths. It is seen that, as the initial corrosion depth increases, the dent depth decreases at specific initial dent depth h_0. This means that the dent, upon spring-back, will become shallower if it is created at a deeper corrosion defect.

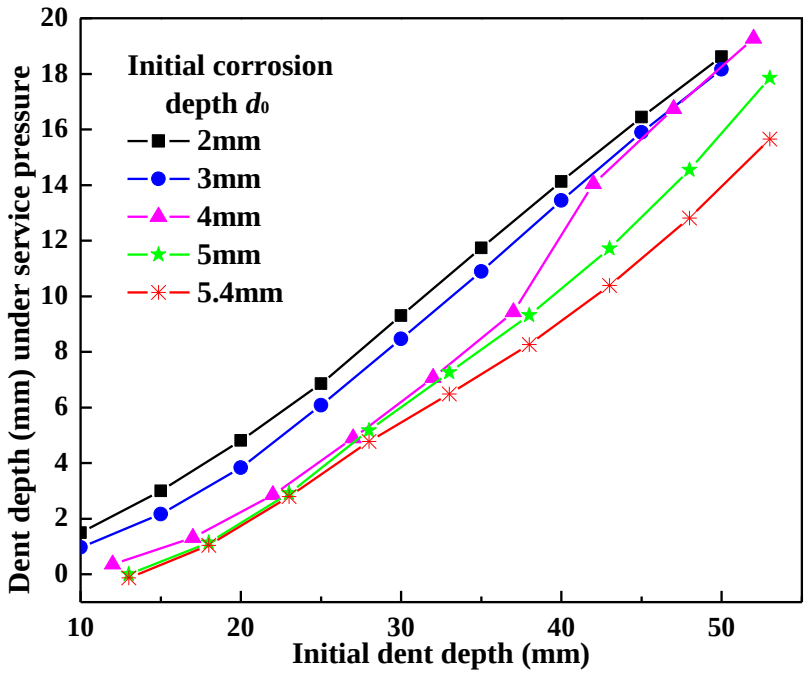

Figure 4.10 Relationship between dent depth (h) under internal pressure (p) and the initial dent depth (h_0) on a corroded X80 steel pipe with various initial corrosion depths.

Furthermore, the relationships shown in Fig. 4.10 that the dent depth h increases linearly with initial depth h_0 by:

$$h = 0.435h_0 - 1.115d_0 - 1.209 \quad (4.19)$$

It is noted that the derived Eq. (4.19) is based on the FE modeling defined in this work. When the pipeline and defect parameters change, the relationship will be re-derived.

4.4.3 Implication on failure assessment of corroded pipelines containing dent

In practice, most surface defects such as dents and corrosion on pipeline are generally acceptable for continuous operation, while the dent-corrosion interaction is usually ignored, especially the corrosion defect growth with time. Both the interaction and the corrosion growth affect the pipeline's pressure capability and remaining service life. According to the new assessment method developed in this work, the following steps should be followed:

(1) Measure geometric parameters of corrosion defect and dent, and determine their initial depths based on empirical equation such as Eq. (4.19).

(2) Estimate the initial pressure capacity, $P(0)$, of the pipeline using Eq. (4.15) before the corrosion defect starts to grow. If $P(0)<S_F \times p$, the pipeline may fail during service. The segment containing the defects should be repaired or replaced.

(3) If $P(0)>S_F \times p$, the pipeline can bear the operating pressure and continue the service. However, the corrosion defect growth over service time should be considered and estimated by the developed model. If the pressure capacity decreases and becomes smaller than p after a certain time T_c, the pipeline should be properly maintained.

Following the assessment steps (1) ~ (3), the failure pressure of the corroded pipelines containing a dent can be determined. Moreover, the remaining service time can be estimated by

determining the corrosion growth rate. It is realized that the remaining life of a pipeline is not only affected by corrosion and dent, but also by other threats such as fatigue and cracking. Thus, a proper pipeline integrity management program should be composed of multiple modeling and assessment of various threats present on the pipeline.

4.5 Conclusions

A new FE-based method is developed for assessment of the burst pressure capability and remaining service life of corroded pipelines containing a dent, while considering mutual interaction of the corrosion defect and the dent. An assessment program containing specific steps is proposed for practical use.

The dent at corrosion defect remarkably changes the stress distribution, elevating the local stress to plastic range. The mutual interaction between the dent and the corrosion defect depends on the corrosion depth. At a deep corrosion defect (e.g., 5.4 mm in depth), the stress level at the corrosion defect increases with increased initial dent depth. Whereas for a shallow corrosion defect (e.g., 2.0 mm in depth), the local stress decreases as initial dent depth increases.

The mutual interaction between corrosion defect and dent affects the corrosion defect growth, and the effect depends on both the initial corrosion depth and the initial dent depth. The corrosion grows more rapidly along the depth direction than the longitudinal direction, especially for shallow corrosion defects, e.g., 2.0 mm in initial depth. The mutual interaction between corrosion defect and dent must be included in pipeline burst failure assessment. The failure assessment should include both the pressure-bearing capability of the pipelines and the remaining service life due to the dent-enhanced corrosion growth. The presence of a deep dent (i.e., >30 mm in depth) makes the burst pressure decrease more rapidly with time.

Chapter Five: Assessment by finite element modeling of corrosion in dent on X52 steel pipelines[§]

5.1 Introduction

In Chapter Four, the burst pressure prediction considering corrosion growth in the dent defect was investigated based on the M-E interaction theory, where the electrochemical force was not considered in the modeling. Relative research is limited in literature especially using FE method. The novelty of this chapter is to develop a new FE-based method to assess the corrosion in dent on an unconstrained dented pipeline exposed to a typical corrosive environment, where the M-E interaction is integrated in the model. The research addresses a problem highly relevant to pipeline failure prediction and integrity management.

In this chapter, FE modeling was conducted on an X52 steel pipe containing corrosion in a dent exposed to a deoxygenated, near-neutral pH electrolyte (i.e., the so-called NS4 solution) with consideration of the M-E interaction. Potentiodynamic polarization was measured on the steel to obtain electrochemical corrosion parameters in the solution. A 3-D FE model was developed to simulate the denting and spring-back processes, as well as corrosion reactions. The distributions of stress and the corrosion-related parameters such as anodic current density, net current density and corrosion potential at the dent were determined. Parametric effects, including the dent depth, dent size (i.e., the open mouth diameter for spherical dents created by indenters) and internal pressure, were investigated. The corrosion growth rate, as quantified by the anodic current density, at the dent was estimated.

[§] The work in this chapter has been published as:

Jian Zhao, Y. Frank Cheng, Assessment by finite element modeling of corrosion in dent on X52 steel pipelines, *International Journal of Pressure Vessels and Piping*, 200 (2022) 104835. https://doi.org/10.1016/j.ijpvp.2022.104835

5.2 Potentiodynamic polarization measurements of X52 steel in NS4 solution

Potentiodynamic polarization was measured on X52 steel in NS4 solution using a Gamary Reference 600 electrochemical workstation. The specimen was cut from an X52 steel plate, with the chemical composition (wt.%): C 0.24, Mn 1.40, Si 0.45, P 0.025, S 0.015, V 0.10, Nb 0.05 Ti 0.04, and Fe balance. The specimen was sealed with epoxy, leaving a working face of 10 mm × 10 mm in area. The working face was ground by SiC papers up to 1200 grit. The prepared NS4 solution was deoxygenated by purging 5% CO_2 to achieve a pH of 6.8. The remaining dissolved oxygen in the solution was below 0.1 ppm, as measured by a dissolved oxygen meter. The CO_2-gassing was maintained during testing at ambient temperature (22 ℃). To ensure reproducibility of the measurement results, all tests were repeated at least three times.

Prior to potentiodynamic polarization measurements, the steel specimen was immersed in NS4 solution for 1 h to let the open-circuit potential to reach a relatively steady value. The polarization curve was then measured on the specimen, while using a saturated calomel electrode (SCE) as reference electrode and a platinum wire as counter electrode (CE). The potential sweep rate was 0.1667 mV/s. The measured polarization curve is shown in Fig. 5.1. During corrosion of X52 pipe steel in NS4 solution, the electrochemical anodic and cathodic reactions are oxidation of iron and the hydrogen evolution, respectively [178]. The anodic and cathodic reaction equilibrium potentials, i.e., $\varphi_{a,eq}$ and $\varphi_{c,eq}$, are calculated by Nernst equations:

$$\varphi_{a,eq} = \varphi^0_{Fe^{2+}/Fe} + \frac{0.059}{2}\log\left[Fe^{2+}\right] \tag{5.1}$$

$$\varphi_{c,eq} = \varphi^0_{H_2/H^+} + 0.059\log\left[H^+\right] = -0.059\text{pH} \tag{5.2}$$

where φ^0 is standard equilibrium potential, which are -0.409 V (standard hydrogen electrode, SHE) and 0 V (SHE) for anodic and cathodic reactions, respectively [24]. The concentration of Fe^{2+}, i.e., $[Fe^{2+}]$, is assumed to be 10^{-6} M [24]. The solution pH is 6.8 and thus the hydrogen ion concentration, i.e., $[H^+]$, can be solved. The $\varphi_{a,eq}$ and $\varphi_{c,eq}$ are then calculated to be -0.827 V (SCE) and -0.642 V (SCE), respectively.

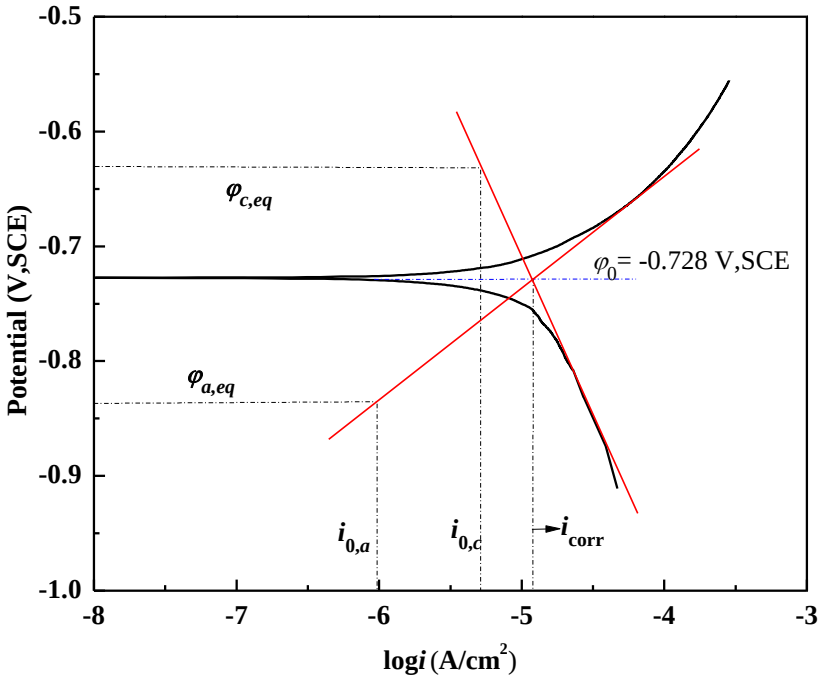

Figure 5.1 Potentiodynamic polarization curve of X52 pipe steel in deoxygenated, near-neutral pH NS4 solution.

It has been established that corrosion of pipeline steels in deoxygenated, near-neutral pH solutions is charge transfer-controlled [178]. Thus, the anodic and cathodic Tafel equations are used to determine the anodic and cathodic current densities, i.e., i_a and i_c, by:

$$i_a = i_{0,a} \times 10^{\frac{\eta_a}{\beta_a}} \tag{5.3}$$

$$i_c = i_{0,c} \times 10^{\frac{\eta_c}{\beta_c}} \tag{5.4}$$

where η_a and η_c are anodic and cathodic reaction overpotentials, respectively, $i_{0,a}$ and $i_{0,c}$ are anodic and cathodic exchange current densities, respectively, β is Tofel slope, which can be derived from the measured polarization curve in Fig. 5.1. The corrosion current density, i_{corr}, is determined to be 11.8 μA/cm^2. For FE modeling, the required initial electrochemical corrosion parameters are listed in Table 5.1.

Table 5.1 Initial electrochemical corrosion parameters required for FE modeling.

Reactions	logi_0 (μA/cm^2)	i_0 (μA/cm^2)	φ_{eq} (V,SCE)	Tofel slope (V/decade)
Anode	-6.032	0.929	-0.827	0.094
Cathode	-5.339	4.581	-0.642	-0.250

5.3 FE modeling

5.3.1 Material and geometric definition

The FE modeling in this work was conducted by coupling of a mechanical stress field and an electrochemical corrosion field at a dent, where corrosion occurred, on a pipe segment. The COMSOL software was used for 3-D analysis of denting process, electrochemical corrosion calculations and the M-E interaction. The mechanical properties of X52 steel and the geometric parameters of the pipe segment are listed in Table 5.2. The ratio of L_1/D_o is over 5.5, ensuring that the pipe segment is sufficiently long to avoid the boundary effect. Rigid material properties were

applied for a spherical indenter which was used to create a dent on the pipe. To investigate the influence of dent size (i.e., the open mouth diameter of a spherical dent), the diameters of the indenter (D_2) were 20 mm, 60 mm, 100 mm, 140 mm, 180 mm and 220 mm.

Table 5.2 Mechanical properties of X52 pipe steel and geometric parameters of the pipe segment used in this chapter.

Steel grade	D_o (mm)	t (mm)	L_1 (mm)	E (GPa)	υ	σ_y (MPa)	σ_U (MPa)
API 5L X52	720	8.1	4000	208	0.3	375	468

Denting is an irreversible deformation, modeling of the denting process in the mechanical stress field is highly nonlinear. Based on the true stress-strain relationship of X52 steel, an isotropic hardening model is used to simulate the hardening effect during a large plastic deformation caused by denting [24]:

$$\sigma_{\text{yhard}} = \sigma_{\text{exp}}\left(\varepsilon_{\text{p}} + \frac{\sigma_{\text{e}}}{E}\right) - \sigma_{\text{y}} \tag{5.5}$$

where σ_{exp} is an experimental stress function that can be obtained by fitting the true stress-strain curve using the R–O model, ε_{p} is plastic strain, and σ_{e} is effective stress.

5.3.2 Coupling of mechanical and electrochemical corrosion fields

It is established that corrosion of steels can be affected by stress due to the M-E interaction. Particularly, the corrosion rate of the steels increases with a plastic stress or strain. According to the M-E interaction concept, the change in anodic reaction equilibrium potential due to elastic and

plastic deformations, i.e., $\Delta\varphi^{e}_{a,eq}$ and $\Delta\varphi^{p}_{a,eq}$, are [179]:

$$\Delta\varphi^{e}_{a,eq} = -\frac{\Delta P V_m}{zF} \tag{5.6}$$

$$\Delta\varphi^{p}_{a,eq} = -\frac{TR}{zF}\ln\left(\frac{\mu\alpha_e}{N_0}\varepsilon_p + 1\right) \tag{5.7}$$

where superscripts e and p refer to the elastic and plastic deformations, respectively, V_m is molar volume of steels (i.e., 7.13×10^{-6} m^3/mol), z is number of charges exchanged during corrosion (z=2 for steels), F is Faraday's constant (i.e., 96,485 C/mol), T is absolute temperature (K), R is ideal gas constant (i.e., 8.314 J/mol K), μ is an orientation-dependent factor (i.e., 0.45), α_e is a coefficient (i.e., 1.67×10^{11} cm^{-2}), N_0 is initial density of dislocations before plastic deformation (i.e., 1×10^{8} cm^{-2}), and ΔP_m is excess pressure and is equal to 1/3 of yield strength of the steels [1]. ΔP is usually calculated from hoop stress (σ_θ) and axial stress (σ_z) of a pipeline by:

$$\Delta P = \frac{1}{3}\left(\sigma_\theta + \sigma_z\right) \tag{5.8}$$

When the pipe steel experiences both elastic and plastic deformations, the anodic reaction equilibrium potential is written as:

$$\varphi_{a,eq} = \varphi^{0}_{a,eq} - \frac{\Delta P_m V_m}{zF} - \frac{TR}{zF}\ln\left(\frac{\mu\alpha_e}{N_0}\varepsilon_p + 1\right) \tag{5.9}$$

The increased anodic current density upon plastic deformation can be measured by potentiodynamic polarization. The cathodic current density, i_c, is determined by a semi-empirical expression under plastic strain [24]:

$$i_c = i_{0,c} \times 10^{\frac{\sigma_{\text{Mises}} V_m}{6F(-b_c)}} \tag{5.10}$$

In addition, the conductivities of the solution and the steel used in FE modeling are determined as 0.096 S/m and 10^6 S/m, respectively.

5.3.3 The FE modeling and analysis of element size sensitivity

Three steps were included in FE modeling of corrosion in dent on a steel pipe, i.e., denting, pressurizing, and electrochemical corrosion analysis. For analysis of the solid mechanics, the pipe segment was dented by a spherical indenter with various diameters. The indenter was then removed to generate an unconstrained dent. After the indenter was removed, a spring-back phenomenon occurred to partially recover the created dent. The residual dent was generated due to plastic deformation. The electrochemical corrosion modeling was conducted using the results from solid mechanics analysis as the initial conditions. Parametric effects including the dent depth, internal pressure and indenter size on corrosion at the dent were determined.

Fig. 5.2 shows a model for a pipe segment, an indenter, and the solution the pipe steel is exposed to, where *x*, *y* and *z* axes refer to circumferential, radial and longitudinal directions, respectively. Geometric parameters of the pipe segment are listed in Table 5.2, and the diameter of the indenter (D_2) is 100 mm. The indenter was placed on the top of the pipe and moved along the *y* direction towards the pipe thickness. The solution was modeled as a block, as colored blue

in Fig. 5.2 (b), covering the dent area. As stated previously, the steel corrodes in NS4 solution, where the steel corrosion is activation-controlled. In other words, the mass transfer step of corrosive species in the solution does not control the corrosion process. It is thus believed that the dimension of the electrolyte in the developed model does not affect corrosion. However, the corrosion occurs at the interface between the electrolyte and the pipe steel. As a result, the area for corrosion reaction to occur should be large enough to cover the entire dent, controlling the scale of the grids. The indenter volume was a part of the solution during electrochemical modeling. The entire model was built as a quarter of symmetric one to reduce the degree of freedom (DOF) and save computational time. Direct solvers were used for both solid mechanics and electrochemical corrosion analysis.

Denting on the pipe was the first step of the solid mechanic analysis, where the indenter moved downward and contacted the pipe surface. The contact pair was defined, as shown in Fig. 5.2 (c), where the indenter surface was designated as the source boundary and the outer surface of the pipe was the destination boundary. A fixed boundary condition was applied on the bottom line of the pipe during the denting. For cross sections of the pipe and the indenter, symmetrical conditions were applied and marked as “s” in Fig. 5.2. A prescribed displacement in y direction for the indenter varied from 10 mm to 67 mm, which were defined as the initial dent depth, h_0. After removal of the indenter, the dent depth decreases from h_0 to h due to spring-back, and h is the final dent depth. Stress and strain in the dent area become more complicated after the spring-back. Relationships between the dent depth and the strain before and after the spring-back were investigated in Chapter Three. The second step of the solid mechanics modeling is to apply various internal pressures on the interior of the pipe to study the effect of internal pressure on corrosion in dent. Corrosion analysis was based on the secondary current distribution method, and the M-E

interaction was included in modeling using the mechanics analysis results as the initial values. Both anodic and cathodic reactions occurred at the interface between the solution and the pipe steel. A direct solver was used to derive corrosion current density and corrosion potential.

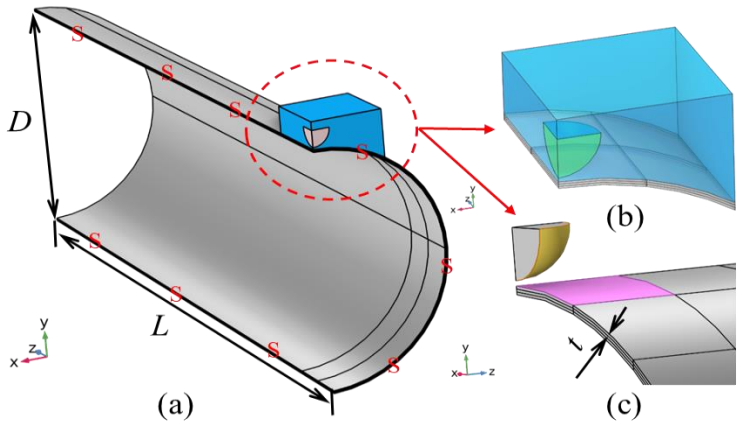

Figure 5.2 Modeling of a pipe segment, an indenter, and the solution the pipe steel is exposed to.

Hexahedral elements were assigned on both the pipe and the indenter, while the solution was meshed as tetrahedral elements, as shown in Fig. 5.3. Meshing of the pipe segment was divided into three parts. The dent area has the greatest element density. The indenter has the same element size as the dent, which is beneficial to convergence of the contact simulation. The solution has a relatively coarse meshing. Generally, a dense meshing in the dent area contributes to an improved accuracy of FE modeling but may increase the computational time. It is thus important to define a reasonable element size that can reduce the computing time and maintain the modeling accuracy. The element size of the dent area changed from 2 mm to 10 mm. The sensitivity analysis of element size for FE modeling of the mechanical and electrochemical corrosion fields is shown in Fig. 5.4. Both the equivalent plastic strain and the maximum anodic current density were obtained after

spring-back when the initial dent depth was set as 45 mm (i.e., 6.25%D_o). It is seen that, as the element size decreases, the results tend to be relatively stable. Thus, the element size of the dent area was selected as 3 mm.

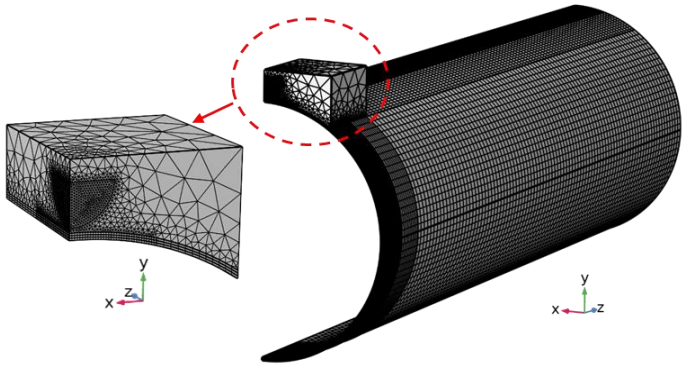

Figure 5.3 Meshing of the pipe, the indenter, and the solution during FE modeling.

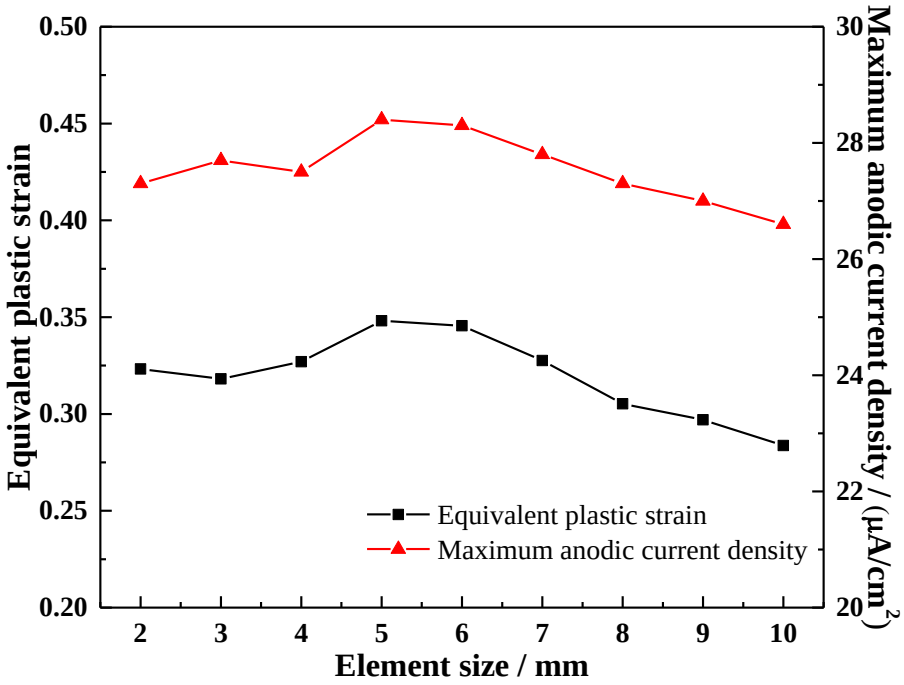

Figure 5.4 Sensitivity analysis of element size for FE modeling of the mechanical and electrochemical corrosion fields.

5.4 Results and discussion

5.4.1 Validation of the modeling results with literature data and theoretical calculations

To validate the developed model in this work, the modeling results in both mechanical and electrochemical corrosion fields were compared with theoretical calculations. The anodic current density of a stressed steel, i_a', can be written as [180]:

$$i_a^{'} = i_a \exp\left(\frac{\Delta P V_m}{RT}\right) \tag{5.11}$$

According to solid mechanics theory, the first principal stress, σ_1, for a pipeline with internal pressure is:

$$\sigma_1 = \frac{pD_o}{2t} \tag{5.12}$$

The comparison of the first principal stress and anodic current density obtained from the developed model and the theoretical calculations under various internal pressures are listed in Table 5.3, where the relative errors are also included. It is seen that the modeling results and the theoretical calculations are consistent with acceptable relative errors.

Experimental testing and numerical calculations for indentation process were performed by Shuai et al. [11]. During FE analysis, the equivalent load calculated by Eq. (4.4), p_e, was applied on both ends of the pipe segment to simulate the effect of end caps. Comparisons between the measured axial and hoop strains at the dent center and the modeling results under various internal

pressures are consistent with Fig. 3.4. Although different FE software were used in Chapter Three and this chapter, the strain calculation results were consistent. Moreover, the FE modeling shows that the initial hoop and axial strains at the dent center are negative after spring-back, indicating that a compressive effect occurs locally. When the internal pressure increases, the compressive load increases in the axial direction and decreases in the hoop direction.

Table 5.3 Comparison of the first principal stress and anodic current density obtained from the developed model and the theoretical calculations under various internal pressures.

Internal pressure (MPa)		2	3	4	5	6
σ_1 (MPa)	Theoretical	88.89	133.33	177.78	222.22	266.67
	FE modeling	88.49	132.57	176.65	220.74	264.86
	Relative error (%)	0.45	0.57	0.60	0.67	0.68
i_a' ($\mu A/cm^2$)	Theoretical	11.87	12.69	13.56	14.51	15.51
	FE modeling	11.13	12.01	12.92	13.88	14.89
	Relative error (%)	6.60	5.67	4.92	4.54	4.20

5.4.2 Modeling of the M-E interaction for corrosion in dent

As discussed previously (Chapter Three), when the initial dent depth, h_0, exceeded 8% of the pipe outer diameter, the maximum equivalent strain would deviate from the dent center. As a result, the corrosion growth at the dent is difficult to estimate.

In this chapter, electrochemical corrosion modeling was conducted on the dented pipe while considering the effect of the dent depth. Modeling results of von-Mises stress, anodic current

density and net current density at a dent with various initial dent depths after spring-back are shown in Fig. 5.5, where the net current density is the sum of anodic and cathodic current densities and is present by the density of the arrows in the solution. Generally, as the initial dent depth decreases, both the residual depth of the dent and the residual stress do not reduce remarkably after spring-back. It is seen that, as the initial dent depth h_0 increase, the maximum von-Mises stress on the outer pipe surface deviates from the dent center. The high stress area expands towards the dent sides with increased h_0. Both the maximum net current density and the maximum anodic current density are observed at the dent center with various initial dent depths. Moreover, the anodic reaction area, i.e., the corrosion area, increases as the initial dent depth increases.

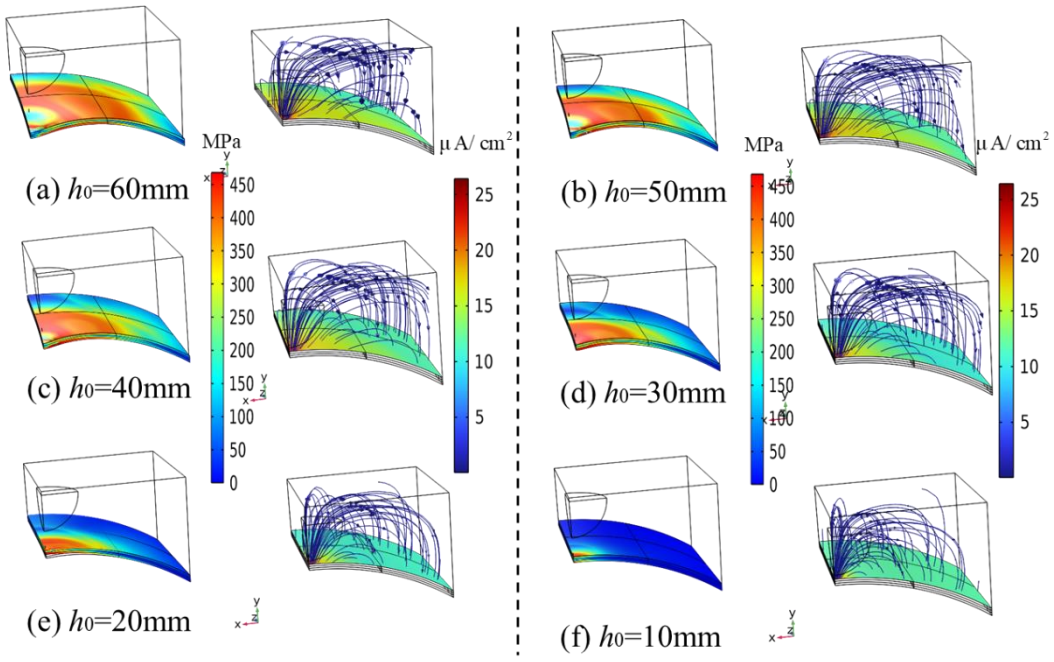

Figure 5.5 Modeling results of von-Mises stress, anodic current density and net current density at a dent with various initial dent depths after spring-back, where the net current density is present by the density of the arrows in the solution.

When a pipe containing unconstrained dents is in service, the residual dent depth and the local stress tend to decrease when the internal pressure is applied [86, 181]. According to the M-E interaction, the electrochemical corrosion is affected by the stress level. Fig. 5.6 shows the anodic current density at the dent with various initial dent depths as a function of internal pressure. It is seen that there is little influence of the internal pressure on the maximum anodic current density, i.e., corrosion rate, at the dent. This is mainly attributed to the reduced stress concentration upon the application of internal pressure. As a result, most of the area at the dent is under an elastic deformation, as modeled previously [86, 181]. According to the M-E interaction theory, the corrosion is rarely affected by an elastic stress. However, the local stress concentration is heavily affected by the dent depth. Under specific internal pressures, the maximum anodic current density increases as the dent depth increases.

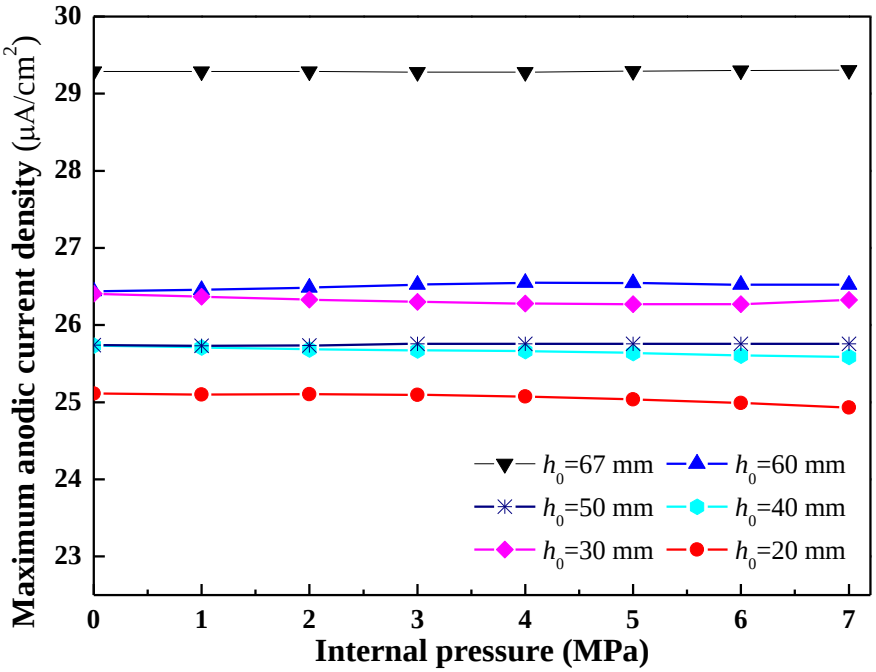

Figure 5.6 Maximum anodic current density at the dent with various initial dent depths as a function of internal pressure.

To further investigate the electrochemical corrosion behavior at the dent with various initial depths, the distributions of anodic current density in the circumferential and longitudinal directions of the pipe are shown in Fig. 5.7, where a constant internal pressure of 6 MPa is applied. It is seen that the anodic current density decreases as the distance from the dent increases. When it is far away from the dent, the anodic current density is approximately constant at about 10.5 $\mu A/cm^2$, which is 2.5–3 times less than the maximum anodic current density recorded at the dent. A deeper dent is always associated with a higher level of anodic current density. Moreover, a deeper dent causes a bigger area with an enhanced anodic current density.

As stated above, the net current density is the sum of anodic and cathodic current densities during corrosion. When corrosion is in an equilibrium state, the net current density is zero. Fig. 5.8 shows the net current density in the circumferential and longitudinal directions as a function of the distance from the dent center. Compared with Fig. 5.7, there is a similar distribution of the net current density to the anodic current density. At the dent center, there is the greatest positive net current density, indicating that anodic dissolution (i.e., corrosion) occurs locally. As the distance from the dent increases, the net current density decreases, but still maintains positively. The results mean that the areas nearby the dent experiences corrosion but at a reduced corrosion rate. The changes of the net current density further confirm the effect of the M-E interaction that the steel corrosion is accelerated by a local stress concentration at the dent. The net current density is the sum of anodic and cathodic current densities, thus a negative net current density indicates that the cathodic reaction (i.e., hydrogen evolution in this work) is faster than the anodic reaction (i.e., the iron dissolution). It is thus seen from the modeling results that the cathodic protection mainly occurs at the sides of the dent, while the dent center suffers from the anodic dissolution.

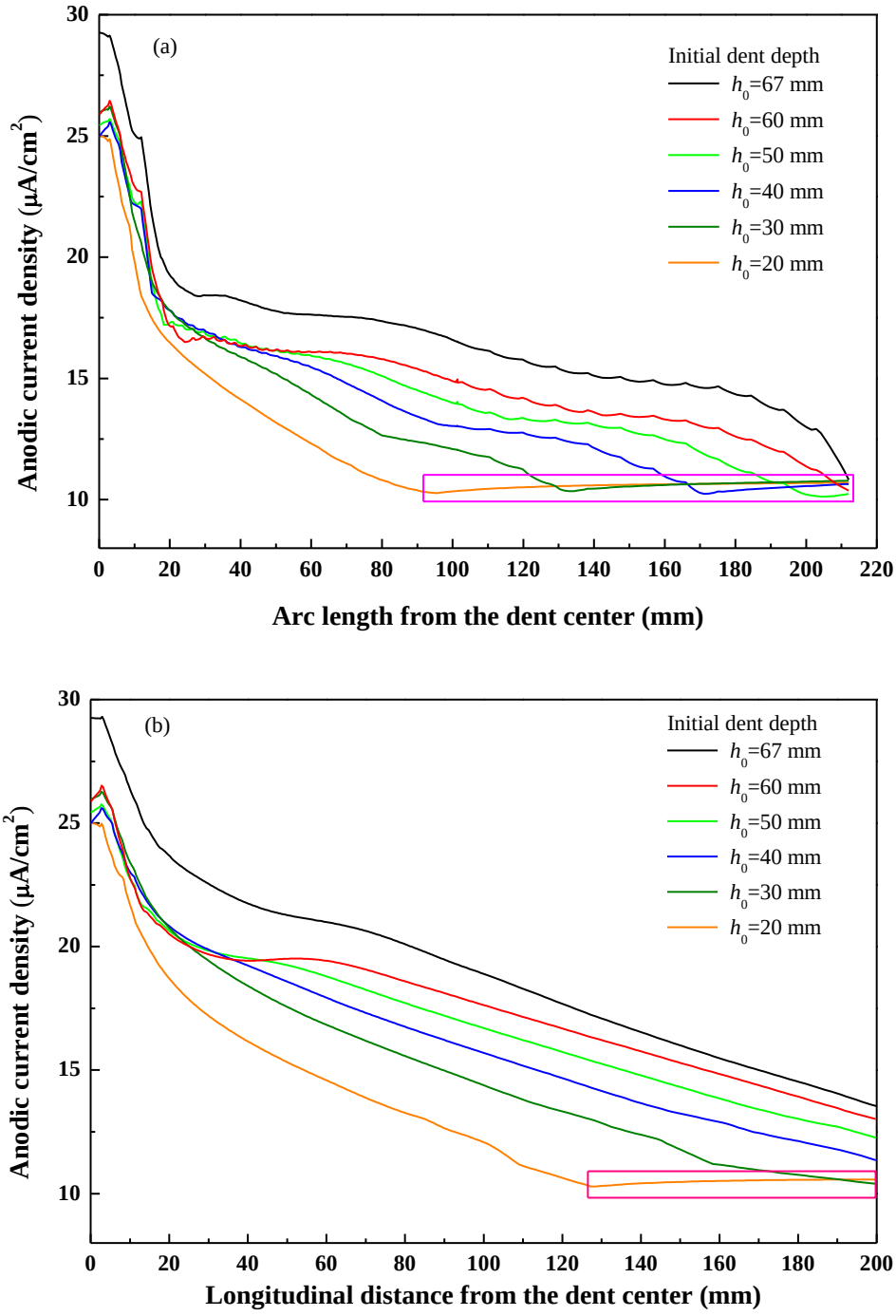

Figure 5.7 Distributions of anodic current density at the dent with various initial dent depths in the (a) circumferential and (b) longitudinal directions.

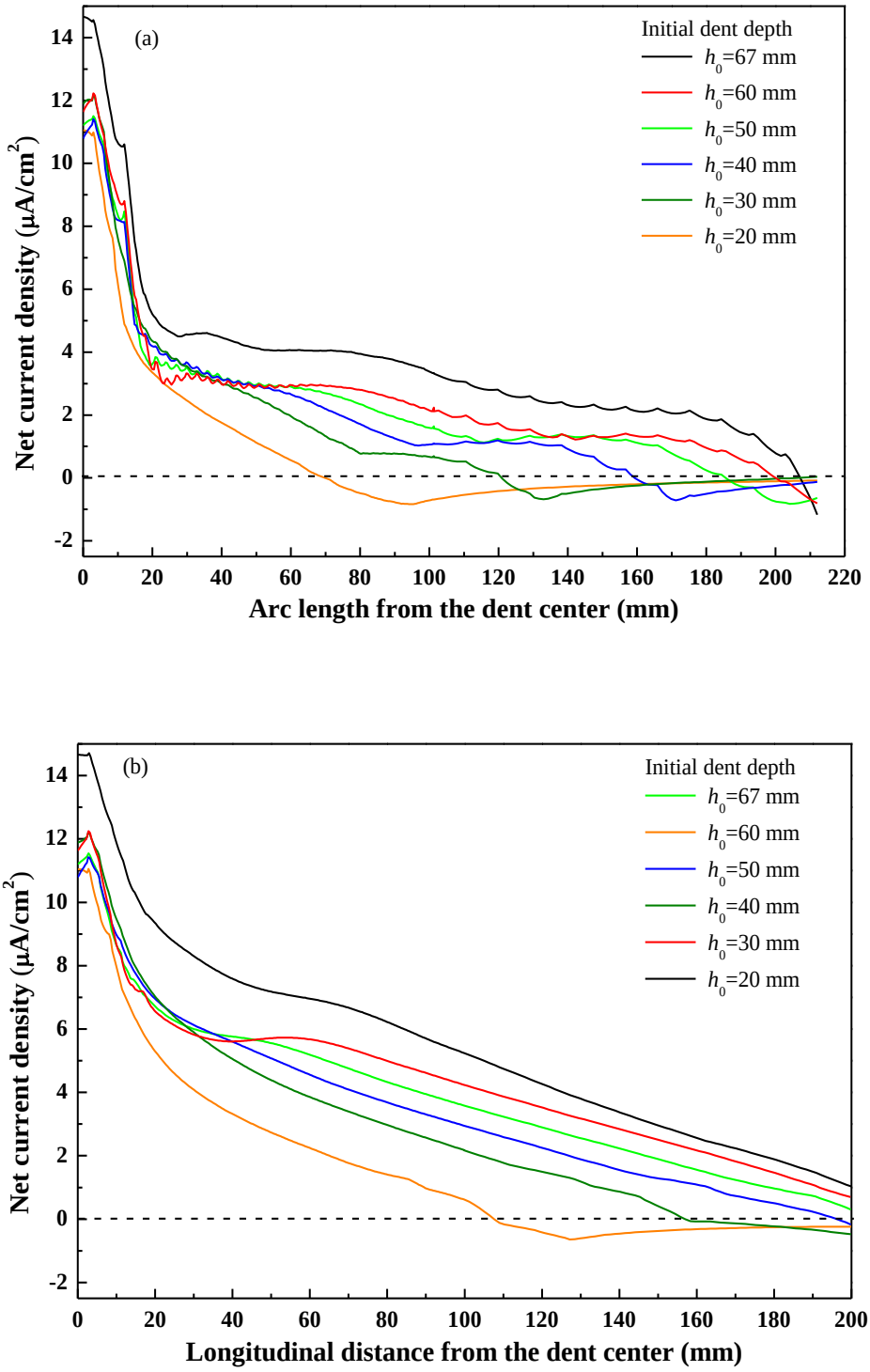

Figure 5.8 Distributions of the net current density in the (a) circumferential and (b) longitudinal directions as a function of the distance from the dent center.

Modeling was also conducted to determine corrosion potential at the dent with various initial dent depths under varied internal pressures, and the results are shown in Fig. 5.9. It is seen that, as the dent depth increases, the corrosion potential at the dent becomes more negative. For example, when h_0 increases from 10 mm to 67 mm, the corrosion potential is negatively shifted by about 29 mV at the dent. Generally, a negative corrosion potential is associated with an increased corrosion activity of the steel. Thus, an increased dent depth elevates the local corrosion activity at the dent. At specific dent depths, the internal pressure does not affect the corrosion potential apparently.

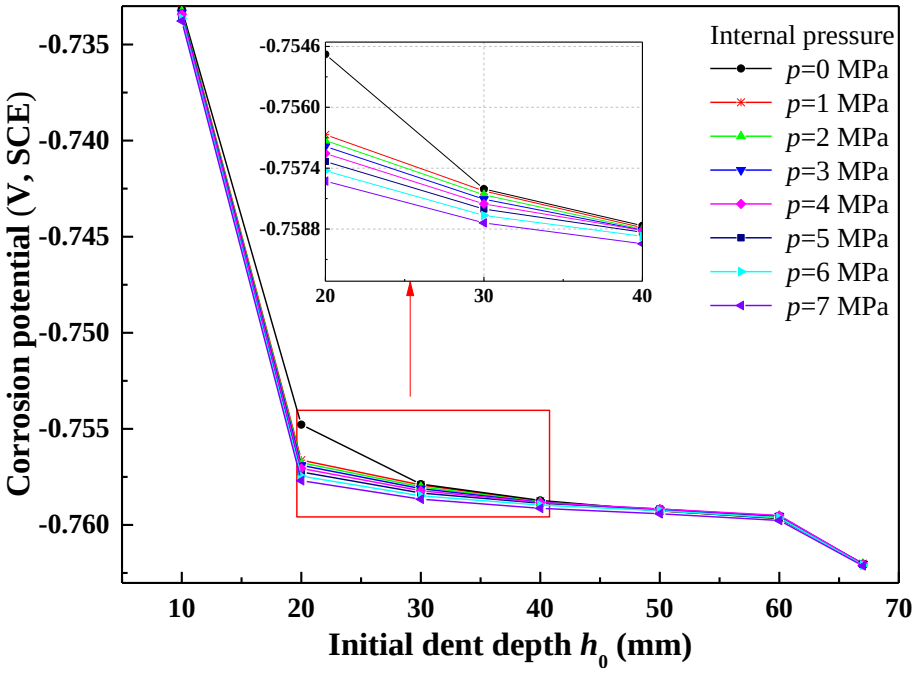

Figure 5.9 Corrosion potential at the dent with various initial dent depths (h_0) under varied internal pressures.

5.4.3 Influence of the indenter size on corrosion in dent

The indenter size, which is defined as the open mouth diameter for a spheric indenter, can remarkably influence the local stress level at the dent [47], which, in turn, affects the corrosion in

dent. Fig. 5.10 shows the distributions of von-Mises stress and corrosion potential at the dent produced by various indenter sizes on the pipe, while the initial dent depth and internal pressure are kept constant at h_0=40 mm and p=6 MPa, respectively. Arrows in the corrosion potential diagrams refer to the net current density in the solution, where denser arrows indicate a greater net current density. The deformation around the dent decreases with larger indenter sizes. A more negative corrosion potential exists at the dent and becomes more negative as the indenter is smaller. The net current density generates at the dent and flows to the area which is away from the dent.

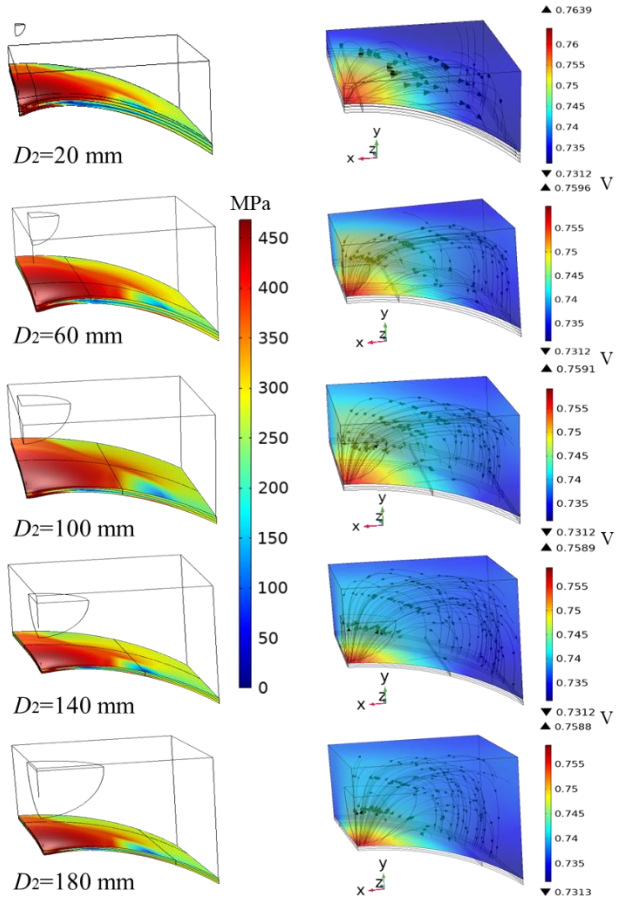

Figure 5.10 Distributions of von-Mises stress, corrosion potential (negatively signed, vs. SCE) and net current density at the dent with varied sizes (D_2). The initial dent depth and internal pressure are constant at h_0=40 mm and p=6 MPa, respectively.

Fig. 5.11 shows the distribution of von Mises stress along the circumferential and longitudinal directions as a function of the distance from the dent which is created an indenter with various sizes. It is seen that the stress fluctuates considerably at the dent, especially when the indenter is small (e.g., 20 mm and 60 mm). This is attributed to a strain hardening resulted from a big plastic deformation, leading to a nonuniform stress distribution. A big plastic area with the stress level exceeding the yielding strength of the steel is produced on the pipe. In addition, the stress level in the longitudinal direction is higher and the plastic area is bigger than in the circumferential direction. It is thus expected that the corrosion reduces more rapidly in the circumferential direction.

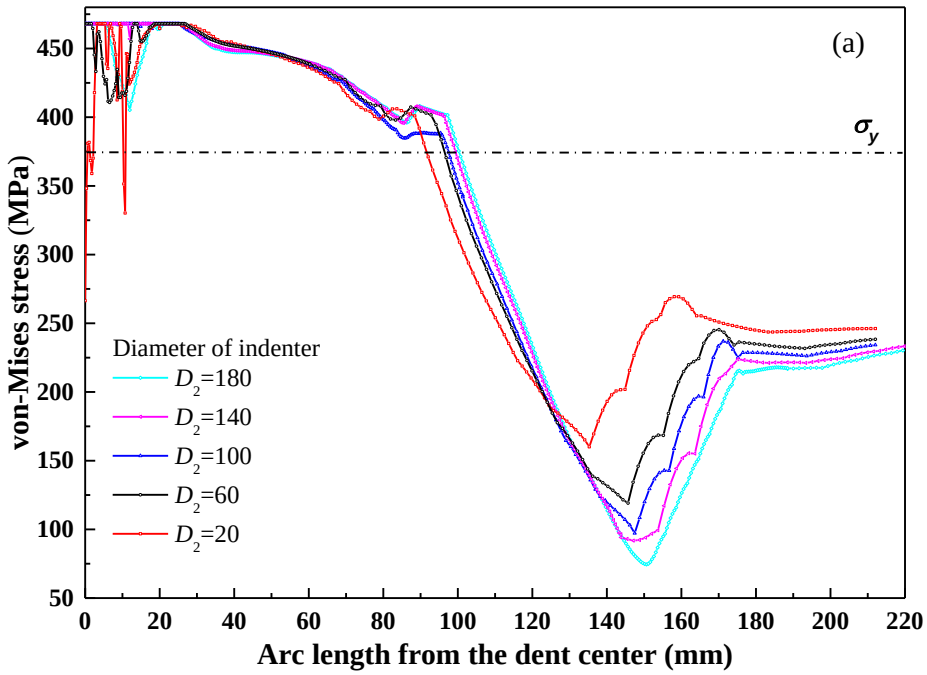

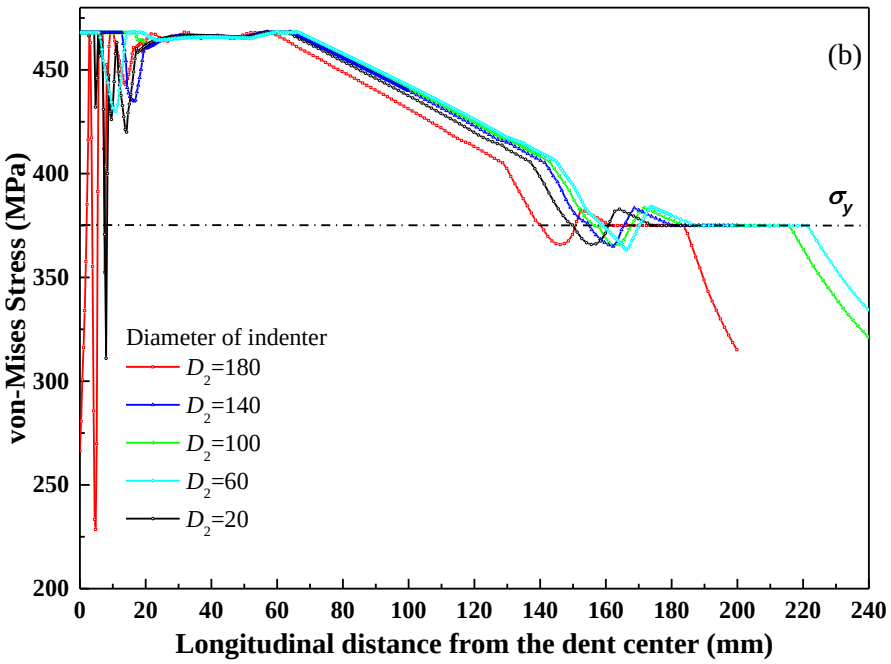

Figure 5.11 Distribution of von Mises stress along the (a) circumferential and (b) longitudinal directions as a function of the distance from the dent created by an indenter with various sizes.

The distribution of net current density along the circumferential and longitudinal directions at the dent created by an indenter with various sizes is shown in Fig. 5.12. It is seen that, in both directions, the maximum net current density occurs at the dent center and decreases rapidly with the increasing distance from the dent. Note that the maximum net current densities are not always located at the dent center, especially for the small indenter of 20 mm in diameter. The net current density decreases with increased indenter size, indicating that a greater corrosion is caused by a smaller indenter. The maximum net current density in the circumferential direction decreases from 17.10 μA/cm^2 to 9.87 μA/cm^2 when the indenter size increases from 20 mm to 180 mm, while the maximum net current density decreases from 16.47 μA/cm^2 to 9.89 μA/cm^2 in the longitudinal direction. The range with a positive net current density expands as the indenter size increases,

indicating that the anodic reaction area becomes wider for a larger dent.

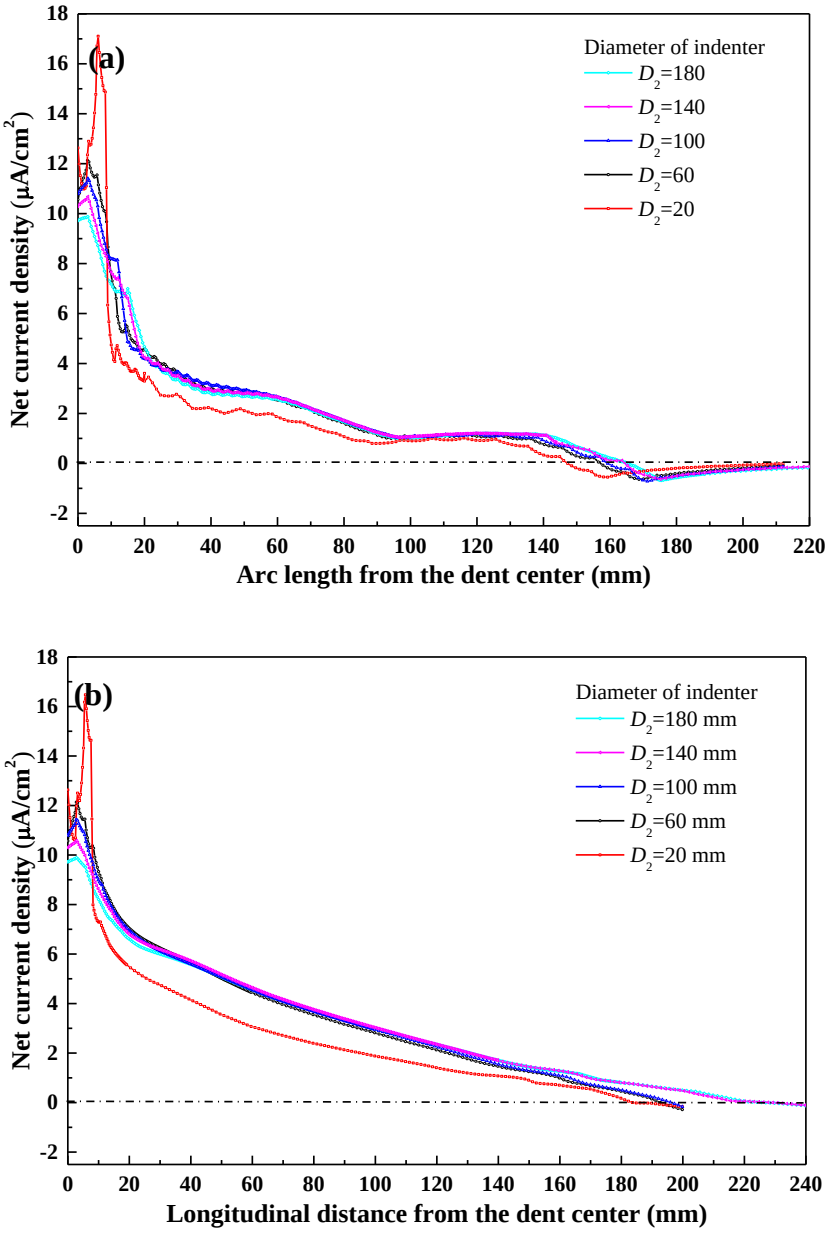

Figure 5.12 Distributions of net current density along the (a) circumferential and (b) longitudinal directions at the dent created by an indenter with various sizes.

The modeling results show that the most negative corrosion potentials under specific

conditions are always located at the dent center. Fig. 5.13 shows the relationship between the corrosion potential at the center of the dent created by an indenter with various diameters and the initial dent depth h_0 with an internal pressure of 16 MPa. It is seen that, as the indenter size decreases, the corrosion potential becomes more negative at specific h_0, indicating an increasing corrosion activity.

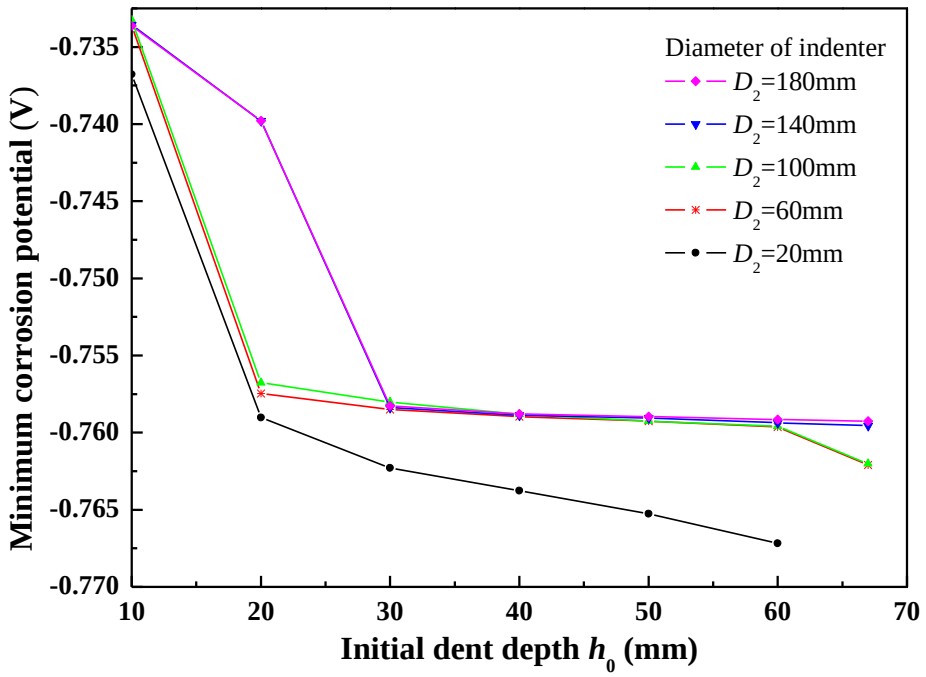

Figure 5.13 Relationship between corrosion potential at the center of the dent created by an indenter with various diameters and the initial dent depth h_0 with an internal pressure of 16 MPa.

5.4.4 Assessment of corrosion in dent on pipelines

This work developed a new approach to assess corrosion in dent on pipelines by considering both the mechanical and electrochemical corrosion factors and their interaction at an unconstrained dent, which is widely encountered in practice, through FE modeling of the denting, spring-back

and pressurizing processes. It is noted that the corrosion appearance was not investigated in this work. Instead, the corrosion rate, i.e., the anodic current density, was investigated as a function of the local stress at the dent. Detailed modeling of corrosion appearance under various conditions such as dent depth will provide useful information about the corrosion growth in dent. It is thus included in the further work plan, while this work focuses on the corrosion rate modeling, which is not affected by the appearance of corrosion. The potential is an indicator of the corrosion thermodynamic activity, and the anodic current density and net current density serve as the kinetics parameters to indicate the corrosion rate. This work demonstrates that the stress factor at the dent affects both corrosion potential and the anodic current density, demonstrating the essential role of the M-E interaction for pipeline corrosion. The stress concentration at the dent always results in a negative shift in corrosion potential (i.e., increased corrosion activity) and the increased anodic current density (i.e., increased corrosion rate). Moreover, the stress distribution at the dent area is consistent with the distributions of the corrosion potential and anodic current density. Specifically, a high stress area is associated with a negative corrosion potential and a great anodic current density.

For assessment of corrosion in dent, the important affecting factor for both local stress and corrosion is the dent depth, while the internal pressure has a limited effect on the anodic current density. In both the circumferential and longitudinal directions at the dent, as the dent depth increases, the anodic current density increases remarkably. Moreover, a deep dent can generate a big area to be affected by the dent in both stress and corrosion. The maximum anodic current density at the dent center is about 2.5–3 times of the anodic current density at the dent sides, showing an accelerated corrosion. The net current density and corrosion potential analyses confirm that the cathodic reaction area mainly locates at the sides of the dent and anodic reaction occurs at

the dent center. The main influence of the scenario is that the dent center suffers from accelerated corrosion, while the sides of the dent are under cathodic protection. The final consequence is that, as the corrosion grows at the dent, the pipeline will leak at the central site of the dent. The stress enhanced corrosion at the dent in will sever as a reliable foundation to estimate the corrosion growth and predict remaining service life of the pipelines.

In addition to the dent depth, the dent size is modeled to investigate its effect on local stress and anodic current density. Generally, a smaller dent, i.e., a small open diameter at the dent mouth, can cause a greater local deformation when the dent depth is identical. For smaller dents, the local stress concentration at the dents is much greater than bigger dents, and so is the maximum anodic current density. The net current density is greater in the longitudinal direction than the circumferential direction, indicating the more rapid corrosion growth in the longitudinal direction of the dent.

5.5 Conclusions

A new approach is developed to assess corrosion in dent on pipelines by considering both the mechanical and electrochemical corrosion factors and their interaction at an unconstrained dent through FE modeling of the denting, spring-back and pressurizing processes. The stress concentration at the dent accelerates corrosion due to a mechano-electrochemical interaction, where the dent depth is the critical affecting factor. As the dent depth increases, the local stress concentration is enhanced, resulting in increased corrosion activity and corrosion rate, as indicated by the negative shift in corrosion potential and increased anodic current density, respectively. The most negative corrosion potential and the maximum anodic current are located at the center of the dent, where the anodic reaction occurs. The cathodic reaction mainly occurs at the dent sides. The

internal pressure has a marginal effect on the anodic current density. A dent with a smaller open diameter can cause more remarkable local stress concentration and a greater anodic current density. Thus, at specific dent depths (e.g., h_0<30 mm), small dents tend to accelerate local corrosion at a more rapid speed than bigger dents. There is a more rapid corrosion growth in the longitudinal direction than the circumferential direction of the dent.

Chapter Six: Finite element modeling of the distribution of hydrogen atoms at a dent on pipelines for hydrogen transport under cyclic loading[**]

6.1 Introduction

Hydrogen embrittlement of the steel is a key problem must be addressed before the application of pipeline transporting hydrogen gas. Employing existing pipelines containing dent defect enhances the complexity of the HE analysis. To fill the gap, the originality of the work in this chapter is to determine the H atom diffusion at a dent on a full-scale steel pipe under cyclic loading, and to understand the effect of cyclic stress on H atom distribution at the dent on pipelines when transporting high-pressure hydrogen gas.

In this work, a 3-D FE based model was developed to define the stress/strain concentrations and determine the H atom diffusion and distribution at an unconstrained dent on an X52 steel pipe under cyclic loading of various magnitudes. The H atom diffusion was calculated with classic diffusion equations, while considering the synergistic effect of stress and concentration gradients. The denting and spring-back processes were modeled with various dent depths and indenter sizes. The H atom concentrations in both lattice sites and dislocations at the dent area were considered. It is expected that the research will serve as a base to evaluate the hydrogen-fatigue interaction when repurposing existing pipelines containing surface defects such as dents for hydrogen transport.

[**] The work in this chapter has been published as:

Jian Zhao, Y. Frank Cheng, Finite element modeling of the distribution of hydrogen atoms at a dent on pipelines for hydrogen transport under cyclic loading, *International Journal of Fracture*, (2023). https://doi.org/10.1007/s10704-023-00741-8

6.2 Methodology

6.2.1 Theoretical aspect of H atom diffusion in steels

The lattice H atom concentration, C_L, is written as:

$$C_L = N_L \theta_L \tag{6.1}$$

where N_L and θ_L are density of lattice sites to host H atoms and lattice sites occupancy, respectively. For body-centered cubic (BCC) metals such as X52 pipeline steel, N_L can be calculated by:

$$N_L = \beta_L N_A \rho_m / M_m = 5.1\times10^{29}[\text{sites/m}^3] \tag{6.2}$$

where β_L is the capacity number of lattice sites hosting H atoms (for BCC iron, β_L=6), N_A is Avogadro's number (i.e., 6.023×10^{23} atoms/mol), ρ_M is density of iron (i.e., 7.87×10^3 kg/m^3), and M_m is atomic weight of iron (i.e., 55.8×10^{-3} kg/mol).

In addition to the lattice sites, H atoms can become trapped at various metallurgical traps. The H atom concentration in the traps is calculated by [182]:

$$C_T^{\,n} = \theta_T^{\,n} N_T^{\,n} \tag{6.3}$$

where the superscript *n* refers to the type of traps (e.g., dislocations or grain boundaries), θ_T is trap occupancy, and N_T is number of trapping sites per unit volume (i.e., the density of trap sites). Generally, diffusible H atoms in steels are the major reason for HE occurrence [68]. As a result,

the lattice sites and reversible traps are mainly considered in this work. Since the density of specific traps keeps constant during plastic deformation except dislocations [31], the H atom concentration at dislocations is the main target of this work. Dislocation multiplication is usually induced by plastic deformation.

According to Oriani's equilibrium theory [183], the H atom concentration at traps (i.e., dislocations), C_T, is written as:

$$C_T = K^d C_L N_T^d \Big/ \left(N_L + C_L K^d \right) \tag{6.4}$$

where the superscript d refers to dislocations, and K^d is equilibrium constant that is calculated using the binding energy of dislocations (W_B^d) as:

$$K^d = \exp\left(-W_B^d \Big/ RT \right) \tag{6.5}$$

where W_B^d is determined as -25 kJ/mol [63], T is temperature, and R is universal gas constant (8.314 J/mol K). It is noted that Eq. (6.4) is used for estimation of the H atom concentration in dislocations. For other light elements such as nitrogen, the diffusion mainly occurs in interstitial voids of the crystalline lattice and grain boundaries. Therefore, the equation is only applied to H atom diffusion.

The total H atom concentration, C, in the steel is:

$$C = C_L + C_T \tag{6.6}$$

According to the chemical potential under the effect of hydrostatic stress, σ_H, the hydrogen flux, J, can be expressed as a function of the lattice H atom concentration by:

$$J = -D_L \frac{C_L}{1-\theta_L}\left(\frac{\nabla C_L}{C_L} - \frac{\nabla N_L}{N_L}\right) + \frac{D_L}{RT} C_L V_H \nabla \sigma_H \tag{6.7}$$

where D_L is the lattice H diffusion coefficient (i.e., 1.27×10^{-8} m^2/s when T=300 K) [184], and V_H is partial molar volume of H in solid solution (i.e., 2×10^{-6} m^3/mol). It should be noted that Eq. (6.7) is derived based on the assumption that the mobility of H atoms between trapping sites is negligible considering discontinuity of the traps [185]. Therefore, only the lattice flux is considered for H atom diffusion in this work. Since the lattice site density N_L is constant (i.e., ∇N_L=0) and a low occupancy of lattice sites in BCC iron (i.e., $\theta_L \ll 1$), Eq. (6.7) can be rewritten as:

$$J = -D_L \nabla C_L + \frac{D_L}{RT} C_L V_H \nabla \sigma_H \tag{6.8}$$

The mechanical factors affecting the H atom diffusion in steels include the hydrostatic stress gradient and the hardening effect during plastic deformation. According to Taylor's model [125], the shear flow stress influences the dislocation density. The dislocation density under plastic flow is calculated by the following equations which is applicable for metals in general:

$$\tau = 0.5Gb\sqrt{\rho} \tag{6.9}$$

where τ is shear flow stress, G is shear modulus, b is Burgers vector of dislocations, and ρ is density of dislocations. Statistically stored dislocations (SSD) and geometrically necessary dislocations (GND) are two types of dislocations in steels during work hardening. The GND density is caused by geometrical constraint of the crystalline lattice and affected by the internal strain gradient, which is in the scale of a few microns [125]. In this work, only the SSD density is considered. Based on Taylor's model, the tensile flow stress, σ_f, is:

$$\sigma_f = M_T \tau \tag{6.10}$$

where M_T is Taylor factor (for BCC metals, M_T=2.9). σ_f can be replaced with hardening function of the steels [125]. The SSD density is rewritten as:

$$\rho = \left(\frac{\sigma_f}{0.5 M_T G b} \right)^2 \tag{6.11}$$

Thus, ρ can be estimated when the stress-strain relationship of the steels is known. The relationship between the dislocation density and the H trapping site density is then written as:

$$N_T^d = \rho / b \tag{6.12}$$

For BCC metals [186],

$$b = \sqrt{3}a/2 \text{ and } N_T^d = 2\rho \Big/ \left(\sqrt{3}a \right) \tag{6.13}$$

where a is cubic edge length (i.e., 0.2867 nm for iron) [187]. It is noted that, in some literature [31, 125, 188], the trapping site density, N_T^d, was calculated using the formula for face-centered cubic (FCC) metals, which is not applicable for pipeline steels.

6.2.2 Mass diffusion of H atoms in COMSOL modeling

This work was conducted using COMSOL 6.0. The general formula governing diffusion of H atoms in COMSOL is provided as:

$$\frac{\partial C}{\partial t} + \nabla \cdot J = R_a \tag{6.14}$$

where C=C_L+C_T. The H atom flux J can be determined by Eq. (6.8). The H atom concentration in trap sites, C_T, can be solved using Eq. (6.4). R_a is a reaction term. Eq. (6.14) is thus written as:

$$\frac{dC_L}{dt} + \frac{dC_T}{dt} = D\nabla^2 C_L - \frac{D\bar{V}_H}{RT}\nabla\left(C_L \sigma_H\right) \tag{6.15}$$

In this work, only dislocations were considered as the hydrogen traps in the steel. By solving Eq. (6.15), the H atom concentrations in lattice sites and dislocations can be obtained. Three modules, i.e., transport of diluted species, solid mechanics, and the general form PDE, were used to solve Eq. (6.15) for modeling of H atom diffusion in the steel pipe containing a dent. The initial governing function, i.e., Eq. (6.14), was solved by the module of transport of diluted species. The reaction term, R_a, was related to the gradients of H atom concentration in lattice sites and of

hydrostatic stress, which were solved by the other two modules. In addition, the first derivative of H atom concentration in dislocations over time, dC_T/dt, was defined using the ‘‘Variables’’ node.

6.2.3 Analysis of the multi-physics field coupling effect

Three steps were contained in FE modeling in this work, i.e., denting, loading of internal pressure and H atom diffusion. As described in Chapter Three, for denting to create a dent on X52 steel pipe body, a spherical rigid indenter with a constant diameter of 100 mm was applied on a quarter pipe segment model, as shown in Fig. 6.1 (a). The initial denting depth, h_o, varied from 10 to 67 mm. An unconstrained dent was studied in this work and, therefore, a spring-back phenomenon was observed after removal of the indenter. Geometric dimensions and material properties are listed in Table 6.1, where the length of the pipe segment, L_1, is 4000 mm which is sufficient to avoid the effect of boundary conditions on the dent area. The pipe segment model was meshed with 3-D hexahedron elements, and the element size was distributed properly from the dent area to the pipe, as shown in Fig. 6.1 (b). The element size in the dent area was refined to ensure modeling accuracy. The bottom boundary of the pipe segment was fixed during the denting process and the cross sections were subject to symmetrical constraints, as marked ‘‘s’’ in Fig. 6.1. Varied downward displacements were applied on the indenter to create dents with various depths. A contact pair was assigned to the outer surfaces of the indenter and the pipe segment. When the spring-back was completed, a cyclic loading simulating pressure fluctuations was applied on the pipe interior. Simulation of this work was operated in solid mechanics and transport of diluted species fields, using a MUMPS solution solver. The modeling was completed using a high-performance workstation, and the multicore and cluster computing was configured to ensure robustness.

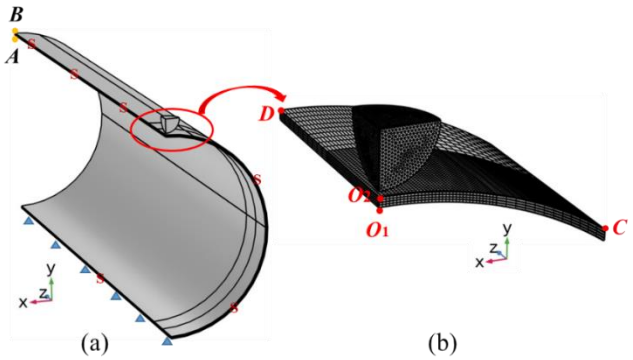

Figure 6.1 The 3-D FE model developed in this chapter (a) A quarter model of the pipe segment and the indenter, (b) Mesh of the dent area.

Table 6.1 Geometric dimensions and material properties used in this chapter.

Parameter	Value
Steel grade	API 5L X52
Outer pipe diameter, D_o	720 mm
Pipe wall thickness, t	8.1 mm
Length of pipe segment, L_1	4,000 mm
Elastic modulus, E	208 GPa
Shear modulus, G	80 GPa
Poisson's ratio, υ	0.3
Yield strength, σ_y	375 MPa
Ultimate tensile strength, σ_U	468 MPa
Temperature, T	300 K
Lattice diffusivity, D_L	1.27×10^{-2} mm^2/s

Identical material model in Chapter Three is used in this work and stress-strain curve is shown in Fig. 3.1. Experimental testing and modeling conducted by [189-192] detailed the processes of applying cyclic loading on a dented pipeline, where three to six cycles of internal pressure were applied on the pipe. A fatigue assessment was then performed. In this work, a cyclic stress simulating pressure fluctuations of pipelines was used, with an amplitude from 20% to 80% of maximum operating pressure (MOP). The MOP of X52 steel pipelines was estimated as 10.53 MPa [193]. Thus, the internal pressure fluctuates from 2 MPa to 8 MPa, and is then back to 2 MPa, which is defined as one cycle, as seen in Fig. 6.2. According to mechanics of steels, a linear stress-strain behavior was obtained during unloading after the applied stress exceeded yield strength. Thus, after spring-back and the first cycle of pressurizing, a similar stress-strain behavior was expected for the following cycles of pressure fluctuation with an identical amplitude [192].

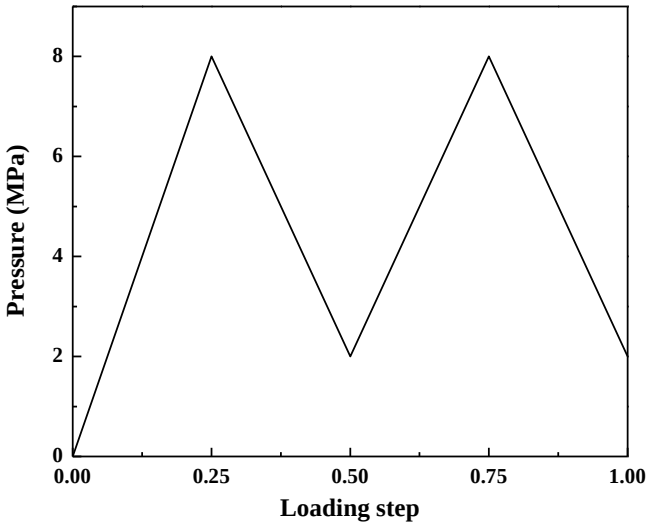

Figure 6.2 Cyclic pressure applied on the pipe interior (two cycles).

The complexity of H atom diffusion in pipeline steels is caused by multiple factors such as the strain hardening effect, stress and strain distributions and cyclic loading. Compared with two-

dimensional FE models in literature, it is not possible to simulate the cyclic loading accompanying with mass diffusion during a long time up to 2×10^6 s using a full-scale model. Therefore, the cyclic loading and the H atom diffusion were modeled separately in this work. The modeling program included three analysis steps, i.e., creation of a dent, cyclic loading by applying fluctuating internal pressures to the pipe interior, and H atom diffusion.

An initial H atom concentration on the internal surface of the pipe was set to simulate the H atom diffusion in pipe steel under the stress-strain field resulting from the cyclic loading using the developed mass diffusion module. Ratios of 1% to 20% of hydrogen gas blending with natural gas are mostly used in today's industry [60, 62, 194, 195]. In this work, the 10% hydrogen blending ratio was selected for simplification purpose. The partial pressure of hydrogen gas ranged from 0.04 MPa to 0.16 MPa considering the pressure fluctuations. Based on existing work, methane does not influence the diffusion of H atoms [186, 196]. The H atom dissolution in metals during the gaseous hydrogen permeation follows the Sievert's law [197, 198], where the initial H atom concentration C_0 on the inner pipe surface can be calculated by:

$$C_0 = S_{\mathrm{H}} \times \sqrt{P_{\mathrm{H}}} \tag{6.16}$$

where S_{H} is Sievert constant, and P_{H} is the partial pressure of hydrogen gas. For X52 pipeline steel, S_{H}=0.029 wppm/bar$^{1/2}$ as measured by hydrogen permeation tests [199]. Therefore, C_0 is calculated as 0.041 wppm to 0.082 wppm (i.e., 0.323 mol/m^3 to 0.646 mol/m^3 for H atoms in steels) under given partial pressures of hydrogen. The time dependent H atom diffusion and distribution were studied until a saturation condition was reached. In terms of the hydrogen flux on the outer surface of the pipe, the hydrogen permeation flux was negligible for steels, e.g., 8.12×10^{-10} mol H/m^2 s for

X80 steel [196]. Accordingly, the internal surface of the pipe was defined as the H atom source and the external surface was not associated with hydrogen flux. This is consistent with conditions reported previously [200-202].

6.3 Results

6.3.1 Element size analysis for FE modeling

Element size used in FE modeling affects the accuracy and computational efficiency. In this work, the stress and strain concentrations and H atom distribution mainly occur at the dent area. Refinement of grids should be conducted in the defect area and relatively coarse meshes can be applied in other areas of the pipe. The maximum and minimum element size of the pipeline model were 10 mm and 3 mm, respectively, and the number of domain elements was 90,390. After creation of the dent, two cycles of internal pressure were loaded and the von Mises stress at the dent on the inner surface of the pipe, i.e., point O_1 in Fig. 6.1 (b), was compared. The H atom distribution was analyzed considering the mechanical effect until the H atom concentration reached steady. The total H atom concentration C on the outer surface at the dent center, i.e., point O_2 in Fig. 6.1 (b), was then calculated and compared with different element sizes. Fig. 6.3 shows the von Mises stress and H atom concentration as a function of the element size when the initial dent depth h_o is 40 mm. It is seen that both the von Mises stress and the H atom concentration tend to become stable when the element numbers reach 90,390.

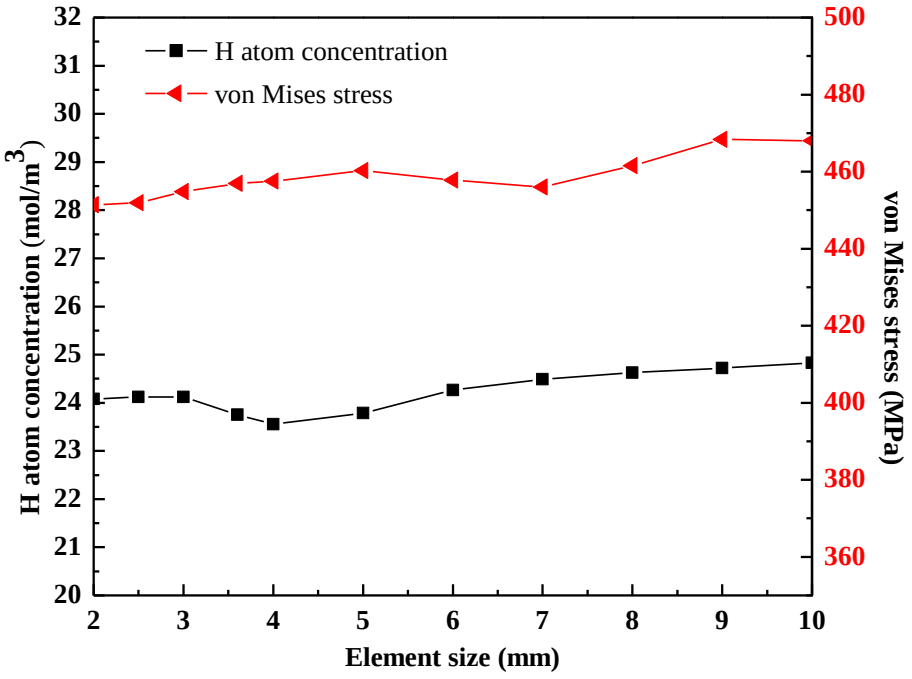

Figure 6.3 Mesh sensitivity analysis for FE modeling based on analysis of von Mises stress and H atom concentration after two cycles pressure loading (h_o=40 mm).

6.3.2 Reliability of the FE model

The FE modeling conducted in this work included mechanical stress/strain and H atom distributions at the dent area. The accuracy of the stress analysis can be validated by previous numerical results in Chapter Three. For H atom distribution, when the steel is under elastic deformation, the chemical potential, μ, at different sites on the pipe segment can be calculated by [202]:

$$\mu=\mu_0+RT\ln C_L-\sigma_h V_H \tag{6.17}$$

where μ_0 is chemical potential under standard conditions. As shown in Fig. 6.1 (a), points A and B are at the end of the pipe segment, where plastic strain does not exist upon application of cyclic

loading. Point A is on the inner surface, which has a constant H atom concentration, C_0, and point B is on the outer surface. The chemical potential of the cross section of the pipe should be identical when an equilibrium state is reached, i.e., $\mu_A=\mu_B$. Hydrostatic stresses of points A and B can be obtained from mechanical analysis, which are 29.59 MPa and 27.56 MPa, respectively, under an internal pressure of 2 MPa. Based on the theoretical calculation by Eq. (6.17), the lattice H atom concentration at point B is 0.322 mol/m^3. The FE modeling of the H atom distribution shows that the H atom concentration at this point is 0.323 mol/m^3. A very small error exists between the calculation by Eq. (6.17) and the FE modeling.

6.3.3 Modeling of stress and strain distributions at the dent area

Hydrogen atom diffusion in pipeline steels is remarkably affected by plastic deformation and the stress status of the steels. The von Mises stress and equivalent plastic strain distributions at the dent area after each of the three processes, i.e., denting, spring-back and cyclic loading, are shown in Fig. 6.4. When the indenter goes to the deepest position (i.e., h_o=40 mm), the von Mises stress (σ_e) at the dent center reaches the maximum value of 468 MPa, and the equivalent plastic strain (ε_p) is 0.262. After the indenter is removed, the maximum σ_e deviates from the dent center while the maximum ε_p is still located at the dent center and maintains at 0.262. Upon application of the cyclic loading, the stress concentration zone further deviates from the dent center and shifts towards the dent side along the circumferential direction, which is consistent with reported results [191, 192, 203]. Higher levels of equivalent stress and plastic strain are found on the internal surface of the pipe than the outer surface. Furthermore, the maximum von Mises stress deviates from the dent center during the three processes.

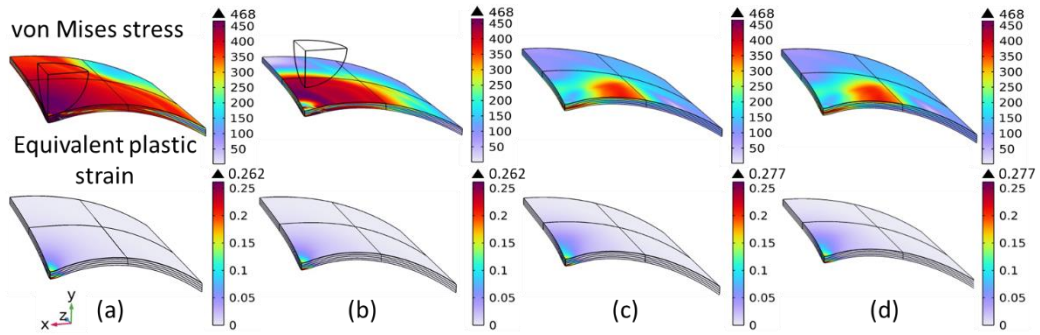

Figure 6.4 The von Mises stress and plastic strain distributions at the dent area after (a) denting (h_o=40 mm), (b) spring-back, (c) cyclic loading by the end of the first pressurizing cycle, (d) cyclic loading after the end of the second pressurizing cycle.

The values of von Mises stress and equivalent plastic strain at the dent center during denting, spring-back and cyclic loading are shown in Fig. 6.5, where superscripts *i* and *o* refer to the modeling results on the inner and outer surfaces, respectively. During denting, the von Mises stress on the internal surface at the dent center reaches a maximum value of 468 MPa at 10 mm in depth, and maintains the value until the maximum depth of 40 mm. However, the maximum von Mises stress on the outer surface decreases after the dent depth exceeds 20 mm. By the end of spring-back, the von Mises stresses on the inner and outer surfaces at the dent center decrease to 379 MPa and 237 MPa, respectively. Upon application of the cyclic loading, both von Mises stresses, i.e., σ_e^i and σ_e^o, show a similar fluctuating pattern. Comparing with the denting and spring-back processes, a remarkable decrease in von Mises stress happens at the end of the loading cycle. This confirms that the stress concentration at the dent center can be relieved by pressure fluctuations.

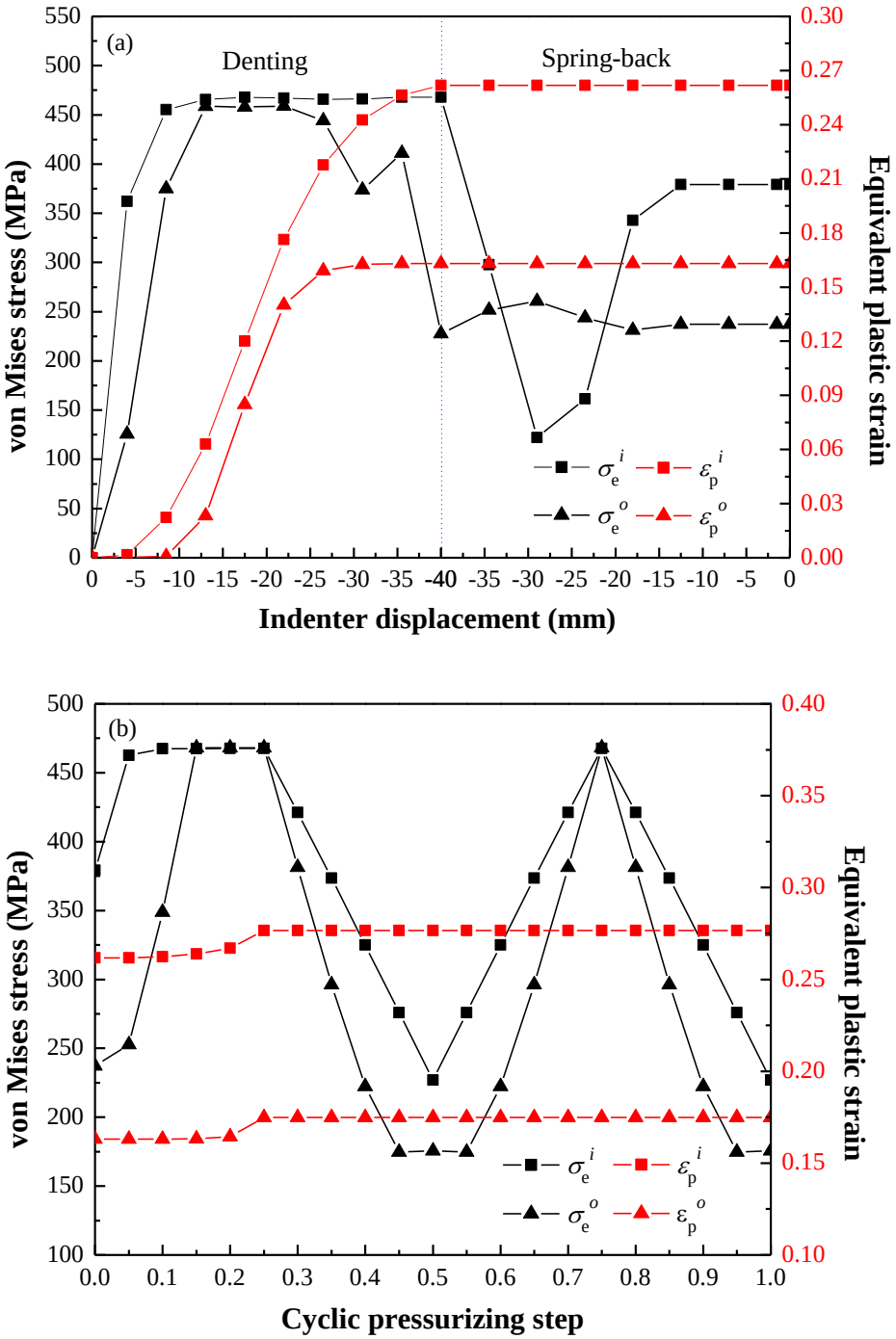

Figure 6.5 The values of von Mises stress (σ_e) and equivalent plastic strain (ε_p) at the dent center during (a) denting for 40 mm and spring-back, where the negative displacement indicates downward motion of the indenter, and (b) cyclic loading.

Different from the change of von Mises stress, the equivalent plastic strain at the dent center is relatively stable during spring-back and cyclic loading. The plastic strains reach the maximum values by the end of denting and keep constant during the spring-back at 0.26 and 0.16 on the inner and outer surfaces, respectively. When the internal pressure increases to 8 MPa, the plastic strains are 0.28 and 0.18 for internal $\varepsilon_p{}^i$ and outer $\varepsilon_p{}^o$ surfaces, respectively. The relative stability of the plastic strain at the dent center is attributed to an increased elastic limitation (i.e., hardening) of the steel by a large plastic deformation caused by denting.

By the end of cyclic loading, the von Mises stress and equivalent plastic strain distributions in the circumferential (i.e., O_2C direction in Fig. 6.1 (b)) and longitudinal (i.e., O_2D direction in Fig. 6.1 (b)) directions are shown in Fig. 6.6, where an internal pressure of 2 MPa is maintained inside the pipe. The maximum von Mises stress of 378.33 MPa occurs at a circumferential distance of 74.09 mm from the dent center. At any other locations in both the circumferential and longitudinal directions on the outer surface, the von Mises stress is smaller than yield strength of the steel. For the plastic strain distribution on the outer surface at the dent area, the maximum value is 0.19 in both the circumferential and longitudinal directions, which deviates 2.98 mm and 2.73 mm from the dent center.

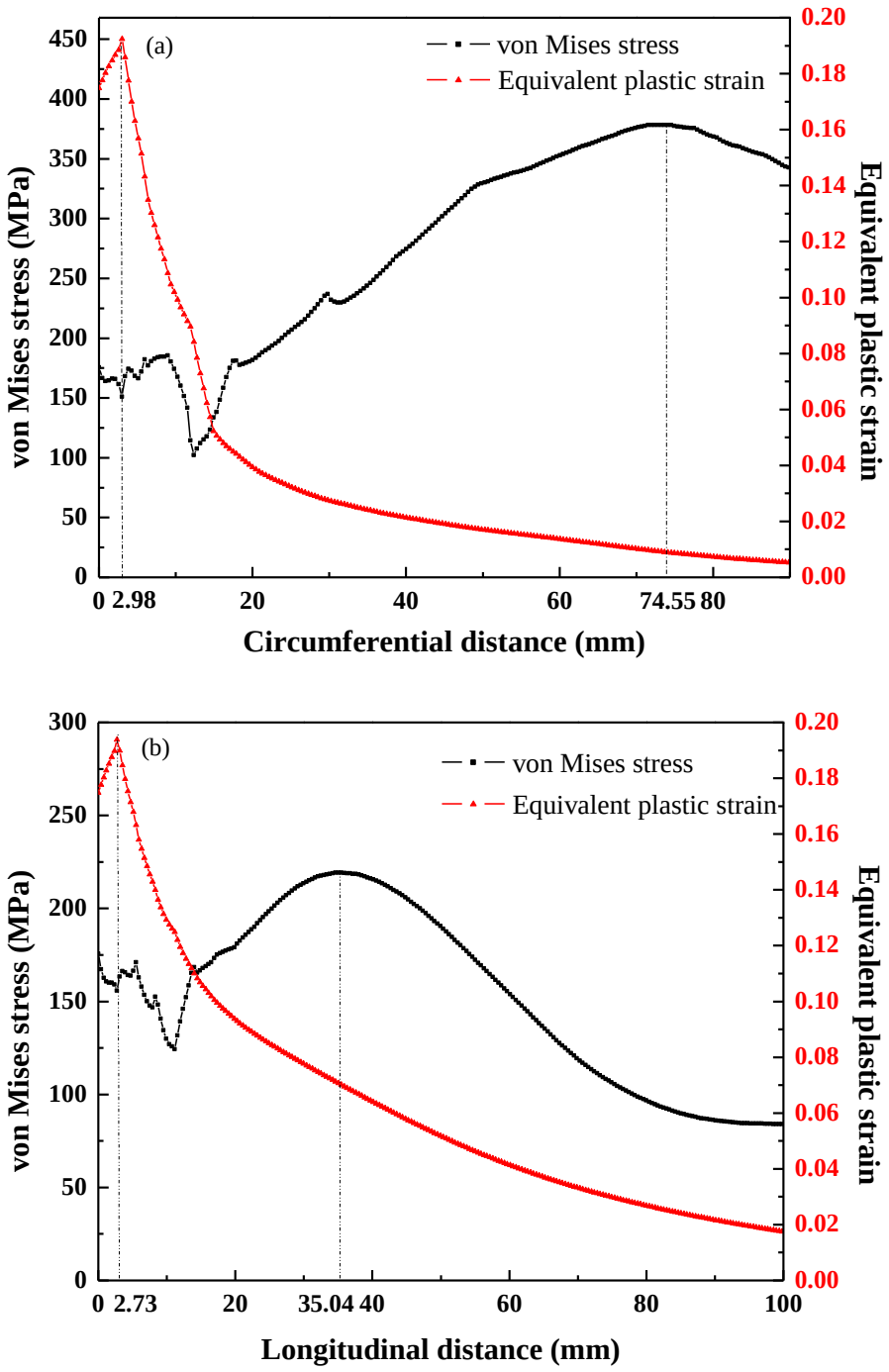

Figure 6.6 The von Mises stress and plastic strain distributions in the (a) longitudinal and (b) circumferential directions at the end of cyclic loading (h_o=40 mm).

6.3.4 Modeling of H atom distribution at the dent

The factors affecting diffusion and distribution of H atoms in steels mainly include the gradient of hydrostatic stress, σ_H, and the density of dislocations, N_T^d. After denting and cyclic loading processes, H atoms diffuse from the inner surface to the outer surface of the pipe and reach saturation finally. The typical H atom diffusion curve on the outer surface at the dent center (i.e., O_2 in Fig. 6.1 (b)) with 40 mm in depth is shown in Fig. 6.7, where both the total and lattice H atom concentration (C and C_L) curves are present. The initial H atom concentration on the inner pipe surface was set as 0.323 mol/m^3. It is seen that both the total and lattice H atom concentrations at the dent center reach equilibrium values after about 10,000 s. The steady values of C and C_L are 0.331 mol/m^3 and 0.315 mol/m^3, respectively. The difference between C and C_L is the H atom concentration in dislocations C_T. Obviously, most H atoms accumulate in the lattice sites (95% of C), rather than dislocations.

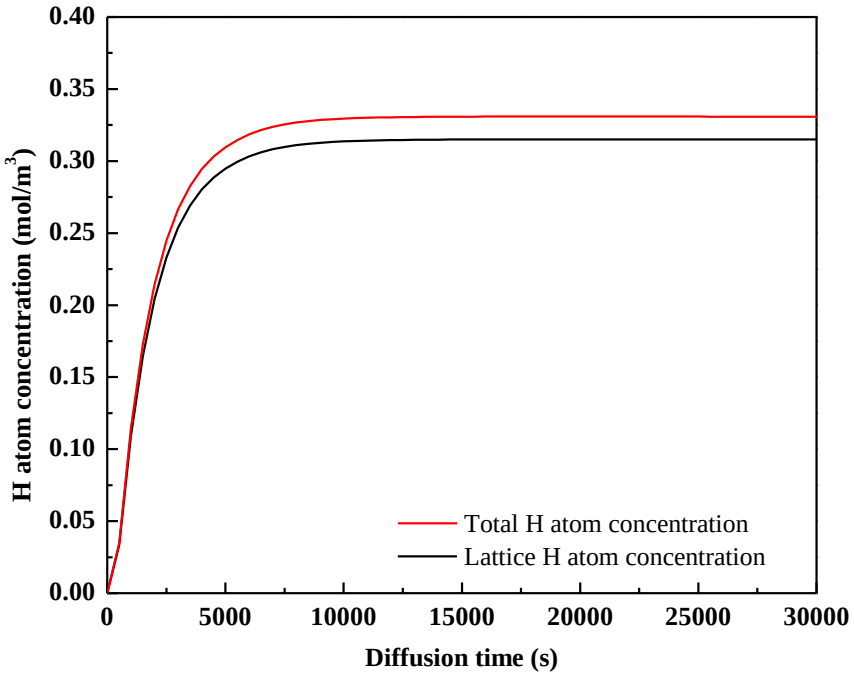

Figure 6.7 Total and lattice hydrogen atom concentrations on the outer surface at the dent center with a depth of 40 mm.

The distributions of total, lattice and dislocation H atom concentrations at the dent area with various dent depths are shown in Fig. 6.8. The pipe segment is exposed to hydrogen gas environment for a sufficient time until the H atoms reach equilibrium in the steel. The dislocation density is estimated by Taylor's model, i.e., Eqs. (6.9) ~ (6.13). Both C and C_L do not change apparently as the dent depth increases. Since the H atoms accumulating in the lattice sites are over 20 times than in dislocations, the total H atom concentration C mainly depends on C_L. However, the locations with the maximum C and C_L deviate from the dent center to the side in the circumferential direction with increased dent depth. Although the stress and strain of the dent can be strongly affected by dent depth, which further influences the H atom diffusion, there is little change for the maximum H atom concentration. The minimum H atom concentration decreases from 0.331 mol/m^3 to 0.279 mol/m^3, which is even smaller than the initial H atom concentration on the inner surface, when the dent depth increases from 10 mm to 60 mm. Theoretical calculations show that C_T is mainly determined by plastic strain and the H atoms concentrate around the dent center. When the dent depth exceeds 40 mm, a shift of C_T is observed, indicating that the maximum H atom concentration and the distribution in dislocations are also affected by the lattice H atom concentration when the dent is deep. A depth of 40 mm is defined as the threshold value distinguishing shallow and deep dents.

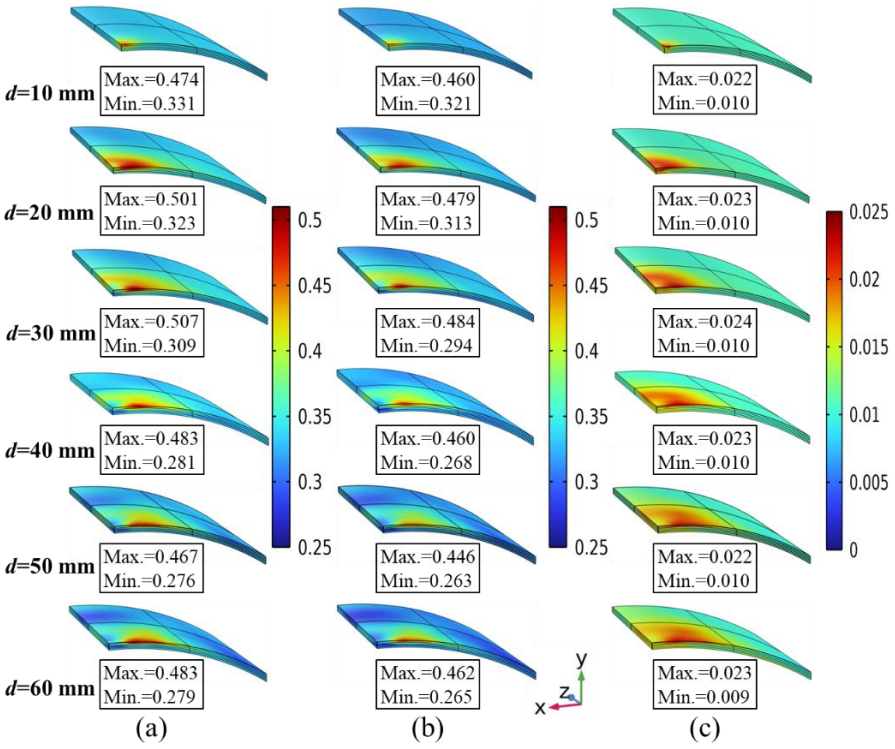

Figure 6.8 H atom concentration at the dent area (a) Total H atom concentration *C*, (b) lattice H atom concentration C_L, and (c) dislocation H atom concentration C_T.

6.3.5 Quantitative determination of H atom concentration at the dent area

It is seen from Fig. 6.8 that a big difference exists for H atom distribution between the circumferential and longitudinal directions as the dent depth changes. Three dent depths, i.e., 20 mm, 40 mm and 60 mm, were selected for a quantitative comparison of H atom concentrations as a function of the dent depth. The steady state H atom concentrations in the circumferential (i.e., O_2C in Fig. 6.1) and longitudinal (i.e., O_2D in Fig. 6.1) directions on the outer surface of the dent area are shown in Fig. 6.9. In both directions, there is a higher H atom concentration at the center of the dent of h_o=20 mm due to the higher σ_H as shown in Fig. 6.10. The H atom concentrations C and C_L decrease as the dent becomes deeper. The location with the maximum H atom concentration shifts away from the dent center with increased dent depth.

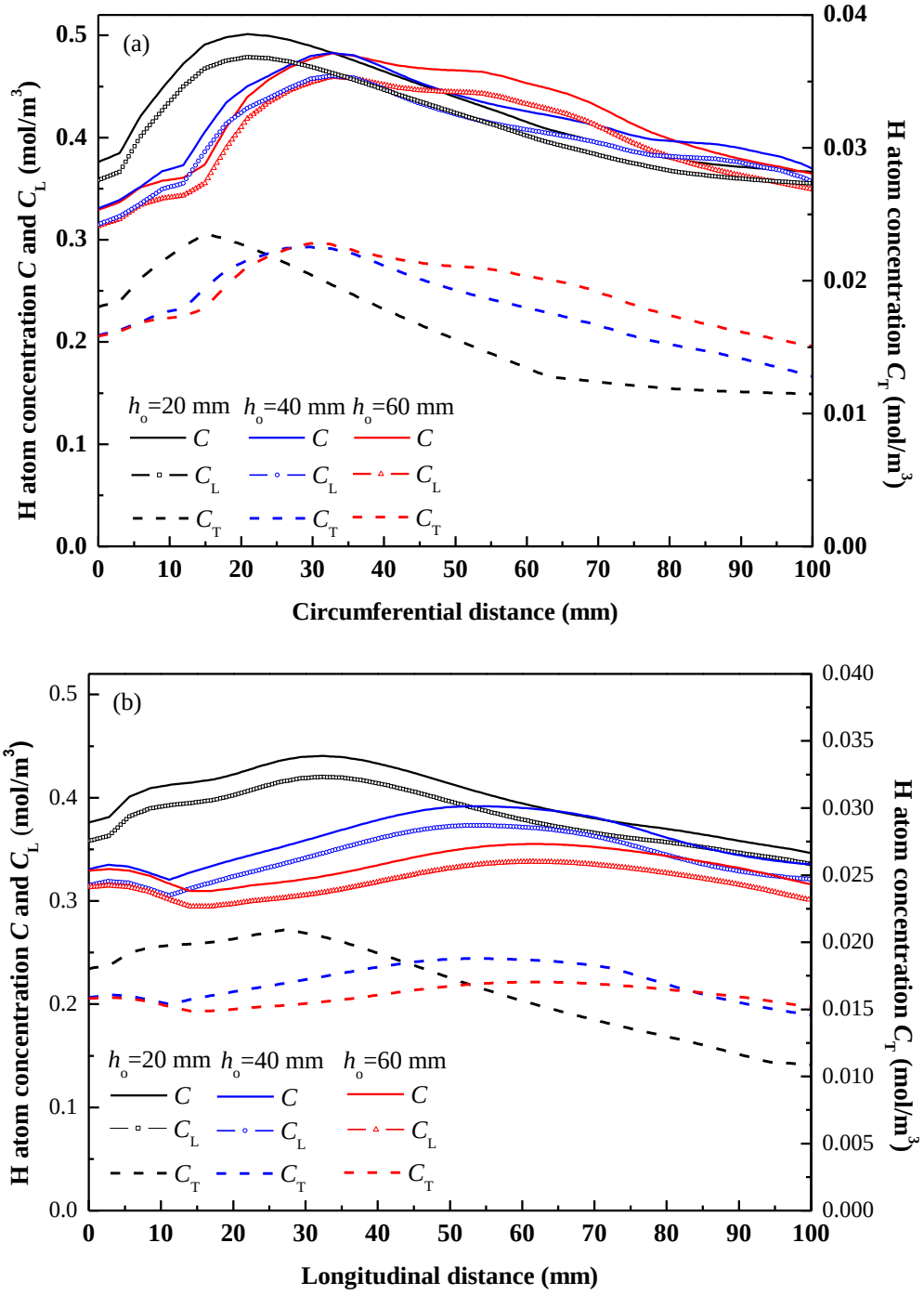

Figure 6.9 The steady state H atom concentrations in the (a) circumferential (i.e., O_2C in Fig. 6.1) and (b) longitudinal (i.e., O_2D in Fig. 6.1) directions on the outer surface of the dent area.

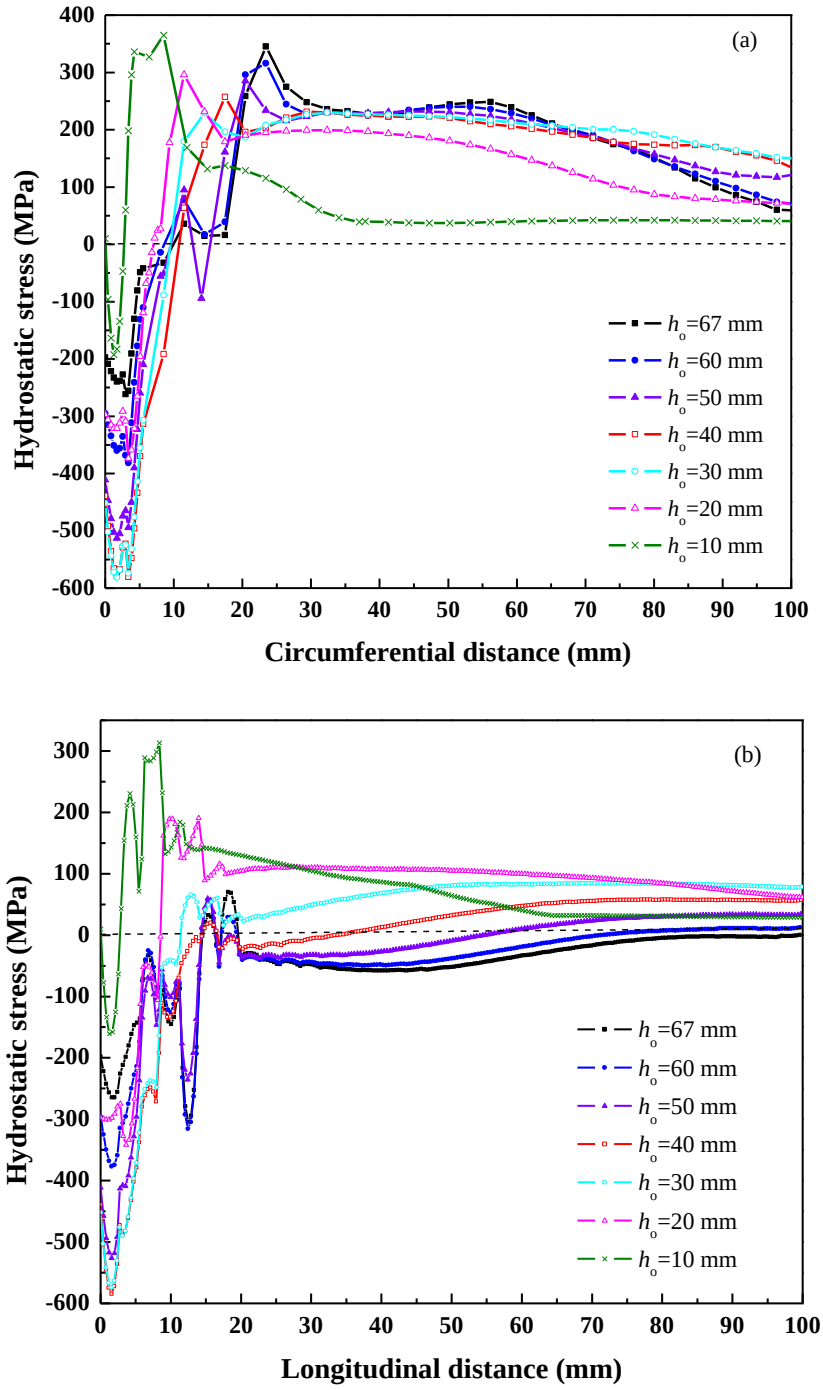

Figure 6.10 Distributions of hydrostatic stress, σ_H, at a dent with various dent depths in the (a) circumferential and (b) longitudinal directions.

The dent depth is a major factor affecting the mechanical stress at the dent. It is important to define the H atom concentration and distribution considering the von Mises stress at the dent with various depths. Table 6.2 lists the maximum H atom concentration as a function of the dent depth in the circumferential and longitudinal directions, where *s* refers to the shift distance of the maximum H atom centration from the dent center, the subscripts C and L denote the circumferential and longitudinal directions, respectively, and the superscripts H and σ denote the H atom concentration and the von Mises stress, respectively. Generally, the shift distances of s^{H} and s^{σ} increase as the dent depth increases in both circumferential and longitudinal directions. In the circumferential direction, the maximum H atom concentration is closer to the dent center than the maximum von Mises stress, which is different from the results obtained in the longitudinal direction. Thus, the H atom concentration in the circumferential direction of the dent area should be considered when determining the H atom diffusion. The s_C^{H} is always smaller than the indenter radius, indicating that the maximum H atom concentration is not located beyond the dent area. Furthermore, the difference between s^{H} and s^{σ} implies that the determination of H atom concentration should be conducted separately from the stress evaluation, especially for deep dents.

According to the solution of hydrogen diffusion in Eq. (6.15), one of the major factors affecting the H atom concentration is the hydrostatic stress of the pipeline. Fig. 6.10 shows the distributions of hydrostatic stress, σ_H, at a dent with various depths in the circumferential and longitudinal directions. As the dent depth decreases, the maximum hydrostatic stress shifts towards the dent center in both circumferential and longitudinal directions. The maximum σ_H decreases from 364.91 MPa (h_o=10 mm) to 229.84 MPa (h_o=30 mm) and then increases to 345.38 MPa (h_o=67 mm) in the circumferential direction. Similarly, the maximum σ_H occurs when the dent depth is 10 mm in the longitudinal direction. At the dent center, the hydrostatic stresses are

negative, decreasing first and then increasing as the dent depth increases. The minimum σ_H occurs at the dent with h_o=40 mm. It was reported that a positive hydrostatic stress could enhance the H atom concentration, while the negative stress was unfavorable for H atom accumulation [204]. Comparing the results in Figs. 6.9 and 6.10 and Table 6.2, it is found that the hydrostatic stress in the longitudinal direction is smaller than the stress in the circumferential direction, and the hydrostatic stresses at the dent center are negative. As a result, the H atom concentration in the longitudinal direction is lower than the concentration in the circumferential direction.

Table 6.2 The maximum H atom concentration at a dent of various depths in the circumferential and longitudinal directions.

h_o (mm)	Maximum H atom concentration in the circumferential direction				Maximum H atom concentration in the longitudinal direction			
	C (mol/m^3)	s_C^H (mm)	σ_e (MPa)	s_C^σ (mm)	C (mol/m^3)	s_L^H (mm)	σ_e (MPa)	s_L^σ (mm)
10	22.79	5.96	320.59	2.98	22.21	5.85	307.39	0
20	23.76	20.86	275.02	32.36	21.52	32.15	214.50	3.21
30	24.73	29.80	328.63	53.65	20.79	49.70	252.19	0
40	23.56	32.78	378.33	74.09	19.15	52.46	219.26	35.04
50	22.81	41.73	436.47	77.92	18.07	58.23	272.28	37.40
60	23.54	32.78	449.70	71.96	17.38	61.06	296.71	43.19
67	23.84	35.76	454.03	74.94	17.09	60.96	308.49	44.80

6.3.6 Effect of cyclic loading on stress/strain distribution and H atom concentration at the dent

Pressure fluctuations are commonly encountered in gas pipelines. In this work, the cyclic pressure shown in Fig. 6.2 was applied inside the pipe where a dent existed (40 mm in depth after the spring-back). The modeling results were compared with the dented pipe under a constant 2 MPa internal pressure. The distributions of von Mises stress and plastic strain on the outer surface of the dent with and without cyclic loading are shown in Fig. 6.11. It is seen that the von Mises stress is remarkably affected by the cyclic loading. In both the circumferential and longitudinal directions, the von Mises stress of the pipe under a constant pressure is much greater than the stress under cyclic pressurizing. For the pipe under constant pressure, there are stress fluctuations around the dent center and the maximum stress is up to the ultimate strength of the steel (i.e., 468 MPa). However, the stress level is reduced by the cyclic loading, and the location with the maximum stress concentration is farther away from the dent center. Although the equivalent plastic strains in both directions are relatively independent of the cyclic loading, the pipe upon cyclic loading has a slightly greater plastic strain. This is associated with the fact that a high pressure during cyclic loading can cause more plastic deformation.

The H atom distributions at the dent area on the pipe with and without cyclic loading in the circumferential and longitudinal directions are shown in Fig. 6.12. Obviously, there is a higher H atom concentration on the dented pipe under a constant pressure in both directions. In other words, cyclic loading due to pressure fluctuations lowers the H atom accumulation at the dent. The lattice H atom concentration under a constant pressure is greater due to the higher hydrostatic stress. The locations with the maximum H atom concentration are close in both directions as presented in Table 6.2. Although the stress and strain distributions at the dent area are different in the absence and presence of cyclic loading, the H atom distributions are quite similar.

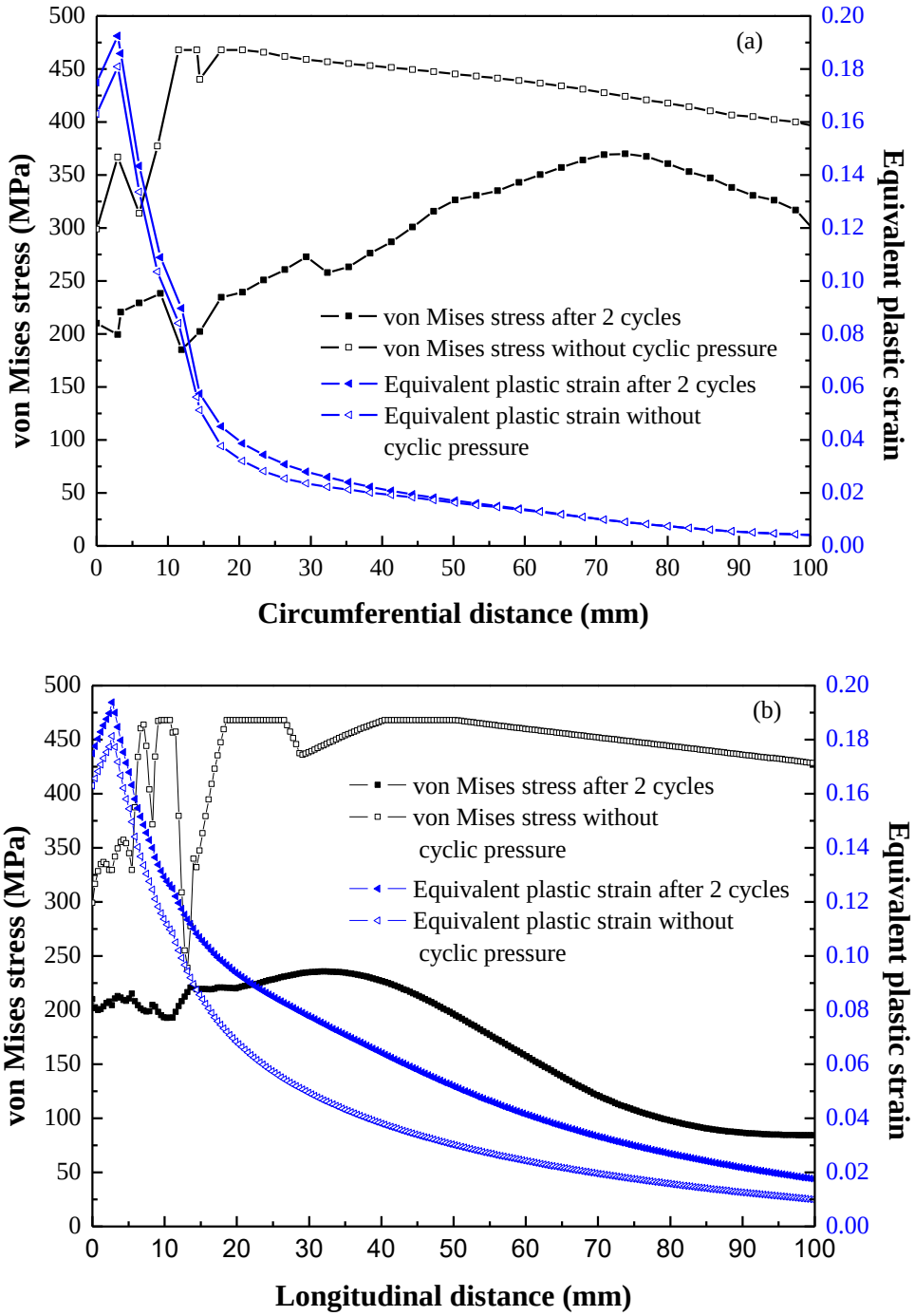

Figure 6.11 Distributions of von Mises stress and equivalent plastic strain on the outer surface of the dent (40 mm in depth) in the (a) circumferential and (b) longitudinal directions with and without cyclic loading.

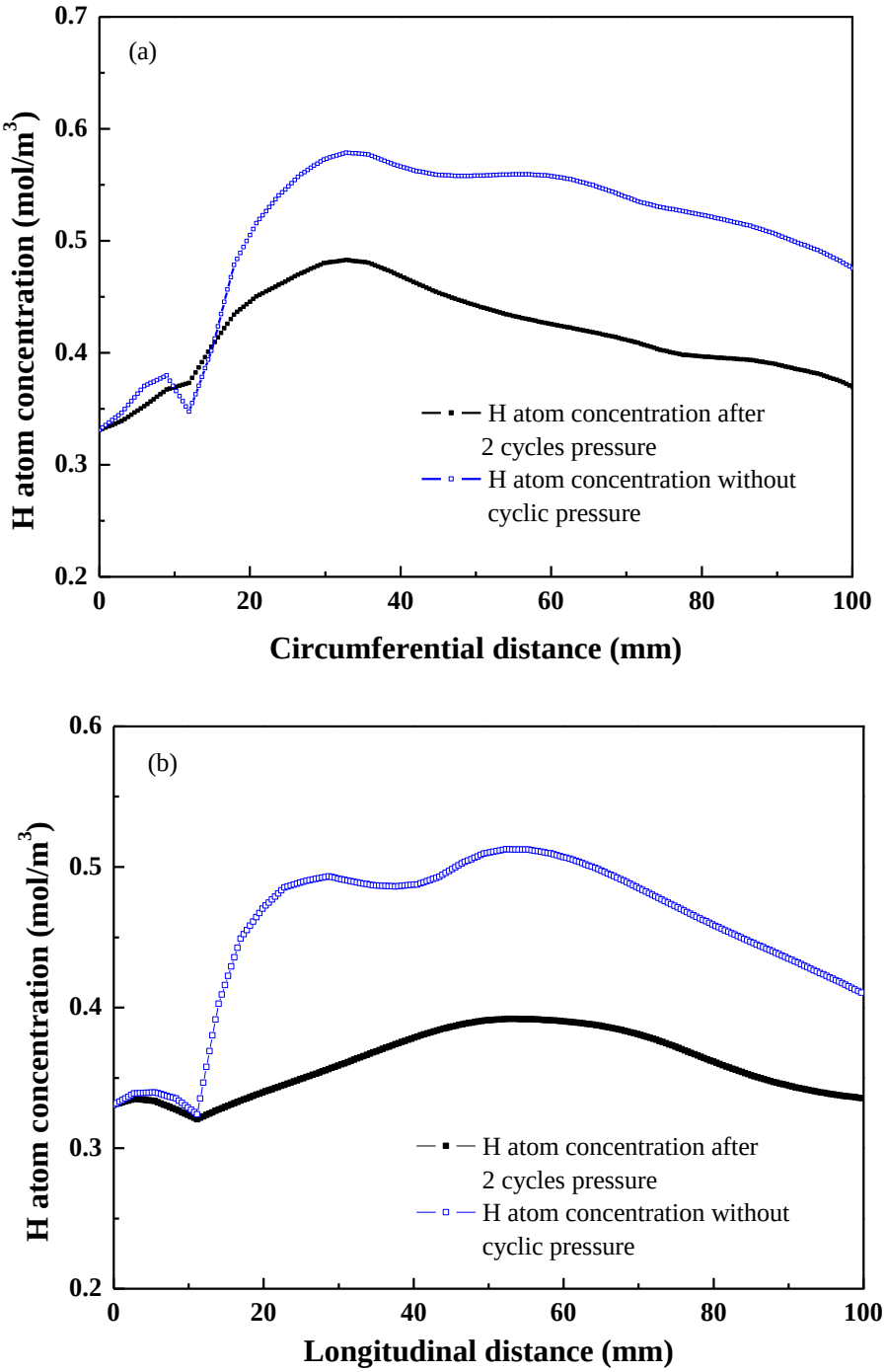

Figure 6.12 Total H atom concentrations at the dent area with and without cyclic loading in the (a) circumferential and (b) longitudinal directions when h_o=40 mm.

It should be noted that, although the internal pressure of pipelines fluctuates, the fluctuation range is usually smaller in practice than the range of 2-8 MPa modeled in this work. Generally, the internal pressure of pipelines usually fluctuates around the operating pressure [68]. The influence of internal pressure on H atom diffusion should be considered due to its significant effect on mechanical stress on the pipe. Therefore, a pressure of 8 MPa is kept after the cyclic loading and the modeling results were compared with the condition under an internal pressure of 2 MPa. Fig. 6.13 shows the hydrostatic stress, the total H atom concentration and the H atom concentration at dislocations under the internal pressures of 2 MPa and 8 MPa, respectively. The initial H atom concentration of 0.323 mol/m^3 was applied on the inner surface of the pipe, and the dent depth was 40 mm. It is seen that a higher internal pressure (i.e., 8 MPa) increases the hydrostatic stress and the total H atom concentration at the dent area. The σ_H around the dent center is more uniform than the hydrostatic stress under the 2 MPa internal pressure, where the stress is concentrated mainly in the circumferential direction. A similar pattern is also observed on the H atom concentration distribution. Thus, although the maximum C is located in the circumferential direction, an estimation of the H atom diffusion around the dent center is necessary. Moreover, the total H atom concentration increases from 0.481 mol/m^3 to 0.572 mol/m^3 when the internal pressure changes from 2 MPa to 8 MPa.

Considering the effect of numbers of cyclic loading, a similar H atom concentration distribution is found at the dent area after the first cycle of pressurizing, which is consistent with the experimental measurements [205]. This is attributed to the mechanical stress field at the dent area dominated by strain-hardening during denting, while the contribution of cyclic loading is modest. In addition, the effect of cyclic loading on the H atom distribution is also resulted from

increased dislocation density, but the dislocation density is relatively small based on Taylor's model calculations.

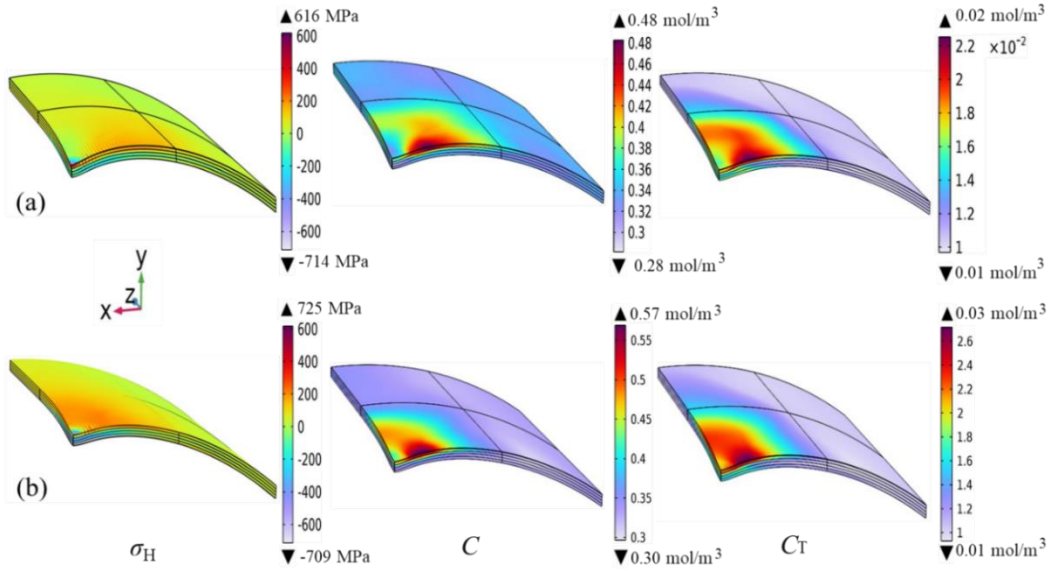

Figure 6.13 Hydrostatic stress, the total H atom concentration and the dislocation H atom concentration under the internal pressures of (a) 2 MPa and (b) 8 MPa with the initial H atom concentration 16.04 mol/m^3 applied on the inner surface and h_o=40 mm.

6.3.7 Effect of the indenter size on H atom concentration at the dent

A spheric indenter with diameter D_2 varying from 20 mm to 180 mm was applied on the pipe with relevant parameters listed in Table 6.1, and the dent depth was fixed at h_o=40 mm. The inner surface of the pipe had the initial H concentration C_0=0.323 mol/m^3 and was loaded with two cycles of pressure. Fig. 6.14 shows the H atom concentrations C and C_T and the equivalent plastic strain ε_e with various indenter size D_2. It is seen that smaller indenters produce sharper dents and a larger plastic deformation. However, the area with a high H atom concentration does not change as the indenter diameter increases. A similar phenomenon is also observed for the peak value of H

atom concentration. The maximum equivalent plastic strains are located at the inner dent center and decrease significantly when D_2 increases, confirming that the plastic deformation does not apparently influence the total H atom concentration. The maximum values of C, C_T and the H atom concentration are recorded at the dent side on the outer surface of the pipe. Compared with the dent depth, the indenter size does not affect the H atom concentration of the dented pipe.

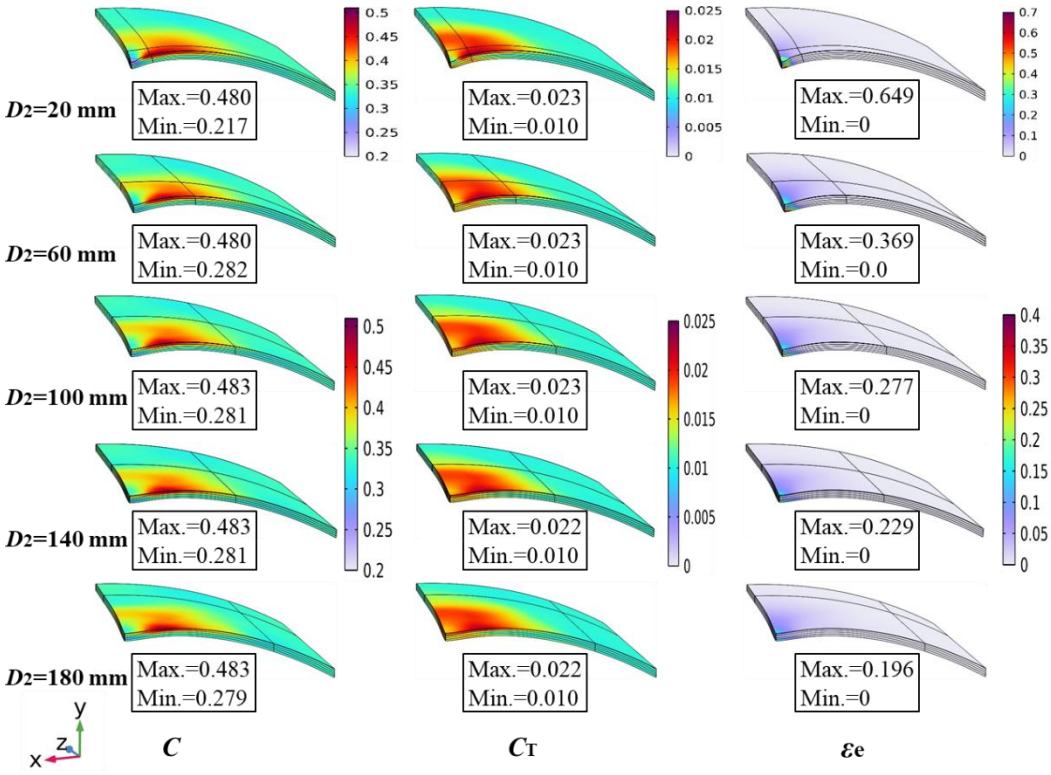

Figure 6.14 Effect of indenter size (D_2) on total H atom concentration (C), dislocation H atom concentration (C_T) and equivalent plastic strain (ε_e) after two cycles of loading with h_o=40 mm and C_0=0.323 mol/m^3. Note that the unit of H atom concentrations is mol/m^3 and contours have same geometrical size.

6.3.8 Implication on HE susceptibility of hydrogen pipelines under pressure fluctuations

This work applies to the realistic challenge to integrity of existing “aged” pipelines when repurposing for hydrogen transport while the pipelines experience pressure fluctuations. Although specific conditions are used for the investigation in the work, the obtained results are applicable as a reference for integrity evaluation of the pipelines. Denting and cyclic loading are introduced on the X52 steel pipe to produce mechanical conditions that affect the H atom diffusion and distribution in the steel, especially at the dent, and thus the HE susceptibility of the pipeline. An important finding of the work is that, while a high stress concentration occurs around the dent center after spring-back, the stress concentration zone shifts to the dent side along the circumferential direction upon cyclic loading. Thus, the conventional stress assessment conducted at the dent center will not apply for dent assessment if the gas pipelines are under pressure fluctuations. Instead, an accurate determination of the shifting distance of both the stress concentration and the H atom accumulation from the dent center is critical to assessment of the HE susceptibility of dented pipelines carrying hydrogen.

Furthermore, an assessment of the H atom distribution at a dent on pipelines should be conducted, especially in the circumferential direction of the dent, to estimate the local HE susceptibility. The results show that a cyclic loading resulted from pressure fluctuations can reduce the stress level at the dent area, as compared with the constant pressure. As a result, the local dislocation density could decrease, causing a reduced trapping of H atoms. This is beneficial in terms of the HE occurrence. Thus, the pressure fluctuation occurring on gas pipelines, including the pipelines transporting hydrogen in blended form, can decrease the local H atom accumulation and thus the risk to HE. The H atom concentration at dent center of the outer surface after pressurizing is less than the initial concentration and thus, the dent center has less risk to HE than

the dent edge. Analysis of various indenter sizes shows that the H atom concentration is slightly affected by the indenter diameter when other conditions of the dented pipelines remain identical.

6.4 Conclusions

A 3-D FE model is developed to determine the stress/strain distribution and calculate H atom concentration at an unconstrained dent on X52 steel pipe upon the denting, spring-back and cyclic loading processes. While a stress concentration generates at the dent center due to denting, the cyclic loading can shift the stress concentration zone to the dent side in the circumferential direction. Moreover, the stress concentration can be remarkably relieved by internal pressure fluctuations. The stress-strain analysis at the dent under cyclic loading should be conducted at the dent side, especially in the circumferential direction, rather than at the dent center. With an increased dent depth, the shift of the maximum H atom concentration from the dent center to the side in the circumferential direction further increases. The H atom distribution is dominated by the lattice H atoms, especially for deep dents with a depth more than 40 mm.

There are no certain relationships among the maximum H atom concentration, von Mises stress, hydrostatic stress, or plastic strain in terms of their distributions and quantities. The cyclic pressure reduces the von Mises stress at the dent and increases the plastic strain. More H atoms concentrate at the dent when the pipe is under a constant pressure than cyclic loading. When the internal pressure increases, the hydrostatic stress and the H atom concentration also increase.

Chapter Seven: Investigation of hydrogen induced cracking on dented pipelines using phase field method[††]

7.1 Introduction

Hydrogen induced cracking is the most severe damage to the steel structures especially for the pipelines transporting high-pressure hydrogen gas. As stated in Chapter Six, the FE method is valid for evaluating the H atom diffusion and distribution in the pipeline containing a plain dent defect. To further investigate the HIC initiation and propagation on the pipeline, a novel assessment framework for HIC of a dented pipeline was developed using the PF method. Theoretical bases for phase field fracture analysis and the H diffusion were introduced. Multiphysics FE models were developed under three conditions: denting, denting coupled with H atom diffusion and denting on a pipeline in service. Factors including the dent depth, H atom concentration and internal pressure were considered. The prediction of HIC occurrence was proposed, and the critical phase field parameter for crack initiation was determined. The initiation and propagation of cracking of hydrogen pipelines were assessed by the PF method.

7.2 Phase field analysis for hydrogen embrittlement of steel

7.2.1 Energetic formulation

As set forth in the introduction, PF fracture model is an energy-based fracture theory and thus, the strain energy declines with the increasing of the PF parameter, i.e., ϕ. The elastic-plastic body is considered to occupy an arbitrary space $\Omega \subset \mathbb{R}^n$ with an external boundary $\partial\Omega \subset \mathbb{R}^{n-1}$. Elastic

[††] The work in this chapter has been submitted as:

Jian Zhao, Y. Frank Cheng, Investigation of hydrogen induced cracking on dented pipelines using phase field method, *International Journal of Mechanical Science*, in submission.

plastic fracture of the pipeline steel is considered in this work and therefore, elastic strain energy, plastic strain energy and the fracture energy are included in the energy function. The total potential energy density W is the sum of strain energy density ψ and fracture energy density φ,

$$W\left(\boldsymbol{\varepsilon},\phi,\nabla\phi\right)=\psi\left(\boldsymbol{\varepsilon},g\left(\phi\right)\right)+\varphi\left(\phi,\nabla\phi\right) \tag{7.1}$$

where $\boldsymbol{\varepsilon}$ is the strain of the structure, g(ϕ) is the PF degradation function, and the damage field variable $\phi\in[0, 1]$. When ϕ=0, the material is intact and ϕ=1 indicates the completely fracture. Additive decomposition of the strain is applied and the elastic-plastic strain can be expressed as:

$$\boldsymbol{\varepsilon}=\boldsymbol{\varepsilon}_{\mathrm{e}}+\boldsymbol{\varepsilon}_{\mathrm{p}} \tag{7.2}$$

where the subscripts “e” and “p” indicate the elastic and plastic parts of the strain, respectively. The strain energy density can therefore be decomposed as the elastic and plastic parts,

$$\psi_0=\psi_{\mathrm{e}}\left(\boldsymbol{\varepsilon}_{\mathrm{e}}\right)+\psi_{\mathrm{p}}\left(\boldsymbol{\varepsilon}_{\mathrm{p}}\right) \tag{7.3}$$

in which the subscript “0” denotes the strain energy density without the degradation of cracking. It should be noted that no coupling effect of damage and elastic-plastic material behavior is considered in this work, which means mechanical properties such as Young’s modulus E and the critical strength are not degraded with the fracture. For elastic deformation, the nucleation and growth of cracks are determined by the tensile component, rather than the compressive behavior

[30, 150, 206]. While for the plastic part, both tensile and compressive component can result in the crack propagation [207, 208]. Accordingly, the strain energy density of the elastic-plastic deformation can be shown as:

$$\psi\left(\boldsymbol{\varepsilon}_{\mathrm{e}},\ \boldsymbol{\varepsilon}_{\mathrm{p}},\ \phi\right)=g\left(\phi\right)\left(\psi_{\mathrm{e}}^{+}\left(\boldsymbol{\varepsilon}_{\mathrm{e}}\right)+\psi_{\mathrm{p}}\left(\boldsymbol{\varepsilon}_{\mathrm{p}}\right)\right)+\psi_{\mathrm{e}}^{-}\left(\boldsymbol{\varepsilon}_{\mathrm{e}}\right) \tag{7.4}$$

where the superscripts "+" and "–" denote the tensile and compressive components of the elastic strain energy density, and PF degradation function g(ϕ) determines the fracture form, to be defined. The volumetric-deviatoric split method considering the bulk modulus *K*, referring the methods of Khalil, et al. [207] and Zhou, et al. [209], is used to determine the elastic strain energy density as:

$$\psi_{\mathrm{e}}^{+}\left(\boldsymbol{\varepsilon}_{\mathrm{e}}\right)=K\left\langle \mathrm{tr}\left(\boldsymbol{\varepsilon}_{\mathrm{e}}\right)\right\rangle_{+}^{2}/2+\mu\left(\boldsymbol{\varepsilon}_{\mathrm{e,\,d}}:\boldsymbol{\varepsilon}_{\mathrm{e,\,d}}\right),\quad \psi_{\mathrm{e}}^{-}\left(\boldsymbol{\varepsilon}_{\mathrm{e}}\right)=K\left\langle \mathrm{tr}\left(\boldsymbol{\varepsilon}_{\mathrm{e}}\right)\right\rangle_{-}^{2}/2 \tag{7.5}$$

where $\boldsymbol{\varepsilon}_{\mathrm{e,d}}$ is the deviatoric part of the elastic strain tensor, and the operator $\langle\ \rangle$ is the Macaulay brackets that is defined as $\langle\cdot\rangle_{+}=(\cdot+|\cdot|)/2$ and $\langle\cdot\rangle_{-}=(\cdot-|\cdot|)/2$.

Determination of the plastic strain energy density is one of the main challenges for most programs of the PF fracture analysis. Generally, the plastic strain energy density can be [210]:

$$\psi_{\mathrm{p}}\left(\varepsilon_{\mathrm{p}}\right)=\int_{\varepsilon_{\mathrm{p}}}\sigma_{\mathrm{f,e}}\left(\varepsilon_{\mathrm{p}}\right)\mathrm{d}\varepsilon_{\mathrm{p}} \tag{7.6}$$

where $\sigma_{\mathrm{f,e}}$ is flow stress of the undamaged body. A backward Euler discretization of plastic flow rule are commonly used in literature [141, 149, 152, 206, 207, 211] to obtain the equivalent plastic

strain $\varepsilon_{p,eq}$ based on the isotropic hardening with the von-Mises stress yield surface function. The plasticity is an energy dissipation process and thus, the plastic strain energy density is expressed as the plastic dissipation density, i.e., the COMSOL global variable *solid.Wp* [142].

Discrete crack surface is smoothed by the continuous phase field $\phi \in [0,1]$ and its bandwidth is controlled by the phase field length scale l_0. Then, the calculation of the volumetric fracture energy is approximated from the crack surface as:

$$\Phi = \int_{\Gamma} G_c \mathrm{d}\Gamma \approx \int_{\Omega} G_c \gamma(\phi, \nabla\phi) \mathrm{d}\Omega \tag{7.7}$$

where Γ is the discontinuous crack surface in a solid body Ω, $\gamma(\phi, \nabla\phi)$ is the crack surface density functional and G_c is the critical energy release rate. The fracture energy density is then derived as:

$$\varphi(\phi, \nabla\phi) = G_c \gamma(\phi, \nabla\phi) \tag{7.8}$$

A widely accepted evaluation of fracture energy density [211] is used in this work as:

$$\varphi(\phi, \nabla\phi) = \frac{G_c}{4 c_\alpha l_0} \left(w(\phi) + l_0^2 |\nabla\phi|^2 \right) \tag{7.9}$$

where $w(\phi)$ is the geometric crack function and satisfy the boundary conditions: $w(1)=1$, $w(0)=0$ and $w'(\phi) \geq 0$ for $\phi \in [0,1]$. Commonly, the geometric crack function and the scaling constant c_α are determined as:

$$w(\phi) = 2\phi, \quad c_\alpha = \int_0^1 \sqrt{w(\phi)}\, \mathrm{d}\phi = 2\sqrt{2}/3 \tag{7.10}$$

To ensure the monotonically increasing of the phase field during the deformation, a history variable H is defined for the phase field in a loading process to store the potential energy. For a current time τ within a total time t, the history variable can be expressed as:

$$H = \max_{\tau \in [0,t]} \left(\psi_{\mathrm{e}}^{+}(\tau) + \psi_{\mathrm{p}}(\tau) \right) \tag{7.11}$$

7.2.2 Determination of the degradation function and phase field length scale

The effect of cracking on the material stiffness is reflected by the PF degradation function g(ϕ). Many types of g(ϕ) functions are used in literature that can be categorized as the simple linear, quadratic, cubic and the hybrid model, etc. [149, 151, 152, 212]. Here, a widely used quadratic degradation function for phase field in elastic-plastic metal is applied and expressed as:

$$g(\phi) = (1-k)(1-\phi)^2 + k \tag{7.12}$$

where k is a small constant for the model to avoid the singular matrix due to the vanishing of tensile strain energy density, with the phase field ϕ tending to 1 [209]. Thus, in this work, k=1×10^{-6}.

In terms of the phase field length scale l_0, literature shows that it is related to the critical stress σ_c and furtherly determines the cracking initiation and propagation [137]. As an important parameter strongly affecting the modeling of the PF analysis, unfortunately, there is no perfect method to determine in existing literature. Based on the theoretical derivation of the uniaxial

homogeneous stress response for different degradation functions $g(\phi)$, Borden et al. [149] obtained a relationship between the critical stress σ_c and length scale for quadratic $g(\phi)$. However, it was validated that the formula is accurate for the brittle fracture but not good enough for the elastic-plastic fracture [30, 141, 149]. Another widely-used expression for phase field fracture is [208]:

$$\sigma_c = \sqrt{27EG_c/256l_0} \tag{7.13}$$

In addition, clarification of the critical stress σ_c is also a challenge in the simulation. Duda et al. [208] studied that the critical stress has a relationship with the yield strength, which is $\sigma_c=\kappa\cdot\sigma_y$ and κ is in the range $1.4\leq\kappa\leq2.4$. Consequently, the phase field scale l_0 can be determined. Although flaws exist in Eq. (7.13) to describe the fracture of elastic-plastic material, it still can be a reference for the determination of l_0.

7.2.3 Governing equations of PF fracture

Proceeding the deduction from Eq. (7.1), the total potential energy functional $E(\mathbf{u}, \phi)$ can be expressed as:

$$E(\mathbf{u},\phi) = \int_\Omega \left(g(\phi) H + \psi_e^- (\boldsymbol{\varepsilon}_e) \right) d\Omega + \frac{G_c}{4c_\alpha l_0} \int_\Omega \left[w(\phi) + l_0^2 |\nabla\phi|^2 \right] d\Omega \tag{7.14}$$

where $\mathbf{u}$ is the displacement tensor. Furtherly, minimization of $E(\mathbf{u}, \phi)$ can be deduced by the first variation of the energy function and the value should be zero, which results in the governing equations as:

$$\begin{cases} \nabla \cdot \boldsymbol{\sigma} + \mathbf{b} = 0 \\ \nabla \cdot \mathbf{q} - Q = 0 \end{cases} \quad \text{in } \Omega \tag{7.15}$$

where $\boldsymbol{\sigma}$ is the stress tensor, $\mathbf{b}$ is the external load, Q is the scalar source term and $\mathbf{q}$ is the flux vector that are deduced as:

$$Q = \frac{\partial W}{\partial \phi} = g'(\phi) H + \frac{G_c}{4 c_\alpha l} w'(\phi) = 2(\phi - 1) H + \frac{G_c}{2 c_\alpha l} \phi \tag{7.16}$$

$$\mathbf{q} = \frac{\partial W}{\partial \nabla \phi} = \frac{G_c}{2 c_\alpha} l \cdot \nabla \phi \tag{7.17}$$

7.2.4 Diffusion of H in the pipeline steel

Similar to the H diffusion analysis in Chapter Six, NILS and dislocation are considered as the sites that H atoms can reside in. Taylor's model was also employed in this chapter. Additionally, it is assumed and observed [26, 71] that the cracking due to the HE is intergranular and thus, H concentration on grain boundary $C_{\mathrm{T}}^{\mathrm{gb}}$ should be considered in this work. Consequently, the total H atom concentration C is determined as:

$$C = C_{\mathrm{L}} + C_{\mathrm{T}}^{\mathrm{d}} + C_{\mathrm{T}}^{\mathrm{gb}} \tag{7.18}$$

Based on the theory that the mass diffusion is driven by the gradient of chemical potential, the H flux J can be determined as in Eq. (6.8) and relative parameters are same as in Chapter Six. Utilizing the divergence theorem, the H concentration equilibrium formula can be derived as:

$$\frac{dC_{\mathrm{L}}}{dt}+\frac{dC_{\mathrm{d}}}{dt}+\frac{dC_{\mathrm{gb}}}{dt}=D\nabla^{2}C_{\mathrm{L}}-\frac{D\overline{V}_{\mathrm{H}}}{RT}\nabla\left(C_{\mathrm{L}}\sigma_{\mathrm{H}}\right) \tag{7.19}$$

where the derivatives of H concentrations in traps is deduced referring the Oriani's equilibrium theory and is written based on Eq. (6.4) as:

$$\frac{\mathrm{d}C_{\mathrm{T}}^{n}}{\mathrm{d}t}=\frac{\mathrm{d}C_{\mathrm{L}}}{\mathrm{d}t}\left(\frac{K^{n}N_{\mathrm{T}}{}^{n}}{N_{\mathrm{L}}+C_{\mathrm{L}}K^{n}}-\frac{\left(K^{n}\right)^{2}C_{\mathrm{L}}N_{\mathrm{T}}{}^{n}}{\left(N_{\mathrm{L}}+C_{\mathrm{L}}K^{n}\right)^{2}}\right) \tag{7.20}$$

7.3 Modeling of the denting induced cracking

7.3.1 Material models and geometric configurations

An X52 steel pipeline model was built in COMSOL software based on the actual size in literature [213]. Geometric configurations are listed in Table 7.1, as well as the material parameters including both mechanical and hydrogen transport properties. Mechanical properties were used for the solid mechanics analysis during the denting and the chemical parameters service for the H atom diffusion simulation. Hardening model σ_{hard} for X52 steel is expressed as [19]:

$$\sigma_{\mathrm{hard}}=\sigma_{\exp}\left(\varepsilon\right)-\sigma_{\mathrm{y}}=\sigma_{\exp}\left(\varepsilon_{\mathrm{p}}+\sigma_{\mathrm{eq}}/E\right)-\sigma_{\mathrm{y}} \tag{7.21}$$

where σ_{exp} is the experimental stress-strain curve of the X52 steel as shown in Fig. 7.1, σ_y is the yield strength, σ_{eq} is the equivalent stress, ε is the strain and ε_p is the plastic strain. In this work, true stress-strain curve and the material properties of X52 pipeline steel were obtained from the experiments in literature [69, 214]. Equivalent plastic strain and von Mises stress were used to represent the plastic strain ε_p and the equivalent stress σ_{eq}, respectively. Parameters of H diffusion in X52 pipeline steel adopted from literature have been cited in table 7.1.

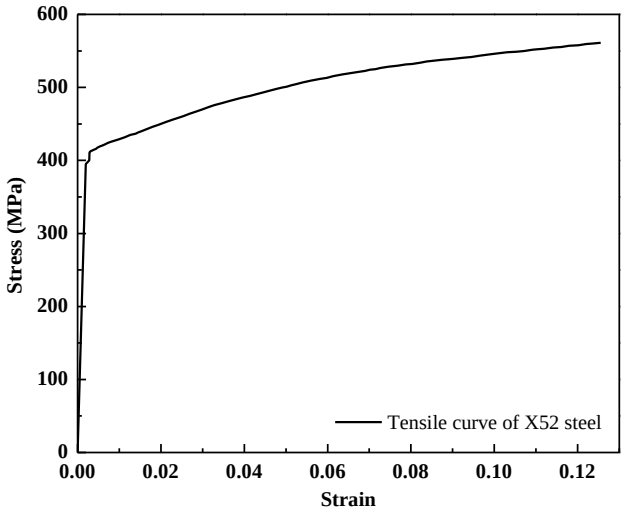

Figure 7.1 True stress-strain curve of X52 steel tested in Ref. [214].

Geometric parameters of the model are listed in Table 7.1. Generally, the length of the pipeline model should be long enough to eliminate the effect of the boundary conditions on the defect area. Yet, restrained by the computational ability and convergence requirement, it is necessary to properly reduce the model length during the solving. In addition, solution of the phase field for HIC is based on the coupling of multiple physics which introduces large amounts of DOFs

(degree of freedoms) and as a result, massive computational resource is consumed. Considering the phenomenon observed in this work that the damage only occurs in a small zone around the dent center, the model can be reduced to a reasonable length.

Hydrogen degradation of mechanical properties of the steel is an essential consideration on the coupling of cracking with the H diffusion. Based on the Density Functional Theory (DFT) calculations, one of the most popular formular in literature [30, 71, 215] is the hydrogen coverage η linearly functioning on the critical energy release rate (in this work, i.e., the fracture toughness),

$$G_c(\eta) = (1 - \chi\eta) G_c(0) \tag{7.22}$$

in which χ is a hydrogen damage coefficient calibrated by the DFT analysis and experimental results [216]. The hydrogen coverage is calculated using Langmuir–McLean isotherm theory as:

$$\eta = \frac{C_{\mathrm{b}}}{C_{\mathrm{b}} + \exp\left(-\left|W_{\mathrm{B}}^{\mathrm{gb}}\right| / (RT)\right)} \tag{7.23}$$

where C_{b} is the bulk H concentration in the units of appm (atomic parts per million). It is assumed and observed that the HIC is intergranular cracking [217, 218]. Therefore, parameter η is the hydrogen coverage over the grain boundary and $W_{\mathrm{B}}^{\mathrm{gb}}$ is the binding energy for the grain boundary. Here, density of grain boundary traps $N_{\mathrm{T}}^{\mathrm{gb}}$ and the binding energy $W_{\mathrm{B}}^{\mathrm{gb}}$ are determined as [71]:

$$N_{\mathrm{T}}^{\mathrm{gb}} = 5.06 \times 10^{25} \text{ sites/m}^3, \; W_{\mathrm{B}}^{\mathrm{gb}} = -24.7 \text{ kJ/mol} \tag{7.24}$$

With respect to the essential constant χ that describing the degeneration of the metal owning to the absorbed hydrogen, a widely used value of 0.89 is applied for the cracking simulation of the steel. Although this value is determined by the fitting of DFT calculations and is imperfect for the X52 pipeline steel, discussion about this parameter is beyond the scope of this work.

Table 7.1 Geometric sizes, mechanical and H transport properties for FE model.

Mechanical Parameters	Value	H transport Parameters	Value
Steel grade	X52	Temperature, T	300 K
Outer pipe diameter, D_o	355.6 mm	Lattice diffusivity, D_L	1.27×10^{-2} mm^2/s [63]
Diameter of indenter, D_2	100 mm	Atomic weight of iron, M_m	55.8×10^{-3} kg/mol
Pipe wall thickness, t	7.92 mm	Binding energy of dislocations, W_B^d	-25 kJ/mol [184]
Length of pipe model, L_1	300 mm	Partial molar volume of H in solid solution, V_H	2×10^{-6} m^3/mol
Elastic modulus, E	203 GPa	Cubic edge length of iron, a	0.2867 nm [187]
Shear modulus, G	80 GPa	Sievert constant for X52, S_H	0.029 wppm/bar$^{1/2}$
Poisson's ratio, υ	0.3	Density of iron, ρ_M	7.87×10^3 kg/m^3
Yield strength, σ_y	395 MPa		
Ultimate strength, σ_U	560 MPa		

7.3.2 COMSOL modules and boundary conditions

Research of this work was composed of mechanical (i.e., denting), H atom diffusion and the PF cracking analysis. As a result, Solid Mechanics and Mathematics modulus were used for the

simulation. Coefficient Form PDE module was implemented for the H diffusion calculation, Poisson's Equation module was configured to solve the governing equation Eq. (7.15) of PF method and the history variable of the phase field H in Eq. (7.11) was defined through the State Variables.

Considering the cost of computation and efficiency, two types of models were established for the comparison in this work, i.e., solid model and solid coupling with shell models, as shown in Fig. 7.2. The pipeline and the indenter were quarterly modeled applying symmetric conditions. Most details can be obtained from the solid pipeline model which is approximated to the reality. Meanwhile, highest computation resources were demanded by the solid model and the DOFs in Fig. 7.2 (a) can reach to 100,000 even with lots of simplifications, which is unacceptable for the PF analysis. Simulations of the solid models showed that the damage was limited to a small area at the dent. Therefore, solid elements coupled with shell elements were applied for the modeling [219] and the PF damage only effects in the solid zone where the indenter was loaded. Similarly, diffusion of H atoms was also limited in the solid zone. Solid-Thin Structure Connection relationship was employed for the attachment between the shell and solid elements.

Detailed mesh is also shown in Fig. 7.2, where fine grids with the smallest element size l_e were attributed to the dent area and relative coarse elements were meshed on the remained domains. Element size l_e of the cracking zone acts as an important factor of the PF analysis. In literature, l_e smaller than $l_0/2$ is proved to be acceptable for the cracking simulation [220, 221]. Phase filed scale l_0 for X52 pipeline steel was determined by Eq. (7.13) with the factor κ=2.25 and the yield strength σ_y=395 MPa. As a result, the phase field scale l_0 was determined as 4 mm in this work. Another important parameter for the simulation is the loading speed (or the time step increment) of the denting. It is reported in the FE mechanical test simulation that the step increment

should be small enough to ensure the accuracy [152], and the H atoms also need enough time to diffuse in the steel. However, denting is generally a transient or short-time process in engineering, which means there is not enough time for H diffusion. Thus, loading speed as 3 mm per minute was taken to balance the relative considerations.

Boundary conditions for the model were similar for both solid mechanics and H diffusion. For mechanical analysis, symmetric conditions were employed on the cross-section surface of the pipe and the indenter. Fixed constrained condition was applied on the bottom line of the pipeline. The load of denting was controlled by the downward displacement of the indenter. Contact pair was defined between the indenter and the pipe, and the rigid material properties were assigned to the indenter. The pipe was bearing the internal pressure p when transporting the blended gas. Moreover, constant H concentration $C_i=C_0$ was defined as the boundary load of the inner surface of the pipe and the outer surface was defined as no flux [200, 202, 222]. Initial H concentration is related to the component ratio of the hydrogen gas blended into the natural gas, i.e., the H concentration is dependent on the partial pressure of hydrogen gas. To evaluate the effects of H concentration and internal pressure individually, the corresponding relationship was not maintained. The maximum operation pressure (MOP) of the pipeline can be calculated by the Barlow's law [38] and the MOP of the pipeline used in this work is 25.35 MPa, where 0.8 has been applied as the safety factor. Ratio of hydrogen in the blended gas was reported to be 1% to 20% [60, 194] and thus the partial pressure of H gas pressure ranged from 0.4056 MPa to 4.056 MPa. Based on the Sivert's law as Eq. (6.16), the boundary H concentration C_0 was calculated as 0.058 to 0.185 wppm (weight parts per million).

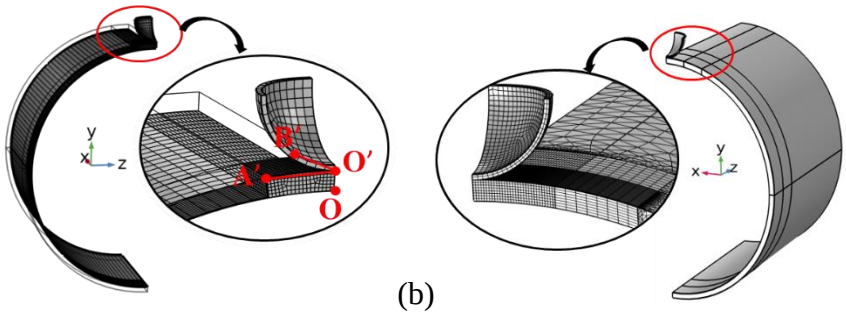

(a) (b)

Figure 7.2 (a) FE solid-shell coupling model, (b) solid model, respectively and the mesh of models. O'A' and O'B' represent the circumferential and longitudinal directions on outer surface, respectively, and the point O indicates the dent center on inner surface.

7.3.3 Program configurations

As presented in Eq. (7.4), elastic strain energy density has been decomposed into positive and negative terms to reflect the degradation of the material resulting from the cracking. In literature, programs in subroutine of ABAQUS or other numerical tools are popular for the PF cracking analysis [141, 144, 145], while limited experiences can be found for the implementation process in COMSOL. Chen and Wu [215] defined the cracking driving force using the Rankine criterion, by which the recognition of tensile and compressive deformations was determined by the property of first principal stress [223]. However, a more general method was provided by Zhou, et al. [209] and the elasticity matrix **D** of the material was defined manually into the material model in COMSOL. Unlike the brittle fracture investigated in literature, elastic plastic cracking is considered in this work and therefore, the elastic strain in local coordinate system has to be distinguished from the total strain. Elastic principal strains were obtained through the matrix diagonalization of the elastic strain matrix in local coordinate, and then were implemented into the degraded elasticity matrix [142].

Convergence of the PF fracture analysis is an acknowledged challenge in FE simulation. Lots of computational resources can be occupied although geometrically smaller models and fewer DOFs are performed. Therefore, appropriate algorithms and configurations in COMSOL need to be carried out and tested. Segregated algorithm is verified as a robust and effective method for the convergence of the PF analysis [30, 149, 210]. Compared to the fully coupled solver for multiphysics, the solution was segregated into several steps, i.e., the Displacement, H diffusion, the PF damage evolution and the History state. The BDF solver was selected as the time stepping method and the PARDISO was used as the direct solver of the time-dependent analysis. The governing equations in strong form are automatically converted to the equivalent weak form through the weighted residual method and furtherly solved by the FE discretization [215].

7.3.4 Validation of phase field model

Adequate work has been carried out validating the accuracy of the PF method applied on the brittle fracture simulation, including the cracking simulations of the hydrogen charged steel [218]. However, few experimental validations can be obtained in literature for the elastic plastic fracture model using the PF method. To test and prove the effectiveness of the model developed based on the theoretical deductions, the fracture simulation of a tensile test from literature [141] was reproduced in this work.

Tensile test experiment was carried out on the flat Steel-1.0553 specimen as shown in Fig. 7.3 (a), where the fracture appearance is also displayed. An FE 2D model established for PF fracture analysis in this work is shown in Fig. 7.3 (b), where the detailed contour of damage field variable ϕ is presented. Geometric size, material parameters and boundary conditions in simulation are same with the experimental configurations. Experiment showed that the fracture initiated at

the center of the specimen as the displacement increases, which was consistent with the simulation results. Furthermore, obvious necking phenomenon can be observed both in experiment and the PF analysis. Comparison between the tensile load-displacement curve is executed and presented in Fig. 7.4. Experimental results show that the maximum load of the tensile test is 22.26 kN and the related displacement is 8.48 mm. The maximum load and the corresponding displacement are 21.58 kN and 8.46 mm, respectively. The error of the maximum loads between the experiment and the PF model in this work is only 3%. The error in terms of the maximum tensile displacement is also small, which are 11.72 mm and 11.05mm for experimental and FE results. Besides, numerical results in literature have little difference compared to the simulation in this work, although different types of PF methods are applied. In conclusion, the PF theories and configurations are validated to be accurate and reliable.

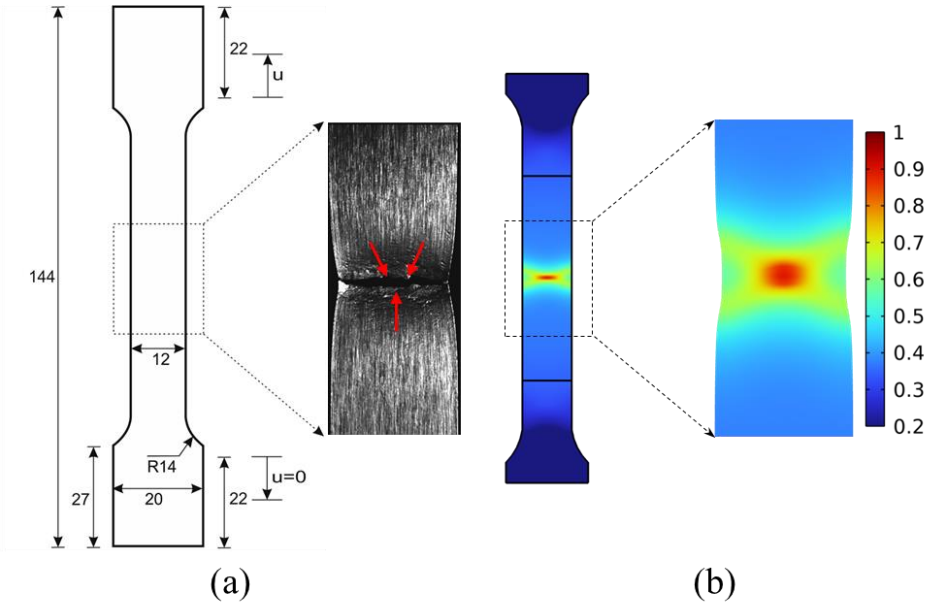

Figure 7.3 Tensile specimen for the validation of PF analysis in this work: (a) Steel-1.0553 specimen geometric size and the fracture characteristics [141]; (b) FE model in this work and the contour of damage field variable ϕ.

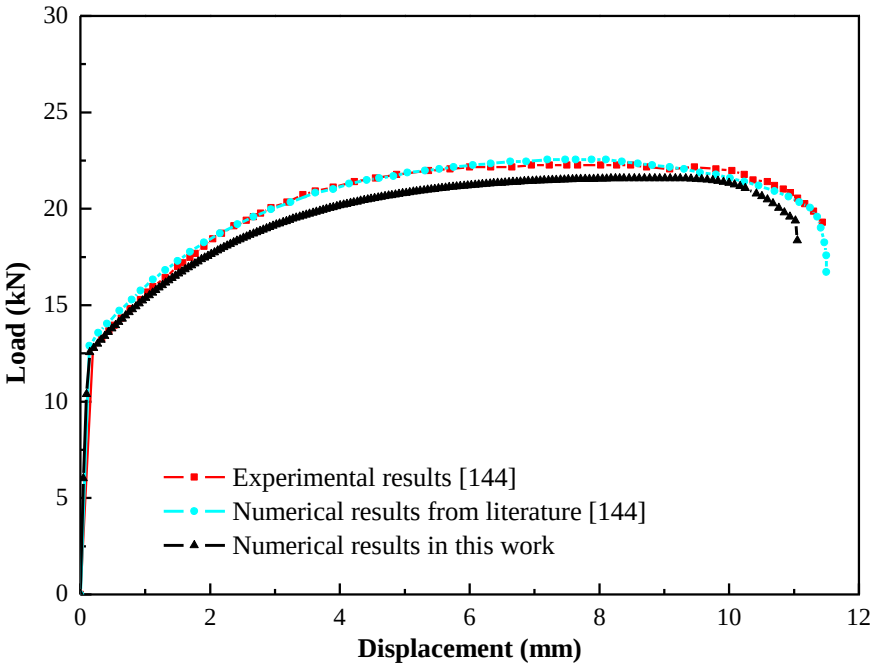

Figure 7.4 Tensile load-displacement curves from experimental and simulation results in literature [141] and the PF analysis in this work.

7.4 Results and discussion

7.4.1 Damage evolution for denting process

Cracking due to the indentation is the main concern for the assessment of dented pipelines. Existing failure evaluation methods such as depth-based and strain-based methods in standards are not suitable for the cracking induced by the dent. Field test reported in literature [48] showed that cracks can initiate when the dent is shallow, and the dent depth is smaller than 6% of the outer pipe diameter. Limited literature can be found to directly assess the crack initiation during the denting process. In this part, PF method was used for the crack initiation research during the denting process. Solid-shell coupling model and solid model were compared to investigate the feasibility of the former method.

Contour of PF variable ϕ is shown in Fig. 7.5 of both types of models, indicating the potential of cracking for different parts of the pipeline. Crack initiation predictions using the PF method reveal that with the downward movement of the indenter, cracking failure finally initiates on the inner surface of the dent center (i.e., point O in Fig. 7.2). An important phenomenon can be observed that the position of maximum ϕ is changed with the indentation depth. When the displacement of indenter (i.e., u) is small, the maximum ϕ is located on the outer surface of the dent center (i.e., point O' in Fig. 7.2). When u increases, the position of maximum ϕ shifts to the inner surface. The transferring of ϕ indicates the failure prediction [215] for different depth of dent, i.e., the potential position of cracking shifts from the outer surface to the inner surface of the dent center. The maximum indenter depth is 17.90 mm (5% of D_o) for the solid-shell model, which is smaller than the depth-based assessment criterion (6% of D_o). Furthermore, it can be seen from the solid model in Fig. 7.5 (b) that only a small zone at the dent center is affected by the PF damage evolution, which means that the simplification of the solid-shell model is reasonable and effective. The limited error of the displacement u for different denting stages also presents the accuracy of the solid-shell coupling model. In conclusion, the solid-shell coupling model can satisfy the requirement of PF analysis and is used as the model for the following investigations in this work.

To further study the mechanical performance of the pipeline, von Mises stress σ_e and equivalent plastic strain ε_{eq} of the solid-shell coupling model are presented in Fig. 7.6. When the cracking occurs (ϕ=1), the maximum σ_e and ε_{eq} are located on the outer surface, with the maximum value of 546 MPa and 0.1, respectively. In contrast, both σ_e and ε_{eq} are small on the inner surface around the dent center, resulting from the cracking of the pipeline. The maximum and minimum values of σ_e and ε_{eq} are marked in Fig. 7.6, in which the peak values deviate from the dent center in circumferential direction. Fig. 7.7 presents the variations of von Mises stress and the equivalent

plastic strain of points O and O' during the denting process. Stress of point O appears a rising trend with the denting proceeding, and rapidly decreases to zero when cracking happens, meanwhile the effective stress at point O' reaches the maximum value. As for the plastic deformation, the equivalent plastic strains maintain at high levels in both inner and outer surfaces until the fracture. Noted that von Mises stress at point O experiences a sudden decline at point P as marked in Fig. 7.7, suggesting that the structure loses the capacity of bearing loads. Calculation results show that the indenter displacement at point P is 16.3 mm and the relative phase field factor ϕ is 0.69. Depth-based and strain-based criteria provided in ASME B31.12 reviewed in Section *2.2.4* can be used for comparison. For the pipeline that only bears the denting load, the depth-based criterion (i.e., 6%) has been proved to be invalidated. The strain-based criterion in ASME B31.12 evaluates the strain through the parameters measured in dent, and the equivalent plastic strains are used for the assessment. When the phase field factor ϕ equals 0.69, ε_{eq} on the outer surface of the dent center is 0.066, which has exceed the strain limitation of 2%.

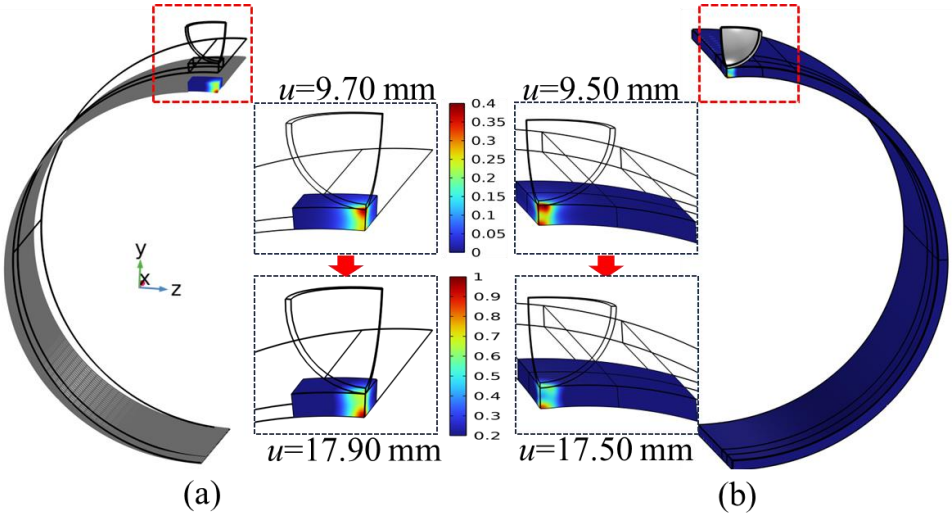

Figure 7.5 Distribution of PF variable ϕ with different indentation depths for the (a) solid-shell coupled model and (b) solid model.

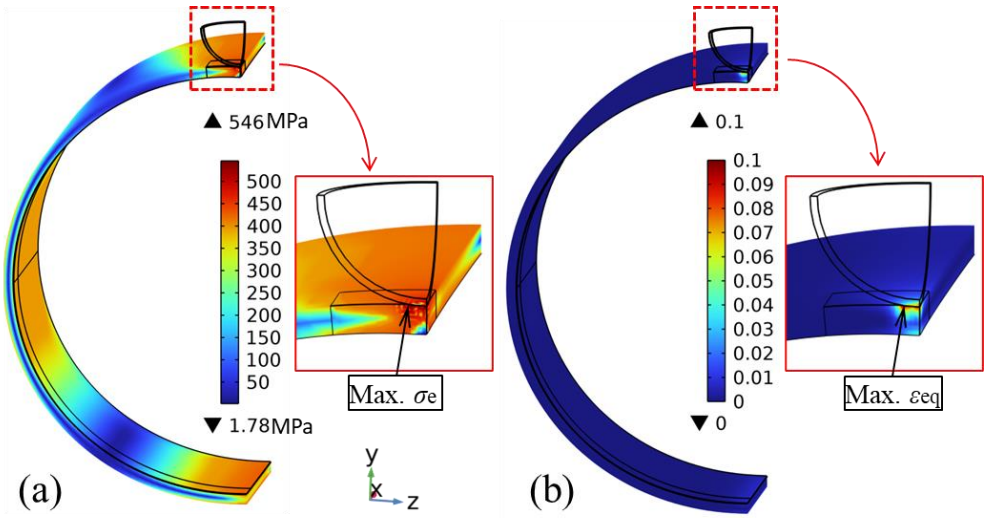

Figure 7.6 Distribution of (a) von Mises stress and (b) equivalent plastic strain as the cracking occurs.

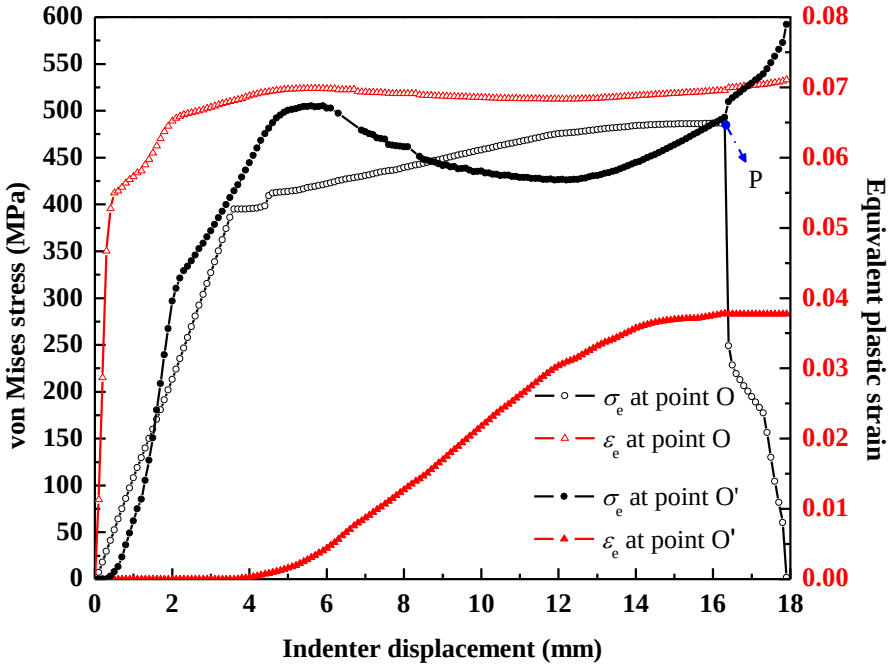

Figure 7.7 Variations of von Mises stress and the equivalent plastic strain of points O and O' over the denting process.

7.4.2 Hydrogen induced cracking for the dented pipeline

Hydrogen induced cracking resulting from the denting was investigated using the solid-shell coupling model. Generally, the H concentration inside the pipeline steel is dependent on the internal pressure, while the internal pressure was not considered in this part to solely study the effect of H on the crack initiation. The initial H concentration C_0 varies from 0.038 wppm to 0.5 wppm and other parameters were in line with the denting simulation.

Based on the degradation function in Eq. (7.22), the fracture toughness G_c is reduced by H atoms inside the steel. Damage evolution for the pipeline with the initial H concentration C_0=0.058 wppm over the denting process is shown in Fig. 7.8, in which the distributions of total H concentration C, von Mises stress σ_e and equivalent plastic strain ε_{eq} are also presented. Here, C_0 is constant at 0.058 wppm which corresponds to the H gas blended ratio of 2% under the maximum service pressure. In Fig. 7.8 (a), the relative maximum values of ϕ are 0.3, 0.6 and 0.9 respectively for different indenter displacements. Similar to the PF analysis of denting without H diffusion, a transfer of maximum ϕ from the outer surface to inner surface can be observed in the denting process. Calculation results show that the maximum dent depth is 16.35 mm when ϕ=1, reducing 8.7% compared to dent depth (i.e., 17.90 mm) of the denting without hydrogen. The difference indicates that the degradation effect of H on fracture toughness can directly manifest as the decrease of maximum dent depth on pipeline. Distributions of C experience limited change during the denting process and less H atoms exist in the zone adjacent to the dent center. In contrast, higher H concentrations scattered around the dent center. The maximum C changed from 0.253 wppm to 0.226 wppm during the denting process, whereas the minimum C has smaller fluctuations around 0.044 wppm. An explanation of H concentration is that the time of denting is too short for

H atoms diffusing to the cracking zone. In terms of the mechanical behavior, similar distributions can be found for σ_e and ε_{eq}. The maximum values are located on the outer surface around the dent center and increase as the indenter moving downward. When the cracking initiates, the pipeline cannot bear the external loads with the effective stress on the inner surface of the dent center reduces to zero. Similar developments of parameters discussed above can be observed for the dented pipeline with different initial H concentrations ranging from 0.038 wppm to 0.5 wppm.

Variations of σ_e and ε_{eq} at Point O over the denting process are shown in Fig. 7.9, considering the conditions of different initial H concentrations and as a comparison, dent without H diffusion is added into figures. It should be noted that the stress and strain curves end when the value of ϕ is 0.9, at which the structure is considered to fail. In general, the development of von Mises and equivalent plastic strain curves are not affected by the hydrogen contents, and the hydrogen concentration only affects the maximum denting depth and the maximum strain. With the increasing of C_0 from 0 wppm to 0.5 wppm, the maximum indenter displacements reduce from 17.5 mm to 10.7 mm, as shown in Fig. 7.9 (a). The final von Mises stress when ϕ is 0.9 has no obvious change for different C_0. At the same time, the point when von Mises stress starts to rapidly decline comes earlier when C_0 increases, and as marked in Fig. 7.9 (a), the transfer points are around ϕ=0.63. Before the transferring point, the von Mises stress curves are overlapped. Equivalent plastic strains at the dent center on inner surface are undergoing increasing trends over the denting, while the maximum ε_{eq} decreases with the rising C_0. Compared to the maximum ε_{eq} (i.e., 0.038) of dented pipeline without hydrogen, the maximum ε_{eq} varies from 0.033 to 0.016 when C_0 increases from 0.038 wppm to 0.5 wppm. The maximum values of ε_{eq} are all close to the critical equivalent strain (i.e., 2%) provided in ASME B31.12, which means the existing assessment method of dent is effective for the dented pipeline under the discussed conditions.

Furthermore, H diffusion before the crack initiation is interested in this part, and the total H concentrations along the circumferential (O'A') and longitudinal directions (O'B') are plotted in Fig. 7.10. The peak values of *C* are distributed on the outer surface of the dent area and in general, fluctuations of H concentration are located at the area ranged from the dent center to 10 mm away from the center. Due to the compression of indenter, H concentration at the dent center is significantly lower than other areas. Hydrogen atoms concentrate on the outer surface around the dent center by about 5 mm.

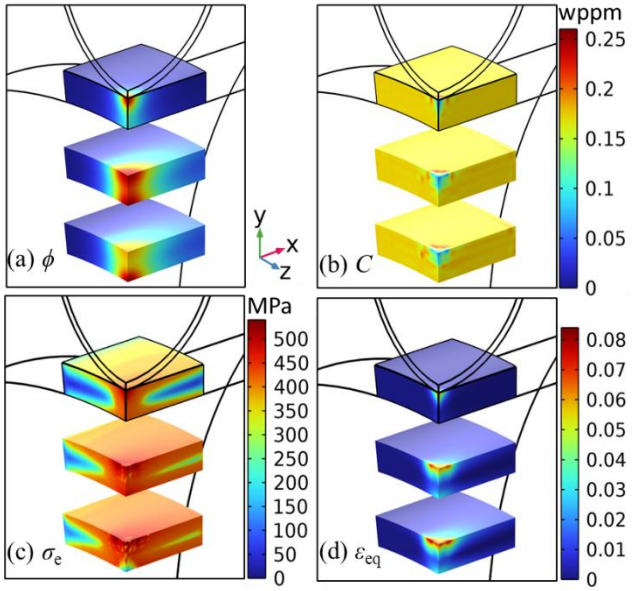

Figure 7.8 Variations of (a) damage evolution ϕ, (b) total H concentration *C*, (c) von Mises stress σ_e and (d) equivalent plastic strain ε_{eq} for the pipeline with initial H concentration C_0=0.058 wppm. Corresponding displacement values of the indenter are 6.7 mm, 13.3 mm and 15.7 mm, from top to the bottom respectively in each graph.

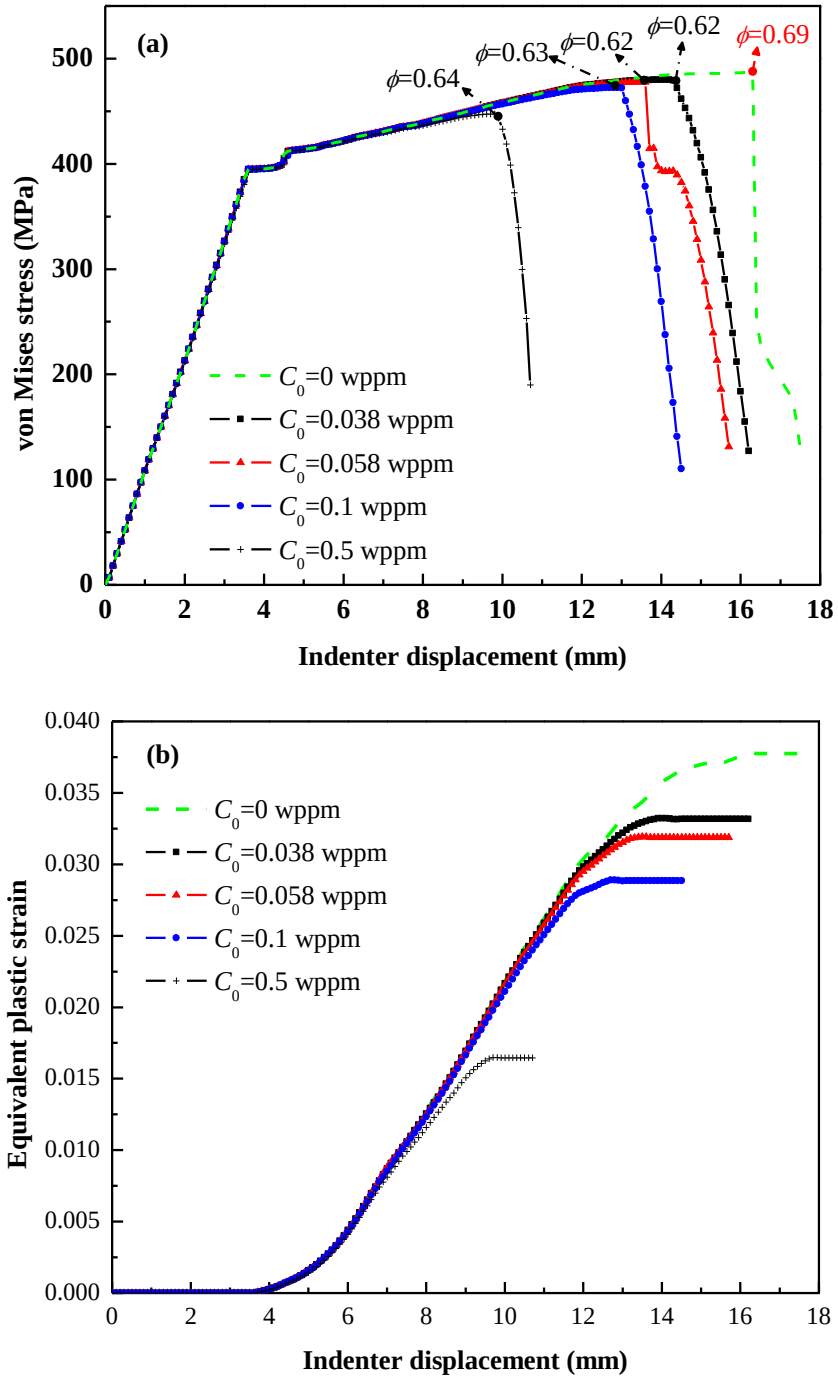

Figure 7.9 Variations of (a) von Mises stress and (b) equivalent plastic strain on point O influenced by different initial H concentrations over the denting process during the denting process.

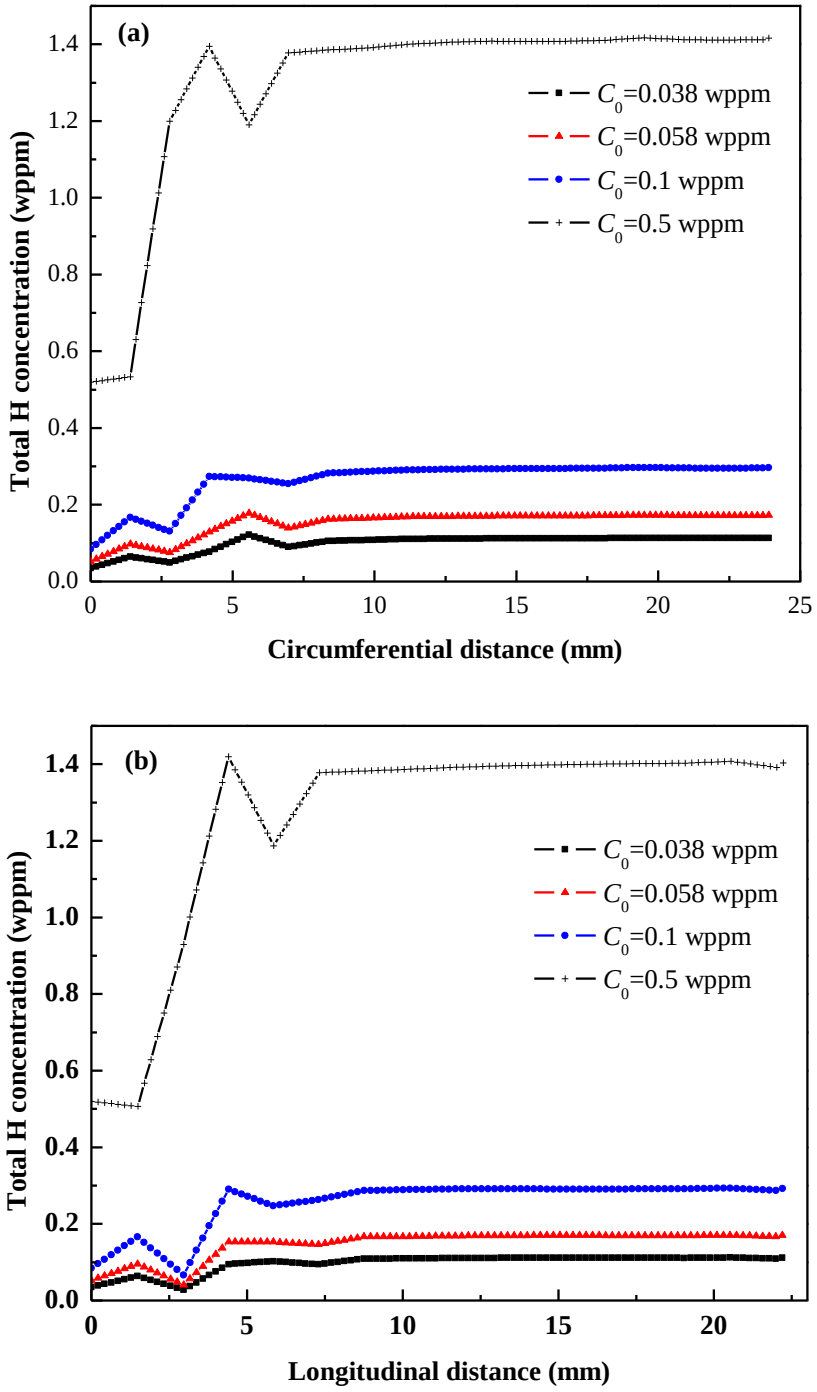

Figure 7.10 Variations of total H concentration in (a) circumferential and (b) longitudinal directions on the outer surface with different initial H concentrations when the phase field ϕ=0.9.

7.4.3 HIC for the pipeline in service

Pipeline is a structure mainly subjected to the internal pressure and therefore, the effect of pressure on the damage evolution considering HIC is investigated in this section. Inclusion of pressure factor into the PF analysis remarkably elevates the difficulty of convergence and the requirement of computational resource. Therefore, limited cases were carried out to present the HIC development for a dented pipeline in service. The pipeline was pressured with p of 4 MPa and 8MPa first, and then the denting process was applied. Damage evolution of dented pipelines (no H diffusion is considered) with and without the internal pressure p are shown in Fig. 7.11, displaying the maximum value of ϕ in different stages. In Fig. 7.11, von Mises stress and equivalent plastic strain curves are evaluated for point O and end at the time steps when the phase field ϕ=0.9. As shown in Fig. 7.11 (a), curves of σ_e and ε_{eq} are strongly affected by the internal pressure, and the maximum values are enhanced more than 10% compared to the pipeline without pressure. At the same time, the maximum dent depth reduces from 17.5 mm to 7.8 mm when p=8 MPa is applied. The result indicates that cracking can initiate much earlier with the effect of internal pressure during the denting process although the HIC is not considered. From Fig. 7.11 (b) and (c), peak values of phase field ϕ in both conditions experience the transfer from the outer surface to inner surface, while the relative dent depths are much reduced due to the internal pressure.

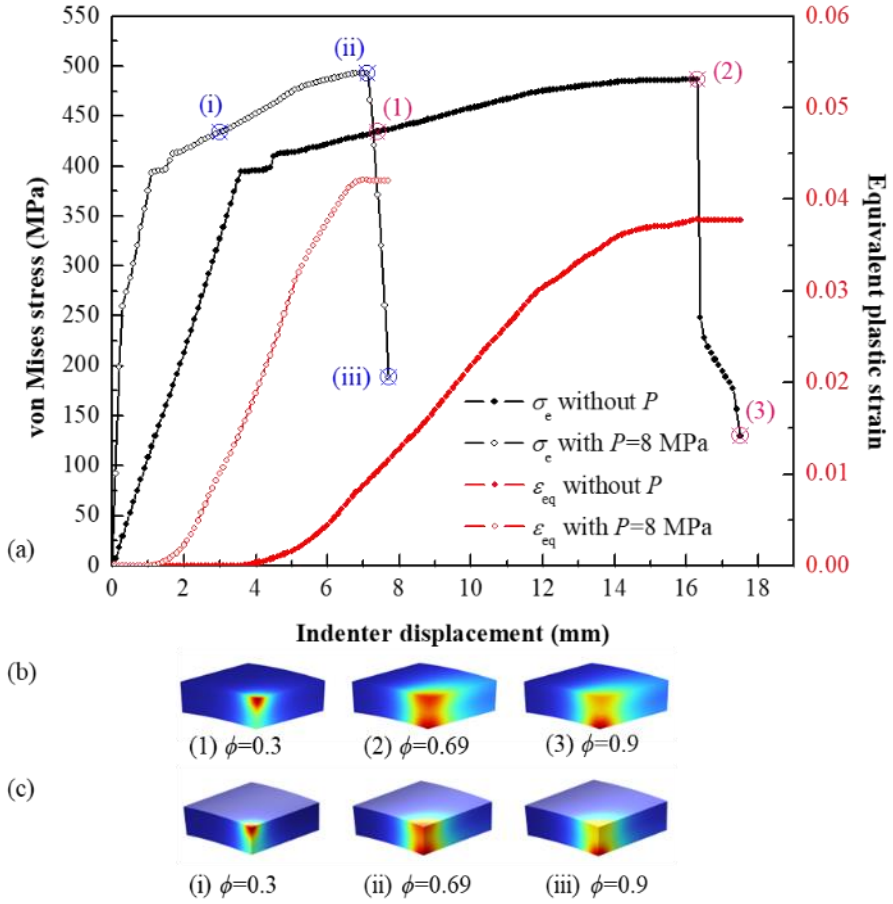

Figure 7.11 (a) Evaluation curves of von Mises stress σ_e and equivalent plastic strain ε_{eq} for point O over the denting, (b) damage evolution for the pipeline without *p* and (c) with *p*, corresponding to the specific stages marked on the curve of von Mises stress.

To further discuss the effect of H diffusion, stress and strain curves for the hydrogen gas pipelines under different internal pressures are presented in Fig. 7.12, as well as the damage evolutions during the denting process. The initial H concentration C_0 is constant at 0.058 wppm to manifest the effect of internal pressure. Again, the maximum stress and strain are enhanced by the increasing of internal pressure from 4 MPa to 8 MPa, however, the amplitudes are relevant small which are 0.9% for σ_e and 8.1% for ε_{eq}. The denting depth for the crack initiation reduces from 9.8 mm to 7.3 mm, and limited influence from hydrogen on dent depths can be found compared to the

maximum values in Fig. 7.11 (a), which is 7.7 mm for stage (iii). Similar distributions of ε_{eq} in Fig. 12 (b) and (c) can be observed for different values of pressure and the critical equivalent plastic strain increases when the pressure enhances.

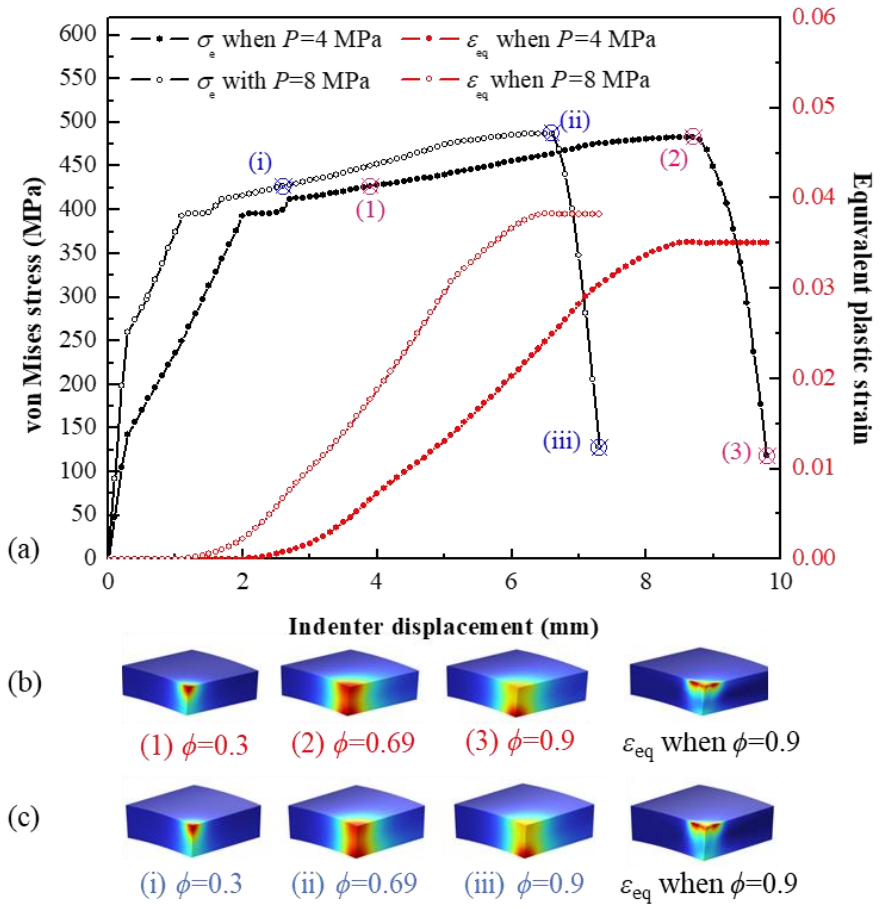

Figure 7.12 (a) Curves of von Mises stress σ_e and equivalent plastic strain ε_{eq} for point O over the denting, (b) damage evolution for the pipeline under p=4 MPa and (c) p=8 MPa, corresponding to the specific stages marked on the curve of von Mises stress, including the contours of ε_{eq} when ϕ=0.9, respectively.

7.4.4 Remarks for the HIC predictions in pipeline

Investigations in this work present the effectiveness of PF method on mechanical cracking and hydrogen induced cracking predictions, with the evolution of damage intuitively demonstrated. Analyses conducted under different conditions unfold that both hydrogen contents and the service pressure can significantly decrease the critical dent depth required for the crack initiation. Moreover, the existing assessment methods in standards (i.e., depth-based and strain-based criterion) are inaccurate for the dented pipeline bearing the H permeation and internal pressure. Therefore, an appropriate prediction method for HIC should be proposed based on the PF method. As can be seen from the stress curves in Fig. 7.9, 7.11 and 7.12, sudden declines of von Mises stress occur when the phase field ϕ reaches a specific value, which is conservatively determined as 0.7. The rapid decrease of effective stress indicates that the pipeline loses the capacity of bearing load and therefore, ϕ=0.7 can be regarded as the critical value of phase field parameter.

The critical value of indenter displacement u and the relative equivalent plastic strains corresponding to the critical ϕ are presented in Table 7.2. It can be concluded that for the dented pipeline without internal pressure, the critical dent depth as the cracking initiates cannot be evaluated using the depth-based criterion in ASME B31.12, while the strain-based criterion is available. A simplified and rough estimation of the critical H concentration based on the strain-based criteria in ASME B31.12 is 0.1 wppm under the conditions in this case. The critical partial pressure of hydrogen gas can therefore be calculated as 1.19 MPa using Eq. (6.16). The internal pressure has finite effect on the critical equivalent plastic strain on the inner surface of the dent area and a rising trend exists with the increasing of internal pressure. It should be noted that the assessment method proposed in this section cannot guide the engineering practice, resulting from the lack of calculation and measurement data. However, complete and solid method for the HIC

prediction of pipelines can be developed based on the theoretical and investigating paths proposed in this work. Furthermore, the accurate position of cracking initiation and the path of cracking propagation can be determined by analyzing the maximum phase field ϕ and estimate the zone that has high values of ϕ. It should be noted that further development of prediction method relies on finer mesh of the model and more accurate configurations of phase field parameters.

Table 7.2 Critical value of indenter displacement *u* and the maximum equivalent plastic strains ε_{eq} corresponding to the critical ϕ=0.7 for varied C_0 and the internal pressures.

C_0	0	0.038	0.058			0.1	0.5	ASME
(wppm)			p=0	p=4 MPa	p=8 MPa			B31.12
u (mm)	16.3	14.8	13.9	9.0	6.7	13.4	10.2	21.3
ε_{eq}	0.0378	0.0332	0.0319	0.0350	0.0382	0.0289	0.0165	0.02

7.5 Conclusions

An assessment method for the cracking initiation of hydrogen induced cracking is proposed based on the phase field theory. Coupling of mechanics, H diffusion and phase field analysis is implemented and developed using finite element method. Validated by the flat steel tensile specimen, the phase field method is further employed on the cracking prediction of the dented pipeline carrying hydrogen gas. To reduce the cost of computation and promote convergence, the solid-shell coupling 3D model is established for the Multiphysics analysis, which is validated to be effective for the analysis in this work.

Cracking assessment methods of dented pipelines serviced for hydrogen transportation are investigated by benchmark examples in this work. Pipelines with different conditions, i.e., denting only, denting coupled with H diffusion and denting on a pipeline in service, are discussed and compared with the criterion in ASME B31.12. Damage evolution results show that the maximum phases field ϕ transfer from the outer surface to inner surface and finally, the crack initiates at the inner surface of the dent center. Evolutions of von Mises stress and equivalent plastic strain at the dent center on inner surface are carried out for various conditions. When the internal pressure is not considered, the development of von Mises and equivalent plastic strain curves are not influenced by hydrogen, while the maximum values of denting depth and the strain are reduced with rising H concentration. For the hydrogen pipeline in service, the stress and strain of the dent center can be enhanced by the internal pressure. However, the critical dent depth can be significantly reduced when the internal pressure increases. Capacity of the pipeline bearing loads decreases significantly when the damage reaches to a specific value, i.e., ϕ=0.7, and thus, this value is determined as the threshold for failure of the dented pipeline. Further remarks for HIC predictions are proposed, and complete and solid assessment method can be developed in future based on the analysis in this work.

Chapter Eight: Conclusions and recommendations

8.1 Conclusions

In this work, finite element methods are developed for assessment of pipelines containing unconstrained plain dent and a dent combined with other defects. Different numerical models are established for dent assessment on the pipelines under varied operating conditions. For pipelines containing a plain dent, a new method based on the ductile damage failure indictor criterion combined with improved strain determination by a FE model is developed for dent assessment. The DFDI formula considers the influence of spring-back upon removal of indenter, and the difference between the equivalent strain at dent apex and the maximum equivalent strain at the whole dent area. When the indenter displacement is smaller than 8% of pipe outer diameter, the maximum DFDI can be determined from the equivalent strain at the dent apex. When the initial displacement exceeds 8% of the pipe outer diameter, the maximum equivalent strain at the dent area, which deviates from the dent apex, should be determined by the FE model. The proposed method in the standard ASME B31.8 is not accurate when the dent is deep. Considerations on shift of the maximum strain and the influence of spring-back are not included in ASME B31.8 methods.

For the corroded X80 steel pipe containing a dent, a new FE-based method is performed to assess the pressure capacity of the pipeline, and the mutual interaction between the dent and corrosion. The presence of a dent at corrosion defect remarkably changes the local stress distribution, elevating stress to plastic range. The mutual interaction between the dent and the corrosion defect depends on both the initial corrosion depth and the initial dent depth. When the corrosion defect is deep (e.g., 5.4 mm in this work), the stress is enhanced by increased dent depth, while the stress level decreases if the corrosion defect is shallow (e.g., 2.0 mm in depth). The corrosion is prone to grow in its depth direction. By analyzing the effects of dent depth and

corrosion size on the corrosion growth rate, a new burst pressure criterion is proposed based on comparison between the modified ASME B31G and DNV RP F101 methods.

To further investigate the corrosion growth in the dent defect, a Multiphysics model is developed to assess the corrosion in dent on an X52 steel pipe by considering both mechanical and electrochemical corrosion factors and their interaction at an unconstrained dent. The stress concentration at the dent accelerates corrosion due to a mechano-electrochemical interaction. As the dent depth increases, the local stress concentration is enhanced, resulting in increased corrosion activity and corrosion rate. The most negative corrosion potential and the maximum anodic current are located at the center of the dent, where the anodic reaction occurs. The anodic current density at the dent center is 2.5-3 times of that at the dent sides, indicating an accelerated corrosion. The internal pressure has a limited effect on the anodic current density. The dent with a smaller open diameter can cause greater local stress concentration and anodic current density. When the initial dent depth is less than 30 mm, smaller dents tend to accelerate local corrosion at a more rapid speed than bigger dents.

A 3-D model is developed to determine the stress/strain and H atom concentrations at an unconstrained dent on an X52 steel pipe which experiences denting, spring-back and cyclic loading processes. The cyclic loading reduces the stress level and shifts the stress concentration zone from the dent center along the circumferential direction. As the dent depth increases, the maximum H atom concentration is further shifted from the dent center to the side. There are no certain relationships among the maximum H atom concentration, von Mises stress, hydrostatic stress, and plastic strain in terms of their distributions and quantities. Pressure fluctuations decrease both the stress and H atom concentrations at the dent, providing a beneficial effect on reduced risk of the

dented pipelines to hydrogen embrittlement in high-pressure hydrogen gas environments. The indenter size has little influence on the H atom distribution in the dent area.

Furthermore, the hydrogen-induced cracking of pipelines subjected to denting process is investigated using the phase field method. The maximum phase field parameter ϕ transfers from the outer surface to the inner surface of the dent center during the denting process, and cracks initiate on inner surface. Rapid declines can be found on von Mises stress curves when the phase field rises to a critical value (i.e., 0.7), indicating that the pipeline loses the capacity of bearing loads. When the H concentration increases from 0 to 0.5 wppm, the maximum indenter displacements reduce from 17.5 mm to 10.7 mm (i.e., a reduction by 39%), and the maximum strains decrease from 0.038 to 0.016 (i.e., a reduction by 58%). Similarly, the internal pressure reduces the critical dent depth, whereas the stress and strain are less affected. Predictions of hydrogen-induced cracking of dented pipelines transporting hydrogen based on the phase field analysis provide a promising method.

8.2 Limitations and Recommendations

The development and improvement of assessment methods and criteria for the dented pipeline can be effectively achieved by the FE method. Specific numerical models are developed considering various working conditions including pressure fluctuations, corrosion and hydrogen embrittlement. Many limitations exist to be solved in this research and further research is proposed as shown below to provide more accurate and applicable guidance for dent assessment on pipelines.

(1) Only the spherical indenter was considered to produce the unconstrained plain dent on the pipeline and its dimension was kept consistent in different parts of this research. However, this simplification cannot completely represent dents with different shapes and sizes. In engineering,

the dent can be produced by the rock or excavation, of which the shape can be rectangular or wedge-shaped and the size can be large compared to the pipe's dimension. In addition, the process of denting is assumed to be slow enough for the steady state analysis in this work, while the natural dent is always generated by the impact of the external loads. The damage to the pipeline resulted from various denting process can be different and was not considered into this work.

Thus, further investigations should be carried out to improve the assessment methods to predict the performance condition and failure of dented pipelines based on other failure mechanisms. In addition, more work should be conducted on assessment of the pipelines containing other shapes and types of dents, such as constrained dents and kinked dents.

(2) Corrosion types are not discussed in this research such as the pitting, uniform and multiple corrosions, which have different geometric characteristics and strongly influence the local stress/strain distribution as well as the corrosion development. Furthermore, based on the M-E interaction theory, different work conditions of pipelines lead to various corrosion growth rates. Only the deoxygenated, near-neutral pH environment (i.e., the soil) was considered in this research to simulate the corrosion development on the buried pipelines. However, a large amount of pipelines service in the air and water, resulting in different corrosion conditions and growth patterns.

Therefore, in the future research, pressure capacity and corrosion defect growth on the dented pipelines where general corrosion or multiple corrosion defects are present should be further investigated. Corrosion with various geometric sizes and locations should be studied considering the mechanical-electrochemical interaction effect. For the pipeline operated in the air or water, more investigations should be carried out for the assessment of corrosion affected by the dent.

(3) Hydrogen embrittlement and diffusion of the dented pipelines are investigated based on theoretical assumptions and derivations in existing literature. In practice, hydrogen gas transportation using the existed pipelines is not widely applied and most of the research is carried out on the simulation and experimental measurements of small-scale specimens. Basic mechanisms for H atoms diffusion, HE and HIC of the pipeline steels are not clarified by the existing research. Besides, pipelines transporting the hydrogen gas can also encounter many types of defects such as corrosion, gouge, fatigue cracking and external impact, etc. Huge demand of hydrogen energy around the world requires more research to be proposed in this field.

Considering the methods and research that have been developed in this work, further studies can be carried out as follows. When the existing pipeline is repurposed to transport hydrogen, the amount of H atoms diffusing into the steel and the H atom concentrations at defects such as dents should be further quantified. In addition, a complete assessment system is required to predict the HIC on dented pipelines when transporting hydrogen. The effects of dent and corrosion on H atom concentration and the crack initiation and propagation should be quantitatively determined.

Reference

[1] G. Qin and Y.F. Cheng, A review on defect assessment of pipelines: Principles, numerical solutions, and applications, Int. J. Pres. Ves. Pip. (2021) 104329.

[2] Y. Shuai, X. Wang and Y.F. Cheng, Buckling resistance of an X80 steel pipeline at corrosion defect under bending moment, J. Nat. Gas Sci. Eng. 93 (2021) 104016.

[3] G. Qin and Y.F. Cheng, Failure pressure prediction by defect assessment and finite element modelling on natural gas pipelines under cyclic loading, J. Nat. Gas Sci. Eng. 81 (2020) 103445.

[4] C. Kim, L. Chen, H. Wang and H. Castaneda, Global and local parameters for characterizing and modeling external corrosion in underground coated steel pipelines: A review of critical factors, Journal of Pipeline Science and Engineering 1(1) (2021) 17-35.

[5] Y. Shuai, D. Zhou, X. Wang, H. Yin, S. Zhu, J. Li and Y.F. Cheng, Local buckling failure analysis of high strength pipelines containing a plain dent under bending moment, J. Nat. Gas Sci. Eng. 77 (2020) 103266.

[6] J. Capelle, J. Gilgert and G. Pluvinage, A fatigue initiation parameter for gas pipe steel submitted to hydrogen absorption, Int. J. Hydrogen Energ. 35(2) (2010) 833-843.

[7] R.M. Andrews, N. Gallon and O. Huising, Assessing damaged pipelines transporting hydrogen, Journal of Pipeline Science and Engineering 2(3) (2022) 100066.

[8] A. Dinovitzer, S. Tiku and M. Piazza, Dent Assessment and Management: API Recommended Practice 1183, pp. V1T-V3T (American Society of Mechanical Engineers, 2020).

[9] M. Durowoju, Y. Pu, S. Benson and J. Race, Fatigue assessment of pipeline with plain dents under cyclic pressure loading using finite element method, pp. V4T-V5T (American Society of Mechanical Engineers, 2016).

[10] P. Zhang, H. Lan, X. Dou, J. Wang and S. Zha, Review of load-bearing capacity of dented pipes under typical loads, Eng. Fail. Anal. 120 (2021) 105006.

[11] Y. Shuai, J. Shuai and X. Zhang, Experimental and numerical investigation of the strain response of a dented API 5L X52 pipeline subjected to continuously increasing internal pressure, J. Nat. Gas Sci. Eng. 56 (2018) 81-92.

[12] M. Allouti, C. Schmitt, G. Pluvinage, J. Gilgert and S. Hariri, Study of the influence of dent depth on the critical pressure of pipeline, Eng. Fail. Anal. 21 (2012) 40-51.

[13] M. Gao and R. Krishnamurthy. Mechanical Damage in Pipelines: A Review of the Methods and Improvements in Characterization, Evaluation, and Mitigation. Oil and Gas Pipelines, pp. 289-3262015).

[14] Y. Wu, J. Li and L. Li, Damage and springback analysis of two typical dented pipelines with different parameters, Journal of Pressure Vessel Technology 141(4) (2019) 41701.

[15] X. Zhu, A comparative study of burst failure models for assessing remaining strength of corroded pipelines, Journal of Pipeline Science and Engineering 1(1) (2021) 36-50.

[16] Z. Zhang, X. Ni and Y. Frank Cheng, Assessment by finite element modelling of the mechano-electrochemical interaction at double-ellipsoidal corrosion defect with varied inclinations on pipelines, Constr. Build. Mater. 260 (2020) 120459.

[17] J. Błachut and I.B. Iflefel, Experimental and numerical investigation of plain and gouged dents in steel pipes subjected to pressure and moment loading, Journal of pressure vessel technology 130(2) (2008) 21203.

[18] P. Zhao, J. Shuai, M. Sun, Z. Lv, K. Xu and Y. Wang, Burst pressure of thin-walled pipes with dent and gouge defects, Thin Wall. Struct. 159 (2021) 107213.

[19] L.Y. Xu and Y.F. Cheng, Development of a finite element model for simulation and prediction of mechanoelectrochemical effect of pipeline corrosion, Corros. Sci. 73 (2013) 150-160.

[20] R.F. Wright, E.R. Brand, M. Ziomek-Moroz, J.H. Tylczak and P.R. Ohodnicki Jr, Effect of HCO3− on electrochemical kinetics of carbon steel corrosion in CO2-saturated brines, Electrochim. Acta 290 (2018) 626-638.

[21] Y. Yang and Y.F. Cheng, Effect of stress on corrosion at crack tip on pipeline steel in a near-neutral ph solution, J. Mater. Eng. Perform. 25 (2016) 4988-4995.

[22] J. Sun and Y.F. Cheng, Modelling of mechano-electrochemical interaction of multiple longitudinally aligned corrosion defects on oil/gas pipelines, Eng. Struct. 190 (2019) 9-19.

[23] Y. Wang, L. Xu, J. Sun and Y.F. Cheng, Mechano-electrochemical interaction for pipeline corrosion: A review, Journal of Pipeline Science and Engineering 1(1) (2021) 1-16.

[24] L.Y. Xu and Y.F. Cheng, An experimental investigation of corrosion of X100 pipeline steel under uniaxial elastic stress in a near-neutral pH solution, Corros. Sci. 59 (2012) 103-109.

[25] J. Sun and Y.F. Cheng, Modelling of mechano-electrochemical interaction at overlapped corrosion defects and the implication on pipeline failure prediction, Eng. Struct. 212 (2020) 110466.

[26] M. Dinachandra and A. Alankar, Adaptive finite element modeling of phase-field fracture driven by hydrogen embrittlement, Comput. Method. Appl. M. 391 (2022) 114509.

[27] A. Laureys, E. Van den Eeckhout, R. Petrov and K. Verbeken, Effect of deformation and charging conditions on crack and blister formation during electrochemical hydrogen charging, Acta Mater. 127 (2017) 192-202.

[28] S.S. Shishvan, G. Csányi and V.S. Deshpande, Strain rate sensitivity of the hydrogen embrittlement of ferritic steels, Acta Mater. 257 (2023) 119173.

[29] E.S. Drexler, A.J. Slifka, R.L. Amaro, N. Barbosa, D.S. Lauria, L.E. Hayden and D.G. Stalheim, Fatigue crack growth rates of API X70 pipeline steel in a pressurized hydrogen gas environment, Fatigue Fract. Eng. M. 37(5) (2014) 517-525.

[30] E. Martínez-Pañeda, A. Golahmar and C.F. Niordson, A phase field formulation for hydrogen assisted cracking, Comput. Method. Appl. M. 342 (2018) 742-761.

[31] T. Das, R. Chakrabarty, J. Song and S. Yue, Understanding microstructural influences on hydrogen diffusion characteristics in martensitic steels using finite element analysis (FEA), Int. J. Hydrogen Energ. 47(2) (2022) 1343-1357.

[32] K.O. Findley, M.K. O'Brien and H. Nako, Critical Assessment 17: Mechanisms of hydrogen induced cracking in pipeline steels, Mater. Sci. Tech.-Lond. 31(14) (2015) 1673-1680.

[33] M.A. Mohtadi-Bonab, J.A. Szpunar, R. Basu and M. Eskandari, The mechanism of failure by hydrogen induced cracking in an acidic environment for API 5L X70 pipeline steel, Int. J. Hydrogen Energ. 40(2) (2015) 1096-1107.

[34] L.B. Peral, A. Zafra, S. Blasón, C. Rodríguez and J. Belzunce, Effect of hydrogen on the fatigue crack growth rate of quenched and tempered CrMo and CrMoV steels, Int. J. Fatigue 120 (2019) 201-214.

[35] Y. Sun and Y.F. Cheng, Thermodynamics of spontaneous dissociation and dissociative adsorption of hydrogen molecules and hydrogen atom adsorption and absorption on steel under pipelining conditions, Int. J. Hydrogen Energ. 46(69) (2021) 34469-34486.

[36] R.W. Revie, Oil and gas pipelines: Integrity and safety handbook, (John Wiley & Sons, 2015).

[37] T.H. Hyde, R. Luo and A.A. Becker, Force‐deflection analysis of offset indentations on pressurised pipes, Int. J. Pres. Ves. Pip. 84(6) (2007) 368-377.

[38] A.K. Abdelmoety, M. Kainat, N. Yoosef-Ghodsi, Y. Li and S. Adeeb, Strain-based reliability analysis of dented pipelines using a response surface method, Journal of Pipeline Science and Engineering 2(1) (2022) 29-38.

[39] J.H. Liu and A. Francis, Theoretical analysis of local indentation on pressured pipes, Int. J. Pres. Ves. Pip. 81(12) (2004) 931-939.

[40] S.J. Dawson, A. Russell and A. Patterson, Emerging techniques for enhanced assessment and analysis of dents. International Pipeline Conference, pp. 397-4152006).

[41] X. Tian and H. Zhang, Failure criterion of buried pipelines with dent and scratch defects, Eng. Fail. Anal. 80 (2017) 278-289.

[42] M. Bernard, J. Fontanabona, V. Gaffard, D. Popineau and P. Wiet, Empreinte: New Horizons for Pipelines Integrity Assessment, (Offshore Technology Conference, 2013).

[43] J. Dawson, I. Murray and J. Hedger, Techniques for the enhanced assessment of pipeline dents., Journal of Pipeline Engineering 17 (2018) 127-135.

[44] K.F. Tee and A.H. Wordu, Burst strength analysis of pressurized steel pipelines with corrosion and gouge defects, Eng. Fail. Anal. 108 (2020) 104347.

[45] D.B. Noronha, R.R. Martins, B.P. Jacob and E. de Souza, Procedures for the strain based assessment of pipeline dents, Int. J. Pres. Ves. Pip. 87(5) (2010) 254-265.

[46] Y. Wu, N. Tang and P. Zhang, The comparison of dented pipeline displacement calculation methods, Eng. Fail. Anal. 57 (2015) 562-573.

[47] S.M. Adeeb and D.J. Horsley, A numerical procedure to establish a safe working pressure during excavation of a pipeline in a rock ditch, Int. J. Pres. Ves. Pip. 83(7) (2006) 488-497.

[48] U. Arumugam, M. Gao, R. Krishnamurthy, R. Wang and R. Kania, Study of safe dig pressure level for rock dents in gas pipelines. International Pipeline Conference, pp. V1T-V3T (American Society of Mechanical Engineers, 2018).

[49] S.A. Lukasiewicz, J.A. Czyz, C. Sun and S. Adeeb, Calculation of strains in dents based on high resolution in-line caliper survey. International Pipeline Conference, pp. 129-134Calgary, Alberta, Canada, 2006).

[50] J.B. Choi, B.K. Goo, J.C. Kim, Y.J. Kim and W.S. Kim, Development of limit load solutions for corroded gas pipelines, Int. J. Pres. Ves. Pip. 80(2) (2003) 121-128.

[51] H. Ghaednia, S. Das, R. Wang and R. Kania, Effect of operating pressure and dent depth on burst strength of NPS30 linepipe with dent – crack defect, Journal of Offshore Mechanics and Arctic Engineering 137(3) (2015).

[52] H. Ghaednia, S. Das, R. Wang and R. Kania, Safe burst strength of a pipeline with dent – crack defect: effect of crack depth and operating pressure, Eng. Fail. Anal. 55 (2015) 288-299.

[53] B.C. Mondal and A.S. Dhar, Finite-element evaluation of burst pressure models for corroded pipelines, Journal of Pressure Vessel Technology 139(2) (2017).

[54] Z. Shengzhu, C. Frank, F. Xiaodong, W. Lijun, W. Rujun, D. Yingquan and H. Yuxin, Performance characteristics and technical challenges of X80 pipeline steel, Oil & Gas Storage and Transportation 38(5) (2019) 481-495.

[55] M. Xie and Z. Tian, A review on pipeline integrity management utilizing in-line inspection data, Eng. Fail. Anal. 92 (2018) 222-239.

[56] R. Amaya-Gómez, M. Sánchez-Silva, E. Bastidas-Arteaga, F. Schoefs and F. Munoz, Reliability assessments of corroded pipelines based on internal pressure – A review, Eng. Fail. Anal. 98 (2019) 190-214.

[57] J. Gossard, J. Bratton, D. Kemp, S. Finneran and S.J. Polasik, Evaluating dents with metal loss using finite element analysis. International Pipeline Conference, pp. V1T-V3T (American Society of Mechanical Engineers, 2016).

[58] H.O. Heggen, J. Bratton, D. Kemp, J. Liu and J. Austin, Fitness for Service of Dents Associated with Metal Loss Due to Corrosion. Proceedings of the 2014 10th International Pipeline Conference, pp. V2T-V6T (American Society of Mechanical Engineers, Calgary, Alberta, Canada, 2014).

[59] D. Hou, D. Zeng, T. Shi, Z. Zhang and W. Deng, The effects of sulfide stress cracking on the mechanical properties and intergranular cracking of P110 casing steel in sour environments, Petrol. Sci. 10 (2013) 385-394.

[60] B. Meng, C. Gu, L. Zhang, C. Zhou, X. Li, Y. Zhao, J. Zheng, X. Chen and Y. Han, Hydrogen effects on X80 pipeline steel in high-pressure natural gas/hydrogen mixtures, Int. J. Hydrogen Energ. 42(11) (2017) 7404-7412.

[61] T.T. Nguyen, N. Tak, J. Park, S.H. Nahm and U.B. Beak, Hydrogen embrittlement susceptibility of X70 pipeline steel weld under a low partial hydrogen environment, Int. J. Hydrogen Energ. 45(43) (2020) 23739-23753.

[62] J.A. Ronevich and C. San Marchi, Materials compatibility concerns for hydrogen blended into natural gas. Pressure Vessels and Piping Conference, pp. V4T-V6T (American Society of Mechanical Engineers, 2021).

[63] H. Wang, Z. Tong, G. Zhou, C. Zhang, H. Zhou, Y. Wang and W. Zheng, Research and demonstration on hydrogen compatibility of pipelines: a review of current status and challenges, Int. J. Hydrogen Energ. 47(66) (2022) 28585-28604.

[64] K. Liu, G. Chen, Y. Chang, B. Zhu, X. Liu and B. Han, Nonlinear dynamic analysis and fatigue damage assessment for a deepwater test string subjected to random loads, Petrol. Sci. 13 (2016) 126-134.

[65] X. Gu, X. Zang, Z. Zhang, P. Yang, W. Miao, P. Cao and B. Zhao, Reliability analysis of large-diameter high-grade-steel natural gas pipelines under fault action, Petrol. Sci. 19(5) (2022) 2387-2398.

[66] E. Ohaeri, U. Eduok and J. Szpunar, Hydrogen related degradation in pipeline steel: A review, Int. J. Hydrogen Energ. 43(31) (2018) 14584-14617.

[67] S. Zhang, L. Qi, S. Liu, Z. Peng, Y.F. Cheng, F. Huang and J. Liu, Synergistic effects of Nb and Mo on hydrogen-induced cracking of pipeline steels: A combined experimental and numerical study, J. Mater. Sci. Technol. 158 (2023) 156-170.

[68] M. Dadfarnia, P. Sofronis, J. Brouwer and S. Sosa, Assessment of resistance to fatigue crack growth of natural gas line pipe steels carrying gas mixed with hydrogen, Int. J. Hydrogen Energ. 44(21) (2019) 10808-10822.

[69] E.V. Chatzidouros, V.J. Papazoglou, T.E. Tsiourva and D.I. Pantelis, Hydrogen effect on fracture toughness of pipeline steel welds, with in situ hydrogen charging, Int. J. Hydrogen Energ. 36(19) (2011) 12626-12643.

[70] A. Laureys, R. Depraetere, M. Cauwels, T. Depover, S. Hertelé and K. Verbeken, Use of existing steel pipeline infrastructure for gaseous hydrogen storage and transport: A review of factors affecting hydrogen induced degradation, J. Nat. Gas Sci. Eng. 101 (2022) 104534.

[71] M. Isfandbod and E. Martínez-Pañeda, A mechanism-based multi-trap phase field model for hydrogen assisted fracture, Int. J. Plasticity 144 (2021) 103044.

[72] J. Kec and I. Cerny, Stress-strain assessment of dents in wall of high pressure gas pipeline, Procedia Structural Integrity 5 (2017) 340-346.

[73] X. Tian, M. Lu and Y. Chen, Numerical Simulation Method for Failure Pressure of Buried Dented Pipeline, Journal of Failure Analysis and Prevention 20 (2020) 944-949.

[74] K.A. Macdonald, A. Cosham, C.R. Alexander and P. Hopkins, Assessing mechanical damage in offshore pipelines – Two case studies, Eng. Fail. Anal. 14(8) (2007) 1667-1679.

[75] K.A. Macdonald and A. Cosham, Best practice for the assessment of defects in pipelines – gouges and dents, Eng. Fail. Anal. 12(5) (2005) 720-745.

[76] M.R. Shaik, Pipeline Integrity Assessment: Methodology, pp. V1T-V3T (American Society of Mechanical Engineers Digital Collection, 2015).

[77] American Society of Mechanical Engineers, Gas Transmission and Distribution Piping Systems. ASME B31 (2016) 8, 2016).

[78] M. Gao, R. McNealy, R. Krishnamurthy and I. Colquhoun, Strain-based models for dent assessment: a review, pp. 823-8302008).

[79] B.N. Leis, Evolution of metal-loss severity criteria: Gaps and a path forward, Journal of Pipeline Science and Engineering 1(1) (2021) 51-62.

[80] A. Cosham and P. Hopkins, The assessment of corrosion in pipelines – Guidance in the pipeline defect assessment manual (PDAM). Pipeline Pigging and Integrity Management Conference, pp. 17-18Amsterdam, The Netherlands, 2004).

[81] J. Shuai, C.E. Zhang, F. Chen and R. He, Prediction of Failure Pressure of Corroded Pipelines Based on Finite Element Analysis, pp. 375-3812008).

[82] V. Babbar and L. Clapham, Finite Element Modeling of Magnetic Flux Leakage Signals from Mechanical Damage Containing Corrosion Pits. AIP Conference Proceedings, pp. 453-458 (American Institute of Physics, 2009).

[83] K.M. Hafez, The role of a plain dent on the failure mode of a crude oil pipeline, Eng. Fail. Anal. 122 (2021) 105291.

[84] Y. Shuai, J. Shuai and K. Xu, Probabilistic analysis of corroded pipelines based on a new failure pressure model, Eng. Fail. Anal. 81 (2017) 216-233.

[85] A. Okodi, M. Lin, N. Yoosef-Ghodsi, M. Kainat, S. Hassanien and S. Adeeb, Crack propagation and burst pressure of longitudinally cracked pipelines using extended finite element method, Int. J. Pres. Ves. Pip. 184 (2020) 104115.

[86] A. Okodi, Y. Li, J. Cheng, M. Kainat, N. Yoosef-Ghodsi and S. Adeeb, Effect of location of crack in dent on burst pressure of pipeline with combined dent and crack defects, Journal of Pipeline Science and Engineering 1(2) (2021) 252-263.

[87] B. Bedairi, D. Cronin, A. Hosseini and A. Plumtree, Failure prediction for Crack-in-Corrosion defects in natural gas transmission pipelines, Int. J. Pres. Ves. Pip. 96-97 (2012) 90-99.

[88] American Petroleum Institute, Fitness For Service API 579-1/ASME FFS-1, (2016).

[89] H. Ghaednia, J. Silva, S. Kenno, S. Das, R. Wang and R. Kania, Pressure Tests on 30-in. Diameter X65 Grade Pipes With Dent – Crack Defects, J. Pipeline Eng. 12(1) (2013) 61-67.

[90] C.R. Alexander, Review of experimental and analytical investigations of dented pipelines, ASME-PUBLICATIONS-PVP 395 (1999) 197-210.

[91] N.E. Nanninga, Y.S. Levy, E.S. Drexler, R.T. Condon, A.E. Stevenson and A.J. Slifka, Comparison of hydrogen embrittlement in three pipeline steels in high pressure gaseous hydrogen environments, Corros. Sci. 59 (2012) 1-9.

[92] J. Yamabe, O. Takakuwa, H. Matsunaga, H. Itoga and S. Matsuoka, Hydrogen diffusivity and tensile-ductility loss of solution-treated austenitic stainless steels with external and internal hydrogen, Int. J. Hydrogen Energ. 42(18) (2017) 13289-13299.

[93] C. Fischer, S. Fliegener, H. Oesterlin, T. Michler, S. Höhler, A. Mondry and P. Ertault De La Bretonniere, Codes and standards for the fatigue-based design of hydrogen infrastructure components, Int. J. Fatigue 171 (2023) 107564.

[94] J. Kittel, J.W. Martin, T. Cassagne and C. Bosch, Hydrogen induced cracking (HIC)-Laboratory testing assessment of low alloy steel linepipe. NACE CORROSION, p. 8110 (NACE, 2008).

[95] The American Society Of Engineers, Hydrogen Piping and Pipelines, ASME B31.12, U.S.A, (2019).

[96] A.N. Md Rafi, S. Das, H. Ghaednia, J. Silva, R. Kania and R. Wang, Revisiting ASME strain-based dent evaluation criterion, Journal of pressure vessel technology 134(4) (2012).

[97] Y. Shuai, X. Wang, J. Shuai, Y. Zhao, X. Zhang and C. Tang, Mechanical behavior investigation on the formation of the plain dent of an API 5L L245 pipeline subjected to concentrated lateral load, Eng. Fail. Anal. 108 (2020) 104189.

[98] M.M. Shahzamanian, M. Kainat, N. Yoosef-Ghodsi and S. Adeeb, Systematic literature review of the application of extended finite element method in failure prediction of pipelines, Journal of Pipeline Science and Engineering 1(2) (2021) 241-251.

[99] R.A. Alashti, S. Jafari and S.J. Hosseinipour, Experimental and numerical investigation of ductile damage effect on load bearing capacity of a dented API XB pipe subjected to internal pressure, Eng. Fail. Anal. 47 (2015) 208-228.

[100] M. Oyane, T. Sato, K. Okimoto and S. Shima, Criteria for ductile fracture and their applications, Journal of Mechanical Working Technology 4(1) (1980) 65-81.

[101] Y. Wu, J. Xiao and P. Zhang, The analysis of damage degree of oil and gas pipeline with type II plain dent, Eng. Fail. Anal. 66 (2016) 212-222.

[102] W. Ying, Q. Cheng-zhi, M. Yu and L. Wu, Displacement Analysis and Comparison of Lateral and Axial Typical Dent on Pipeline Based on FE Calculation, Information Technology Journal 12(24) (2013) 8212.

[103] C. Li and S. Dang, Plastic damage analysis of oil and gas pipelines with unconstrained and constrained dents, Eng. Fail. Anal. 77 (2017) 39-49.

[104] U. Arumugam, M. Gao, R. Krishnamurthy, R. Wang and R. Kania, Study of a Plastic Strain Limit Damage Criterion for Pipeline Mechanical Damage using FEA and Full-Scale Denting Tests. Proceedings of the 2016 11th International Pipeline Conference, pp. V1T-V3T (American Society of Mechanical Engineers, Calgary, Alberta, Canada, 2016).

[105] X. Liu, H. Zhang, W. Baodong, X. Mengying, T. Kai and W.U. Kai, Nonlinear finite element analysis of the limit state and pressure of dented X60 steel pipeline, Mechanics 23(6) (2017) 814-819.

[106] J. Baek, Y. Kim, W. Kim, J. Koo and C. Seok, Load bearing capacity of API X65 pipe with dent defect under internal pressure and in-plane bending, Materials Science and Engineering: A 540 (2012) 70-82.

[107] S.B. Cunha, I.P. Pasqualino and B.C. Pinheiro, Pipeline plain dent fatigue: A comparison of assessment methodologies. International Pipeline Conference, pp. V2T-V6T (American Society of Mechanical Engineers, 2014).

[108] B.C. Mondal and A.S. Dhar, Improved Folias factor and burst pressure models for corroded pipelines, Journal of Pressure Vessel Technology 140(1) (2018).

[109] K.J. Yeom, Y. Lee, K.H. Oh and W.S. Kim, Integrity assessment of a corroded API X70 pipe with a single defect by burst pressure analysis, Eng. Fail. Anal. 57 (2015) 553-561.

[110] K.U. Amandi, E.O. Diemuodeke and T.A. Briggs, Model for remaining strength estimation of a corroded pipeline with interacting defects for oil and gas operations, Cogent Engineering 6(1) (2019) 1663682.

[111] X. Tang and Y.F. Cheng, Micro-electrochemical characterization of the effect of applied stress on local anodic dissolution behavior of pipeline steel under near-neutral pH condition, Electrochim. Acta 54(5) (2009) 1499-1505.

[112] H.B. Xue and Y.F. Cheng, Electrochemical corrosion behavior of X80 pipeline steel in a near‐neutral pH solution, Materials and corrosion 61(9) (2010) 756-761.

[113] A.N.M. Rafi, Structural Behaviour of Dented Pipelines, (2011).

[114] H. Ghaednia, K. Gerard, S. Bhattacharjee and S. Das, Behavior of NPS30 pipe subject to denting load. Proceedings of the ASME 2014 International Mechanical Engineering Congress and Exposition, pp. V9T-V12T (American Society of Mechanical Engineers, Montreal, Quebec, Canada, 2014).

[115] J. Oshana Jajo, Dent behaviour of steel pipes under pressure load, (2014).

[116] A. Cosham, P. Hopkins and K.A. Macdonald, Best practice for the assessment of defects in pipelines – Corrosion, Eng. Fail. Anal. 14(7) (2007) 1245-1265.

[117] J. Bao and W. Zhou, Influence of depth thresholds and interaction rules on the burst capacity evaluation of naturally corroded pipelines, Journal of Pipeline Science and Engineering 1(1) (2021) 148-165.

[118] B. Sobhaniaragh, S.H. Afzalimir and C. Ruggieri, Towards the prediction of hydrogen‐induced crack growth in high‐graded strength steels, Thin Wall. Struct. 159 (2021) 107245.

[119] I.M. Dmytrakh, R.L. Leshchak, A.M. Syrotyuk and R.A. Barna, Effect of hydrogen concentration on fatigue crack growth behaviour in pipeline steel, Int. J. Hydrogen Energ. 42(9) (2017) 6401-6408.

[120] A.J. Slifka, E.S. Drexler, R.L. Amaro, L.E. Hayden, D.G. Stalheim, D.S. Lauria and N.W. Hrabe, Fatigue measurement of pipeline steels for the application of transporting gaseous hydrogen, Journal of Pressure Vessel Technology 140(1) (2018).

[121] V. Singh, R. Singh, K.S. Arora and D.K. Mahajan, Hydrogen induced blister cracking and mechanical failure in X65 pipeline steels, Int. J. Hydrogen Energ. 44(39) (2019) 22039-22049.

[122] T. An, S. Zhang, M. Feng, B. Luo, S. Zheng, L. Chen and L. Zhang, Synergistic action of hydrogen gas and weld defects on fracture toughness of X80 pipeline steel, Int. J. Fatigue 120 (2019) 23-32.

[123] L. Briottet, I. Moro and P. Lemoine, Quantifying the hydrogen embrittlement of pipeline steels for safety considerations, Int. J. Hydrogen Energ. 37(22) (2012) 17616-17623.

[124] T. An, S. Zheng, H. Peng, X. Wen, L. Chen and L. Zhang, Synergistic action of hydrogen and stress concentration on the fatigue properties of X80 pipeline steel, Materials Science and Engineering: A 700 (2017) 321-330.

[125] R. Fernández-Sousa, C. Betegón and E. Martínez-Pañeda, Analysis of the influence of microstructural traps on hydrogen assisted fatigue, Acta Mater. 199 (2020) 253-263.

[126] A. Rajabipour and R.E. Melchers, Application of Paris' law for estimation of hydrogen-assisted fatigue crack growth, Int. J. Fatigue 80 (2015) 357-363.

[127] T.T. Nguyen, H.M. Heo, J. Park, S.H. Nahm and U.B. Beak, Fracture properties and fatigue life assessment of API X70 pipeline steel under the effect of an environment containing hydrogen, J. Mech. Sci. Technol. 35(4) (2021) 1445-1455.

[128] X. Zhu and R. Wang, Effect of residual stress or plastic deformation history on fatigue life simulation of pipeline dents. Proceedings of the 2018 12th International Pipeline Conference, pp. V1T-V3T (American Society of Mechanical Engineers, Calgary, Alberta, Canada, 2018).

[129] M. Kainat, J. Woo, D. Langer, T. Krausert, J.R. Cheng, S. Hassanien and S. Adeeb, Effects of loading sequences on remaining life of plain dents in buried liquid pipelines, Journal of Pipeline Systems Engineering and Practice 10(2) (2019) 4019001.

[130] B. Pinheiro, C.G. Soares and I. Pasqualino, Generalized expressions for stress concentration factors of pipeline plain dents under cyclic internal pressure, Int. J. Pres. Ves. Pip. 170 (2019) 82-91.

[131] C. Han, S. Tan, J. Zhang and C. Zhang, Simulation investigation of dent behavior of steel pipe under external load, Eng. Fail. Anal. 90 (2018) 341-354.

[132] P. Zhao, J. Shuai, Z. Lv and K. Xu, Strain response of API 5L X80 pipeline subjected to indentation, Appl. Ocean Res. 94 (2020) 101991.

[133] B. Ma, J. Shuai, D. Liu and K. Xu, Assessment on failure pressure of high strength pipeline with corrosion defects, Eng. Fail. Anal. 32 (2013) 209-219.

[134] H. Ghaednia, S. Das, R. Wang and R. Kania, Effect of dent depth on the burst pressure of NPS30 X70 pipes with dent-crack defect. Proceedings of the 2014 10th International Pipeline

Conference, pp. V2T-V6T (American Society of Mechanical Engineers, Calgary, Alberta, Canada, 2014).

[135] A. Okodi, Burst Pressure of Pipeline with Longitudinal Crack in Dent Defects Using Extended Finite Element Method, (2021).

[136] S. Del Busto, C. Betegón and E. Martínez-Pañeda, A cohesive zone framework for environmentally assisted fatigue, Eng. Fract. Mech. 185 (2017) 210-226.

[137] X. Zhuang, S. Zhou, G.D. Huynh, P. Areias and T. Rabczuk, Phase field modeling and computer implementation: A review, Eng. Fract. Mech. 262 (2022) 108234.

[138] L. Chen, T. Rabczuk, S.P.A. Bordas, G.R. Liu, K.Y. Zeng and P. Kerfriden, Extended finite element method with edge-based strain smoothing (ESm-XFEM) for linear elastic crack growth, Comput. Method. Appl. M. 209-212 (2012) 250-265.

[139] S. Kingklang, W. Daodon and V. Uthaisangsuk, Failure investigation of liquefied petroleum gas cylinder using FAD and XFEM, Int. J. Pres. Ves. Pip. 171 (2019) 69-78.

[140] W. Zhou, B. Liu, Q. Wang, X. Chang and X. Chen, Formulations of displacement discontinuity method for crack problems based on boundary element method, Eng. Anal. Bound. Elem. 115 (2020) 86-95.

[141] M. Ambati, R. Kruse and L. De Lorenzis, A phase-field model for ductile fracture at finite strains and its experimental verification, Comput. Mech. 57 (2016) 149-167.

[142] A. Díaz, J.M. Alegre, I.I. Cuesta, E. Martínez-Pañeda and Z. Zhang, Notch fracture predictions using the Phase Field method for Ti-6Al-4V produced by Selective Laser Melting after different post-processing conditions, Theor. Appl. Fract. Mec. 121 (2022) 103510.

[143] A. Valverde-González, E. Martínez-Pañeda, A. Quintanas-Corominas, J. Reinoso and M. Paggi, Computational modelling of hydrogen assisted fracture in polycrystalline materials, Int. J. Hydrogen Energ. 47(75) (2022) 32235-32251.

[144] W. Huber and M. Asle Zaeem, A mixed mode phase-field model of ductile fracture, J. Mech. Phys. Solids 171 (2023) 105123.

[145] D. Wang, F. Ma and H. Chen, Numerical Simulation for Hydrogen-Assisted Cracking: An Explicit Phase-Field Formulation, Materials 16(4) (2023) 1708.

[146] G. Dal Maso and R. Toader, A Model for the Quasi-Static Growth¶ of Brittle Fractures:¶ Existence and Approximation Results, Arch. Ration. Mech. An. 162 (2002) 101-135.

[147] J. Wu, A unified phase-field theory for the mechanics of damage and quasi-brittle failure, J. Mech. Phys. Solids 103 (2017) 72-99.

[148] C. Miehe, M. Hofacker and F. Welschinger, A phase field model for rate-independent crack propagation: Robust algorithmic implementation based on operator splits, Comput. Method. Appl. M. 199(45) (2010) 2765-2778.

[149] M.J. Borden, T.J. Hughes, C.M. Landis, A. Anvari and I.J. Lee, A phase-field formulation for fracture in ductile materials: Finite deformation balance law derivation, plastic degradation, and stress triaxiality effects, Comput. Method. Appl. M. 312 (2016) 130-166.

[150] M. Ambati, T. Gerasimov and L. De Lorenzis, Phase-field modeling of ductile fracture, Comput. Mech. 55 (2015) 1017-1040.

[151] G. Molnár, A. Gravouil, R. Seghir and J. Réthoré, An open-source Abaqus implementation of the phase-field method to study the effect of plasticity on the instantaneous fracture toughness in dynamic crack propagation, Comput. Method. Appl. M. 365 (2020) 113004.

[152] J. Fang, C. Wu, T. Rabczuk, C. Wu, C. Ma, G. Sun and Q. Li, Phase field fracture in elasto-plastic solids: Abaqus implementation and case studies, Theor. Appl. Fract. Mec. 103 (2019) 102252.

[153] M. Tingxia, W. Jinqiang, T. Yu, H. Hao and L. Anjun, Maximum suspended length of production pipeline, Journal of Southwest Petroleum University (Science & Technology Edition) 34(4) (2012) 165.

[154] P. Roovers, M.R. Galli, R.J. Bood, U. Marewski, M. Steiner and M. Zarea, EPRG methods for assessing the tolerance and resistance of pipelines to external damage. Pt. 1, 3R. Rohre, Rohrleitungsbau, Rohrleitungstransport 38 (1999).

[155] U. Arumugam, M. Gao, R. Krishnamurthy, R. Wang and R. Kania, Root cause analysis of dent with crack: a case study. Proceedings of the 2012 9th International Pipeline Conference, pp. 735-746 (American Society of Mechanical Engineers, Calgary, Alberta, Canada, 2012).

[156] R.Y. Wang, R. Kania, U. Arumugam and M. Gao, A combined approach to characterization of dent with metal loss. Proceedings of the 2012 9th International Pipeline Conference, pp. 209-216 (American Society of Mechanical Engineers, Calgary, Alberta, Canada, 2012).

[157] M. Witek, Possibilities of using X80, X100, X120 high-strength steels for onshore gas transmission pipelines, J. Nat. Gas Sci. Eng. 27 (2015) 374-384.

[158] Y.Z. Jia, J.Q. Wang, E.H. Han and W. Ke, Stress corrosion cracking of X80 pipeline steel in near-neutral pH environment under constant load tests with and without preload, J. Mater. Sci. Technol. 27(11) (2011) 1039-1046.

[159] S. Zhang and W. Zhou, Assessment of effects of idealized defect shape and width on the burst capacity of corroded pipelines, Thin Wall. Struct. 154 (2020) 106806.

[160] S. Zhang and W. Zhou, Development of a burst capacity model for corroded pipelines considering corrosion defect width and a revised Folias factor equation, J. Nat. Gas Sci. Eng. 88 (2021) 103812.

[161] L.Y. Xu and Y.F. Cheng, Corrosion of X100 pipeline steel under plastic strain in a neutral pH bicarbonate solution, Corros. Sci. 64 (2012) 145-152.

[162] X. Zhang, B. Chen and C. Guedes Soares, Effect of non-symmetrical corrosion imperfection on the collapse pressure of subsea pipelines, Mar. Struct. 73 (2020) 102806.

[163] M. Fahed, I. Barsoum, A. Alfantazi and M.D. Islam, Burst pressure prediction of pipes with internal corrosion defects, Journal of Pressure Vessel Technology 142(3) (2020) 31801.

[164] J. Sun, Y.F. Cheng, J. Woo, M. Kainat and S. Hassanien, Assessment of Interaction Between a Dent and an Adjacent Corrosion Feature on Pipelines and the Effect on Pipeline Failure Pressure by Finite-Element Modeling, Journal of Pipeline Systems Engineering and Practice 12(3) (2021) 4021029.

[165] W. Ramberg and W.R. Osgood, Description of stress-strain curves by three parameters, 1943).

[166] J. Freire, R.D. Vieira, J. Castro and A.C. Benjamin, Part 3: Burst tests of pipeline with extensive longitudinal metal loss, Exp. Techniques 30(6) (2006) 60-65.

[167] J. Sun and Y.F. Cheng, Assessment by finite element modeling of the interaction of multiple corrosion defects and the effect on failure pressure of corroded pipelines, Eng. Struct. 165 (2018) 278-286.

[168] J. Zhao and Y.F. Cheng, A new criterion based on strain determination for dent assessment of pipelines, Journal of Pipeline Science and Engineering (2021).

[169] C. Oh, Y. Kim, J. Baek, Y. Kim and W. Kim, Ductile failure analysis of API X65 pipes with notch-type defects using a local fracture criterion, Int. J. Pres. Ves. Pip. 84(8) (2007) 512-525.

[170] G. Fekete and L. Varga, The effect of the width to length ratios of corrosion defects on the burst pressures of transmission pipelines, Eng. Fail. Anal. 21 (2012) 21-30.

[171] E.R. Lancaster and S.C. Palmer, Burst pressures of pipes containing dents and gouges, Proceedings of the Institution of Mechanical Engineers, Part E: Journal of Process Mechanical Engineering 210(1) (1996) 19-27.

[172] M. Zarea, R. Batisse, B. Leis, P. Cardin and G. Vignal, Full scale experimental database of dent and gouge defects to improve burst and fatigue strength models of pipelines. International Gas Union Research Conference, pp. 845-861 (American Society of Mechanical Engineers, 2011).

[173] C. Alexander and K. Brownlee, Methodology for assessing the effects of plain dents, wrinkle bends, and mechanical damage on pipeline integrity. NACE CORROSION, p. 7139 (NACE, 2007).

[174] A. Valor, F. Caleyo, J.M. Hallen and J.C. Velázquez, Reliability assessment of buried pipelines based on different corrosion rate models, Corros. Sci. 66 (2013) 78-87.

[175] F. Caleyo, J.C. Velázquez, A. Valor and J.M. Hallen, Probability distribution of pitting corrosion depth and rate in underground pipelines: A Monte Carlo study, Corros. Sci. 51(9) (2009) 1925-1934.

[176] J.C. Vela´zquez, F. Caleyo, A. Valor and J.M. Hallen, Predictive Model for Pitting Corrosion in Buried Oil and Gas Pipelines, Corrosion 65(5) (2009) 332-342.

[177] L.Y. Xu and Y.F. Cheng, Reliability and failure pressure prediction of various grades of pipeline steel in the presence of corrosion defects and pre-strain, Int. J. Pres. Ves. Pip. 89 (2012) 75-84.

[178] Y.F. Cheng, Stress corrosion cracking of pipelines, (John Wiley & Sons, 2013).

[179] E.M. Gutman, Mechanochemistry of solid surfaces, (World Scientific Publishing Company, 1994).

[180] J. Sun and Y.F. Cheng, Investigation by numerical modeling of the mechano-electrochemical interaction of circumferentially aligned corrosion defects on pipelines, Thin Wall. Struct. 144 (2019) 106314.

[181] Y. Huang, P. Zhang and G. Qin, Investigation by numerical modeling of the mechano-electrochemical interaction at a dent-corrosion defect on pipelines, Ocean Eng. 256 (2022) 111402.

[182] P. Novak, R. Yuan, B.P. Somerday, P. Sofronis and R.O. Ritchie, A statistical, physical-based, micro-mechanical model of hydrogen-induced intergranular fracture in steel, J. Mech. Phys. Solids 58(2) (2010) 206-226.

[183] R.A. Oriani and P.H. Josephic, Equilibrium aspects of hydrogen-induced cracking of steels, Acta metallurgica 22(9) (1974) 1065-1074.

[184] Y. Charles, H.T. Nguyen and M. Gaspérini, FE simulation of the influence of plastic strain on hydrogen distribution during an U-bend test, Int. J. Mech. Sci. 120 (2017) 214-224.

[185] A. Díaz, J.M. Alegre and I.I. Cuesta, Coupled hydrogen diffusion simulation using a heat transfer analogy, Int. J. Mech. Sci. 115 (2016) 360-369.

[186] Y. Sun and Y.F. Cheng, Hydrogen-induced degradation of high-strength steel pipeline welds: A critical review, Eng. Fail. Anal. (2021) 105985.

[187] W.D. Callister and D.G. Rethwisch, Materials science and engineering: an introduction, (wiley New York, 2018).

[188] M. Dadfarnia, P. Sofronis and T. Neeraj, Hydrogen interaction with multiple traps: can it be used to mitigate embrittlement? Int. J. Hydrogen Energ. 36(16) (2011) 10141-10148.

[189] B.D.C. Pinheiro and I.P. Pasqualino, Fatigue analysis of damaged steel pipelines under cyclic internal pressure, Int. J. Fatigue 31(5) (2009) 962-973.

[190] J. Freire, V. Paiva, G. Gonzáles, R.D. Vieira, J.E. Maneschy, A. D Almeida and A.S. Ribeiro, Fatigue assessment and monitoring of a dented pipeline specimen. Pressure Vessels and Piping Conference, p. V1T (American Society of Mechanical Engineers, 2019).

[191] B. Pinheiro, I. Pasqualino and S. Cunha, Fatigue life assessment of damaged pipelines under cyclic internal pressure: Pipelines with longitudinal and transverse plain dents, Int. J. Fatigue 68 (2014) 38-47.

[192] S. Tiku, V. Semiga, A. Dinovitzer and G. Vignal, Full scale cyclic fatigue testing of dented Pipelines and development of a Validated Dented Pipe Finite Element Model. International Pipeline Conference, pp. 693-702 (American Society of Mechanical Engineers, 2012).

[193] Z. He and W. Zhou, Fatigue reliability analysis of dented pipelines, Journal of Pipeline Science and Engineering 1(3) (2021) 290-297.

[194] G. Pluvinage, J. Capelle and M.H. Meliani, Pipe networks transporting hydrogen pure or blended with natural gas, design and maintenance, Eng. Fail. Anal. 106 (2019) 104164.

[195] D. Zhou, T. Li, D. Huang, Y. Wu, Z. Huang, W. Xiao, Q. Wang and X. Wang, The experiment study to assess the impact of hydrogen blended natural gas on the tensile properties and damage mechanism of X80 pipeline steel, Int. J. Hydrogen Energ. 46(10) (2021) 7402-7414.

[196] Y. Sun, Y. Ren and Y.F. Cheng, Dissociative adsorption of hydrogen and methane molecules at high-angle grain boundaries of pipeline steel studied by density functional theory modeling, Int. J. Hydrogen Energ. 47(97) (2022) 41069-41086.

[197] A. Alvaro, V. Olden, A. Macadre and O.M. Akselsen, Hydrogen embrittlement susceptibility of a weld simulated X70 heat affected zone under H2 pressure, Materials science and engineering: A 597 (2014) 29-36.

[198] W. Zhao, T. Zhang, Y. Zhao, J. Sun and Y. Wang, Hydrogen permeation and embrittlement susceptibility of X80 welded joint under high-pressure coal gas environment, Corros. Sci. 111 (2016) 84-97.

[199] R. Valentini, M. De Sanctis, G. Lovicu and C. Colombo, Helios—A New Method for Hydrogen Permeation Test. Proceedings of the 5th International Conference on Hydrogen Safety, Brussels, Belgium, pp. 9-112013).

[200] V. Olden, A. Saai, L. Jemblie and R. Johnsen, FE simulation of hydrogen diffusion in duplex stainless steel, Int. J. Hydrogen Energ. 39(2) (2014) 1156-1163.

[201] I. Khader, D. Kürten, R. Raga, N. Winzer and A. Kailer, Modeling hydrogen diffusion in a tribological scenario: A failure analysis of a thrust bearing, Wear 438 (2019) 203054.

[202] O. Barrera, E. Tarleton, H.W. Tang and A. Cocks, Modelling the coupling between hydrogen diffusion and the mechanical behaviour of metals, Comp. Mater. Sci. 122 (2016) 219-228.

[203] X. Zhu and B.N. Leis, Finite element modeling and quantification of mechanical damage severity in pipelines. International Pipeline Conference, pp. V1T-V3T (American Society of Mechanical Engineers, 2016).

[204] S. Guo, L. Xu, S. Dong and Y.F. Cheng, Finite element modeling of hydrogen atom diffusion and distribution at corrosion defect on aged pipelines transporting hydrogen, Int. J. Hydrogen Energ. (2023).

[205] M. Cabrini, L. Coppola, S. Lorenzi, C. Testa, F. Carugo, D.P. Bucella and T. Pastore, Hydrogen permeation in X65 steel under cyclic loading, Materials 13(10) (2020) 2309.

[206] C. Miehe, M. Hofacker, L.M. Schänzel and F. Aldakheel, Phase field modeling of fracture in multi-physics problems. Part II. Coupled brittle-to-ductile failure criteria and crack propagation in thermo-elastic – plastic solids, Comput. Method. Appl. M. 294 (2015) 486-522.

[207] Z. Khalil, A.Y. Elghazouli and E. Martínez-Pañeda, A generalised phase field model for fatigue crack growth in elastic – plastic solids with an efficient monolithic solver, Comput. Method. Appl. M. 388 (2022) 114286.

[208] F.P. Duda, A. Ciarbonetti, S. Toro and A.E. Huespe, A phase-field model for solute-assisted brittle fracture in elastic-plastic solids, Int. J. Plasticity 102 (2018) 16-40.

[209] S. Zhou, T. Rabczuk and X. Zhuang, Phase field modeling of quasi-static and dynamic crack propagation: COMSOL implementation and case studies, Adv. Eng. Softw. 122 (2018) 31-49.

[210] C. Li, J. Fang, C. Wu, G. Sun, G. Steven and Q. Li, Phase field fracture in elasto-plastic solids: Incorporating phenomenological failure criteria for ductile materials, Comput. Method. Appl. M. 391 (2022) 114580.

[211] N. Khandelwal and A.R. Murthy, Ductile fracture simulation using phase field method with various damage models based on different degradation and geometric crack functions, Materials Today Communications 35 (2023) 105627.

[212] J. Wu, Robust numerical implementation of non-standard phase-field damage models for failure in solids, Comput. Method. Appl. M. 340 (2018) 767-797.

[213] J. Wang, Y. Shuai, C. Feng, P. Zhang, T. Wang, N. Lin and Z. Liu, Multi-dimensional mechanical response of multiple longitudinally aligned dents on pipelines and its effect on pipe integrity, Thin Wall. Struct. 166 (2021) 108020.

[214] M. Lin, Characterization of tensile and fracture properties of X52 steel pipes and their girth welds, (2015).

[215] W. Chen and J. Wu, Phase-field cohesive zone modeling of multi-physical fracture in solids and the open-source implementation in Comsol Multiphysics, Theor. Appl. Fract. Mec. 117 (2022) 103153.

[216] P.K. Kristensen, C.F. Niordson and E. Martinez-Paneda, Applications of phase field fracture in modelling hydrogen assisted failures, Theor. Appl. Fract. Mec. 110 (2020) 102837.

[217] A. Nagao, M. Dadfarnia, B.P. Somerday, P. Sofronis and R.O. Ritchie, Hydrogen-enhanced-plasticity mediated decohesion for hydrogen-induced intergranular and “quasi-cleavage” fracture of lath martensitic steels, J. Mech. Phys. Solids 112 (2018) 403-430.

[218] E. Martínez-Pañeda, Z.D. Harris, S. Fuentes-Alonso, J.R. Scully and J.T. Burns, On the suitability of slow strain rate tensile testing for assessing hydrogen embrittlement susceptibility, Corros. Sci. 163 (2020) 108291.

[219] M. Lin, Y. Li, J.J. Roger Cheng, S. Koduru, M. Kainat, X. Zhang and S. Adeeb, Novel XFEM variable strain damage model for predicting fracture in small-scale SENT and full-scale pipe tests, Eng. Fract. Mech. 271 (2022) 108628.

[220] K.H. Pham, K. Ravi-Chandar and C.M. Landis, Experimental validation of a phase-field model for fracture, Int. J. Fracture 205 (2017) 83-101.

[221] T.T. Nguyen, J. Yvonnet, M. Bornert, C. Chateau, K. Sab, R. Romani and R. Le Roy, On the choice of parameters in the phase field method for simulating crack initiation with experimental validation, Int. J. Fracture 197 (2016) 213-226.

[222] S. Zheng, Y. Qin, W. Li, F. Huang, Y. Qiang, S. Yang, L. Wen and Y. Jin, Effect of hydrogen traps on hydrogen permeation in X80 pipeline steel——a joint experimental and modelling study, Int. J. Hydrogen Energ. 48(12) (2023) 4773-4788.

[223] T.K. Mandal, V.P. Nguyen and J. Wu, Comparative study of phase-field damage models for hydrogen assisted cracking, Theor. Appl. Fract. Mec. 111 (2021) 102840.